Proceedings of SCANNING 2000

May 9–12, 2000
San Antonio, Texas, USA

Wednesday, May 10

Applications of SEM in Forensic Science

Cathodoluminescence Microscopy of Paint Samples

THOMAS J. HOPEN, RICHARD S. BROWN, DAVID A. VANKO,* DR. WILFRIED STOECKLEIN†

MVA, Inc., Norcross, Georgia, USA; *Dept. of Geology, Georgia State University, Georgia, USA; †Kriminaltechnisches Institut, Bunderskriminalamt, Wiesbaden, Germany

The layer sequence of multilayered white and off-white paint chips is sometimes difficult to discern when utilizing commonly employed microscopical methods. This layer sequence information becomes vitally important when comparing a questioned paint sample to a paint sample of known origin. Techniques such as reflected light microscopy, fluorescence microscopy, and scanning electron microscopy (SEM) coupled with energy dispersive x-ray spectrometry (EDS) may not provide the needed discrimination. The elemental information obtained by EDS is of limited value since elemental composition alone is not sufficient to identify pigments/extenders used in white and off-white paints or to distinguish between different phases. Also, binder information may not be available for comparison since the thinness of the layers and the abundance of extender pigments may preclude analysis by Fourier transform infrared (FTIR) microspectrophotometry.

Cathodoluminescence microscopy (CLM) may provide the needed layer sequence information and discrimination when analyzing and comparing multilayered white and off-white paint samples. Cathodoluminescence is the emission of radiation from the sample in the visible light region and neighboring wavelengths following excitation by electrons generated from a cathode electron gun. CLM provides further discrimination of the layer sequence of multilayered white and off-white paint samples since cathodoluminescence is sensitive to phase differences, trace amounts of foreign atoms, and other lattice imperfections.

Analysis of polished cross-sections by CLM was accomplished utilizing a light microscope coupled with a vacuum specimen chamber and a cold-cathode electron gun. A comparison was made of the layer information obtained by CLM, darkfield reflected light microscopy, fluorescence microscopy, and SEM-EDS of several architectural paint cross-sections.

Forensic Microscopy in Pharmaceutical Manufacturing — Where Did Those Dark Spots Come From?

J.P. NEILLY, J.A. FAGERLAND, J.J. SZPYLMAN AND W. DZIKI

Abbott Laboratories, Pharmaceutical Products Division, Abbott Park, IL, USA

In pharmaceutical manufacturing, potent chemical compounds are combined with excipients to create dosage forms that are safe and effective. Manufacturing involves many complex operations such as milling, mixing, granulation, and tablet compression and coating. A variety of materials can be used as excipients including synthetic compounds, agricultural materials such as starch and sugars, and mined material such as talc. Occasionally, unwanted discoloration or dark spots can occur in the final products rendering them aesthetically unacceptable. Forensic microscopy methods such as polarized light microscopy (PLM), Fourier-transform infrared spectroscopy (FTIR), scanning electron microscopy (SEM), and energy dispersive x-ray spectroscopy (EDS) can be used to determine the source of dark spots that arise during manufacture of pharmaceutical products.[1]

During visual inspection of a new tablet formulation, small, black and silver-colored spots were observed on the tablet surface. Initial inspection with a stereomicroscope showed that the particles were opaque, silver-gray in color and very reflective. By SEM, their texture was determined to be primarily smooth with conchoidal fractures and many rough patches. EDS of the smooth areas detected only carbon, while the rough patches contained carbon, oxygen, magnesium, and silicon. SEM showed that the particles had the morphology of graphite,[2] and EDS indicated that the rough patches were magnesium silicate or talc. Talc is known to contain graphite,[3] and similar particles were eventually found in the talc used in manufacturing this product.

Contaminants can be introduced during manufacturing. During recent production of an oral liquid, numerous black, irregular particles were found in a liquid pharmaceutical

product. By EDS, the particles contained primarily carbon and fluorine with low levels of oxygen, sodium, and silicon, suggesting that the particles might be part of a gasket or seal composed of fluoropolymer. However, SEM examination showed that the particles had a unique fibrous structure similar to that of expanded polytetrafluoroethylene (PTFE). In addition, several particles had adherent diatoms on them. The elemental composition, fine structure of the particles, and presence of diatoms identified the source of the contaminants as a PTFE/diatomaceous filter that had failed.

During stability testing of coated and uncoated tablets, dark spots formed on tablets after they were exposed to accelerated storage conditions (high heat and humidity). Examination with a stereomicroscope showed that the spots were actually holes where material had fallen out of the tablet. In addition, discoloration of the tablet and coating material around the hole had occurred. Cracks radiated from the holes, and small yellow fibrous particles were present on the edges of the holes. EDS and x-ray mapping showed fibrous structures that contained sodium throughout discolored tablets and surrounding the holes. These structures were identified as croscarmellose, a disintegrant used in this formulation. The fact that they were on the edges of the holes suggested that they had performed their function by absorbing water and swelling.

The active compound in this formulation was a primary amine and contained sulfur that allowed unique localization by EDS and x-ray mapping. X-ray maps showed that the drug had migrated away from the holes and suggested that water based diffusion may have occurred. Lactose is known to turn brown when in contact with primary amines.[3] Therefore, migrating drug may have reacted with lactose to form the brown spots.

Identifying the source of the water that caused the drug migration came from careful examination of the excipients. The only excipient that had particles approximately the size of the holes in the tablet was anhydrous citric acid, which is very hydroscopic.[3] Large citric acid particles on the surface of normal tablets were identified by microscopic FTIR. The largest citric acid particles likely absorbed enough water to activate the disintegrant, cause diffusion of the drug, and facilitate reaction of drug with lactose to form the colored spots. Reducing the particle size of the citric acid is being evaluated as a solution to this problem

These examples clearly show the utility of correlative microscopy for identifying the source of contaminants in pharmaceutical products.

References

1. Briton HG, Bogdonawich SJ, Bugay DE, DeVincentis J, Lewen G, Newman AW: Physical Characterization of Pharmaceutical Solids. Pharmaceutical Research 8, 963–973 (1991)
2. McCrone Particle Atlas, Electronic Edition PAE2 CD-ROM, 1992.
3. Wade A, Weller PJ eds., Handbook of Pharmaceutical Excipients 2nd ed. American Pharmaceutical Association 124, 257 (1994)

An X-ray Spectral Database for Forensic Applications

DENNIS C. WARD

FBI Laboratory, Washington, D.C., USA

The scanning electron microscope (SEM) with associated energy dispersive spectrometer (EDS) is frequently used in the forensic laboratory to characterize the structure and elemental composition of a variety of materials of forensic significance. Most often the results of these examinations are applied comparatively. Absence of differences may indicate that the materials had a common origin. Conclusions of this type require only temporal data acquisition.

As with other developed spectroscopies (FTIR, MS), the usefulness of SEM/EDS is limited without the ability to archive spectra within a database utility. The FBI Laboratory has designed such an X-ray database, consisting of storage, query, and display utilities unique to X-ray spectroscopy. Associated with each spectrum is: 1. A description of the material, including manufacturer criteria and physical characteristics, 2. Compositional characteristics, 3. Instrumental parameters, and 4. Image. Material classes are organized in a hierarchical tree. Database queries may be made by selecting any combination of descriptors and compositional characteristics, or by simply performing a "best fit". The spectra returned from a query can be critically compared in an interactive display.

This database application permits:

- retrieval of compositional and structural information regarding a specific item
- retrieval of compositional and structural information of materials with a few related characteristics
- comparison of the composition of an unknown material to that of standards, and
- determination of the variations of composition within a material class

Future development will include networking this database to other forensic laboratories.

Classification of Puncture Holes in Plastic Bottles by Light and Scanning Electron Microscopy: A Preliminary Study

S.F. PLATEK, N.RANIERI, J.B.CROWE AND K.A. WOLNIK

Forensic Chemistry Center, U.S. Food and Drug Administration, Cincinnati, Ohio, USA

An increasing number of cases involving accidental, misinterpreted, falsely reported and intentional acts of tampering with food and beverage products are investigated by the Forensic Chemistry Center (FCC) of the US Food and Drug Administration. The Federal Anti-Tampering Act of 1983 specifically addresses product tampering as well as

the false report of product tampering as a felony with substantial fines and prison sentences.[1,2] Suspected tampering cases are routinely submitted to the FCC for confirmation of breached or punctured containers with visible holes and the identification of any foreign substance introduced. Cases range from suspect holes in both product and container items including fruits[3], plastic/paper wrapped food items (exa.—bread, candy bars), plastic film wrapped items (exa.—meat and produce) and plastic bottles and metal cans. In a number of cases analyzed by the FCC, there have been associated threats of extortion, terrorism and both accidental and deliberate product tampering involving holes or punctures in product packaging. Identification of the object(s) used to make the holes has been demonstrated to reduce the initial analysis time and determine if the hole was consistent with known objects. The identification is also valuable in the follow-up investigation.

Plastic bottles made of a variety of relatively soft plastics are used to package numerous items including soft drinks, bottled water, milk, juice, cosmetics, pharmaceuticals, and cleaning products. A study was initiated at the FCC to investigate and classify holes in plastic bottles made by a variety of commonly encountered objects. Emphasis was placed upon items that could be used to inject or make a suitable hole for the introduction or removal of liquids. Thirty-eight (38) puncturing objects [including nails, screws, needles (syringe, sewing), tacks, pins, paper clips, tools, blades (knife, razor), staples, fish hooks, scissors, and punches] were used to produce simulated tampering holes in plastic bottles.

Each object was used to make a series of eleven holes in a 5×10-cm section of plastic soft drink bottle. Stereoscopic (SLM), polarized light microscopy and scanning electron microscopy (SEM) were used to analyze and characterize each type of hole. The puncture holes were initially examined on both sides by SLM. It was determined the inner or eruption surface provided the most characteristic information.

SEM analysis provided additional characteristic information including that the cut/puncture surface revealed smooth cut surfaces for syringe, razor, scissors and knife tips. Thread cuts were visible on twisted screw holes and could be differentiated from screw punctures. The eruption surface around the inside edges of the holes provided characteristic shapes usually dependent on the cross-sectional profile of the penetrating object. Cut nail holes (regardless of size) could be differentiated from conical pin, tack and sewing needle holes. Figure 1 shows an example of secondary electron images comparing characteristic puncture holes in a plastic soft drink bottle (interior surface) made by a 25-gauge syringe needle (A) and a sewing needle (B). Syringe needles produced characteristic holes forming a "single eye lid" appearance while sewing (conical) needles produced a symmetrical "double eye lid" appearance (Fig. 1). Staples and drill bits also produced unique hole eruption surfaces. The diameter of circular penetration objects could be also be approximated. The preliminary results of this study show that there are a number of unique and identifiable characteristics in the eruption surfaces of holes in plastic bottles made by penetrating objects. Continuing research at the FCC will include developing a complete method for hole classification and the preparation of a guide for the identification of puncture holes.

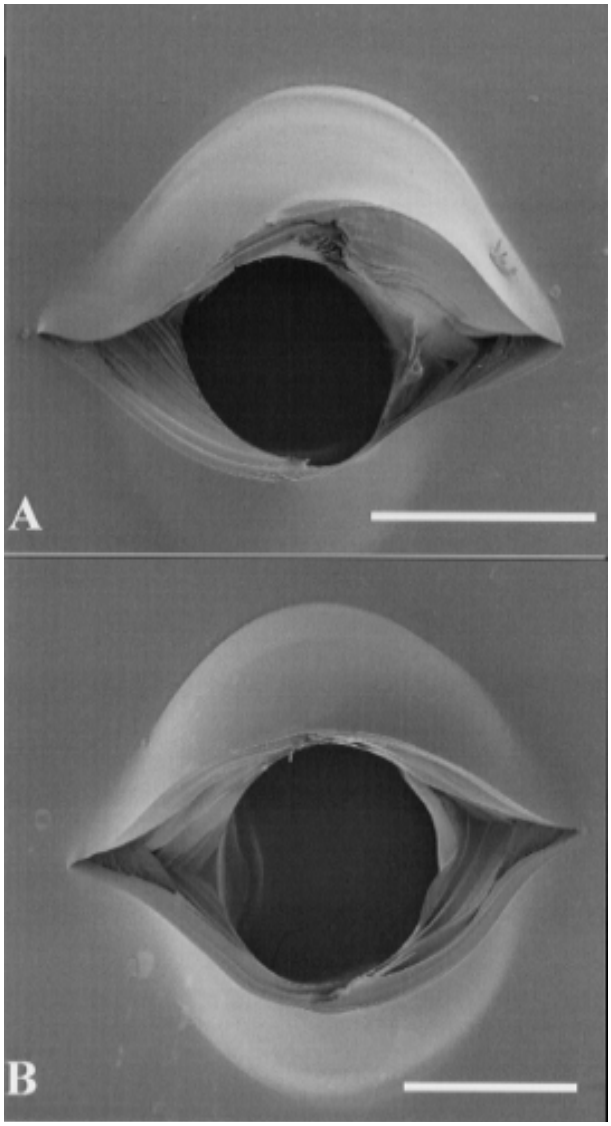

FIG. 1 Secondary electron images comparing characteristic puncture holes (interior surface) in a plastic soft drink bottle made by a 25-gauge syringe needle (A) and a sewing needle (B). Syringe needles produced characteristic holes forming a "single eye lid" appearance while sewing (conical) needles produced a symmetrical "double eye lid" appearance. Bar markers = 0.5 mm

References

1. Federal Anti Tampering Act, Title 18, USC Section 1365, 1983
2. Fines Enhancement Statues of 1985, Title 18, USC Section 3571
3. Tomlinson JA, Crowe JB, Ranieri N, Kindig JP, Platek SF: Supermarket tampering: cocaine in syringes and in fruit. *J. Forensic Sciences* (accepted for publication — in print)

Forensic Analysis of Diamonds and Diamond Simulants, An Unusual Case History

CARL N. BRUNO AND SCOTT KOVAR

Nassau County Police Department, Scientific Investigation Bureau, Mineola, New York, U.S.A.

Scanning electron microscopy/energy dispersive X-ray spectroscopy (SEM/EDS) and energy dispersive X-ray fluorescence spectroscopy (EDXRF) are qualitative and quantitative non-destructive techniques utilized in forensic analysis for gunshot residue (GSR), metal alloys, powders, glasses, paints, etc. Present day software speeds up both image capture in SEM and qualitative/quantitative energy dispersive spectrometric analysis in seconds rather than minutes. An Amray 1000 SEM with EDAX DX Prime EDS and a Phillips PV 9500 XRF Spectrometer were the actual instruments utilized in this case study.

Interestingly, there have been very few, if any, papers or literature presented in the forensic community on diamonds and diamond simulants.

The subject in this case started advertising appraisals for $49.95 and with the use of a discount coupon, he would appraise an unlimited number of items for only $24.95. The police department and Scientific Investigation Bureau got involved in February, 1993, when a complainant claimed her diamond was switched for a cubic zirconia (CZ) stone. A sting was set up with four diamond rings and a loose pear-shaped diamond (0.8 ct.), which was subsequently switched with a cubic zirconia simulant. The subject was indicted and plead guilty to eleven counts and received a jail term of 3–6 years for grand larceny and 2–4 years for insurance fraud.

The analysis of dozens of rings and pieces of jewelry, over a period of eight months, was made involving consultation with GIA (Gemological Institute of America); mapping inclusions of diamonds, utilizing a gemological microscope; measuring stones with micrometers and calipers; weighing stones; determining girdle and culet type; measuring refractive index, specific gravity, UV fluorescence, and thermal conductivity. Diamonds are easy to tell apart from most simulants due to the fact that diamonds have numerous inclusions as either imperfections (e.g. — cloud, cavity, feather, pit, pin point, cavity, etc.), or minerals (e.g. — colorless diamond, zircon, garnet [red], diopside [green], magnetite/hematite/chromite [black], chrome spinel [red], olivine [green], etc.). Also, diamonds typically have frosted girdles.

For these analyses we utilized a micrometer or caliper to measure table diameter, girdle diameter, and depth. The refractive index was measured directly by gemological microscope or gemological refractometer. The specific gravity was measured with a special diamond pan attachment to a weighing pan balance. A diamond proportion analyzer was used to measure table %, crown angle, crown height %, girdle thickness %, pavilion depth %, and total depth %. Finally, a thermal conductivity instrument was used to determine whether a stone was a diamond simulant or not. Diamonds have the highest thermal conductivity, by far, of any mineral, except for moissanite, which is fairly close and would fool the older instruments (early 1990's). All this was necessary to characterize and individualize the stones from this particular case. It should be noted, however, that none of the original diamonds was actually recovered except for the stone originally used for the sting.

In 1996, we became involved with SEM/EDS and XRF, and have since analyzed simulants to determine their chemical composition. Some examples of various simulants are: CZ (ZrO_2). YAG ($Y_3Al_5O_{12}$), sapphire (Al_2O_3), topaz ($Al_2[F/OH]_2\ SiO_4$), quartz (SiO_2), rutile (TiO_2), spinel ($MgAl_2O_4$), strontium titanate ($SrTiO_3$), zircon ($ZrSiO_4$), GGG ($Gd_3Ga_5O_{12}$), and moissanite (SiC). The use of XRF is necessary for analysis of trace elements down to 10-100 PPM and LA-ICP/MS, an expensive instrument, would be best suited down to PPB and PPT (parts per trillion).

Forensic analysis of jewelry settings to determine alloy content, and whether or not a gold alloy is only a plating, can also be done either instrumentally (SEM/EDS, or XRF) or by touchstone (basalt) testing utilizing known gold touch needles and appropriate acids. Through the years we have analyzed alleged gold bars (brass), gold plated coins, and other counterfeit metal items.

Case Studies in Gunshot Residue Analysis by SEM/EDX

JAMES D. GARCIA AND MICHAEL V. MARTINEZ

Bexar County Criminal Investigation Laboratory, San Antonio, Texas; Bexar County Criminal Investigation Laboratory, San Antonio, Texas, USA

The use of scanning electron microscopy/energy dispersive x-ray (SEM/EDX) analysis in criminal investigations has proven to be a very important tool in a variety of criminal cases. With the advent of automated systems, the ability of the forensic scientist to analyze a variety of forensic samples has increased and improved the use of SEM/EDX systems. The Bexar County Criminal Investigation Laboratory in San Antonio, Texas, has employed the use of automated SEM/EDX analysis since 1996. The primary use of the automated system is for the detection of primer gunshot residues from a wide assortment of possible sources. Three cases where automated SEM/EDX technology was used to detect for primer gunshot residue from locations other than the hands of a suspect or a victim show the versatility of its forensic importance. Case one deals with primer gunshot residue detected on a leaf found at a homicide crime scene. The results of the analysis aided in solidifying the reconstruction of a fatal gunshot wound

to the back of the head followed by several "coup-de-grâce" shots. Case two deals with primer gunshot residue found on the interior of a vehicle, on the sleeve of a jacket and the right hand of a subject involved in an unusual drive-by shooting. The final case deals with primer gunshot residue detected on latex gloves used in one the largest mass murders by the "Mexican Mafia" in San Antonio history. These three cases represent novel forensic approaches using modern technology with simple sample collection techniques of commercially available carbon tape sampling devices. The samples were analyzed at an approximate magnification of 350 at 20 KeV and a working distance of 10 mm.

Can Gunshot Residue Indicate the Type of Ammunition Fired?

JOZEF LEBIEDZIK

Advanced Research Instruments Corp., Wheat Ridge, Colorado, USA

The presence or absence of gunshot residue (GSR) on the hand of a suspect can be easily and rapidly determined by SEM-EDX analysis if the sample is collected shortly after a weapon is fired.[1,2] To determine what type of ammunition was fired is more difficult and in some instances may be impossible. However, a comprehensive GSR analysis can point to a specific ammunition.

A careful study of GSR and supporting particles reveal a number of indicators typical to a specific type or a family of fired ammunition. This type of investigation requires a sufficient amount of each type of available ammunition to be fired from a clean weapon to collect statistically significant data. The job is much more time consuming than the GSR analysis alone, since it requires analysis of all particles not just the high density ones as is the case for GSR analysis.

There are two basic indicators that may be combined to lead us to the type of fired ammunition. The two indicators are morphology and composition of the supporting particles. The morphology of GSR particles points to a family of possible ammunition and the composition of the supporting particles may reveal the type of bullet fired or a specific type of ammunition.

To illustrate this approach we limit our focus to large GSR particles only. In the SEM, they are easy to find and can provide us with the first estimate.

The *morphology* of GSR particles greater than several micrometers can be divided into three basic groups:

1. Spheroid forming. This is typical for Russian, Chinese, Czech 9mm or PMC ammunition.
2. Irregular shapes. Typical for Winchester, Mag Safe +P+, Federal Hydra Shok, CCI Blazer.
3. Mixed shapes. Other types.

Each group may be divided into subgroups based upon more subtle morphological differences, but more data may need to be collected to form a reliable conclusion.

The *composition* of GSR supporting particles, expressed as scanned area fraction in parts per million, indicates the concentration of any given type of particle. This number is routinely available from the image/x-ray analyzer. For example, lead area fraction divided by GSR area fraction yields the relative lead concentration to GSR in the sample. If this value is less than one, implying low lead concentration, this indicates jacketed bullet (typically around 0.1). If the value is greater than one (typically 5-30) this indicates a lead bullet. Using relative concentration value rather than absolute values dramatically reduces the data spread due to various sampling or collection errors.

To distinguish .22LR Federal from Remington ammunition is easy. The .22LR Federal has a copper plated lead bullet while Remington has a brass plated lead bullet. If the ratio of copper-lead particles expressed as area fraction to brass-lead particles is greater than one, it is from Federal ammunition. If less than one it is from a brass plated Remington.[3]

Another example of identification of specific ammunition is the significant presence of strontium. If the strontium concentration is half or more than that of GSR, coupled with unusually low lead presence, this points directly (regardless of morphology) to 9mm CCI Blazer "lead free" ammunition.[4]

These preliminary results indicate that there is enough information in the GSR and supporting particles to determine, in some cases, the origin of the fired ammunition. The next step is to refine the system of clues which will converge to a specific ammunition applicable to larger variety of ammunition.

References

1. Meng HH, Caddy B. Gunshot Residue Analysis-A Review. J Forensic Sci 1997; 42(4):553-570.
2. Lebiedzik J, Johnson DL. Rapid Search and Quantitative Analysis of Gunshot Residue Particles in the SEM. J Forensic Sci 2000;45(1):83-92.
3. Wrobel H A, Miller J J, Kijek M. Identification of Ammunition from Gunshot Residue and Cartridge Related Materials-A Preliminary Model Using .22 Caliber Rimfire Ammunition. J Forensic Sci 1998;43(2):324-328.
4. Zeichner A, Schecter B, Brener R. Antimony Enrichment on the Bullets= Surface and the Possibility of Finding It in Gunshot Residue (GSR) of the Ammunition Having Antimony-Free Primers. J Forensic Sci 1998;43(3): 493-501.

Fact of Friction: Putting the Brakes on Gunshot Residue

J.R. GIACALONE

West Virginia State Police Forensic Laboratory, South Charleston, West Virginia, USA

Microtrace particle analysis of gunshot residue (GSR) is accomplished by utilizing scanning electron microscopy coupled with energy dispersive x-ray spectroscopy (SEM/EDS).[1] The identification of these micron size particles on the hands and/or face of a suspect by a crime laboratory has had forensic value for the past two decades. This value is attributed to the fact that when the primer in a round of ammunition is detonated, the resultant residue products are unique.[2] The quest to identify hobby's, occupations, and activities which may involve GSR-like particles has been explored.[3] Over the past several years however, two different non-firearm related sources have been documented as having the potential ability to produce residue which can be construed as GSR.[4,5]

Friction materials are one of these sources and they are commonly encountered in brakes and transmissions. Their formulations can have ingredients that may produce residue akin to GSR. Primer compositions containing lead, barium, and antimony compounds yield conglomerate residue particles of these elements when they mix in the vapor phase during the discharge.[6]

There exists friction material formulations which have a myriad of resins, binders, fillers, and metallic flakes.

The wheel is hailed as one of the greatest inventions but its value and usefulness are minimized unless it can be controlled by slowing and stopping. Therefore, with the advent of the wheel arose perhaps a more important invention — the brake. Brakes are by far the most important mechanism on any vehicle because the safety and lives of the passengers depend on the proper operation of the braking system.[7] Brakes are energy absorbing mechanisms that, on demand, slow a moving object. Friction, which converts kinetic energy (motion) into thermal energy (heat), is one way to achieve this and is the most popular method for general purpose clutching and braking. Leonardo da Vinci was one of the earliest scholars of tribology and undertook systematic studies on friction.

This study focuses on friction material formulations. Samples of brake lining from various wheeled vehicles ranging from bicycles to airplanes were gathered and analyzed by SEM/EDS under the same parameters which are utilized for the identification of GSR. The friction material specimens originated from 'new', unused pads and from worn, used ones. Sample preparation simply involved dabbing the brake friction material using a pin mount covered with double-sided carbon adhesive tape. The specimens were manually searched at magnifications ranging from 40–4000 times. This afforded the opportunity to locate, analyze, and record particles which are representative of the respective friction material ingredients. Where possible the MSDS sheets were obtained to assist in correlating the findings. A variety of inorganic elements were catalogued during this research. One disc brake pad encountered is a sintered kevlar/carbon graphite type that contains lead/barium/antimony in its composition.

The existence of non-firearm sources of lead/barium/antimony particles necessitates a reevaluation of the uniqueness of such residue and their implication with discharge residue (GSR). Though the majority of primer residue encountered consists of lead/barium/antimony, there are other formulations in older, foreign, and newly developed 'lead-free' ammunition that have yet to be encountered in friction materials. The inclusion of aluminum, copper, and/or zinc with lead/barium/antimony particles will maintain their uniqueness to a firearm origin. Morphology can also play a role in evaluating the creation and origin of these particles. It is strongly advised and increasing useful to examine the residue remaining in the spent cartridge casing involved in the crime. By using this as a 'known' it can be used to compare the 'questioned' residue formulations detected on the suspect's evidence.

The importance of microtrace particle analysis by SEM/EDS continues to grow in forensic science. It provides the capability to identify particulate residue from various sources and allows them to be associated with specific circumstances, environments, and scenarios.[8] The objective of a criminal investigation is to link both the crime scene with the suspect and the suspect to the crime scene. Forensic science with its cornucopia of technological, analytical, and sensitive comparison examinations provides the avenue to establish these connections and SEM/EDS is a vital tool in the law enforcement arsenal.

References

1. White RS, Owens AD: Automation of gunshot residue detection and analysis by scanning electron microscopy/energy dispersive x-ray analysis (SEM/EDX). J Foren Sci JFSCA 32, No. 6, 1595-1603 (1987)
2. Wolton GM, Nesbitt RS, Calloway AR, Loper GL, Jones, P: Final Report On Particle Analysis For Gunshot Residue Detection, Aerospace Corporation, El Segundo, CA, 1977, ATR-77, 7915-3
3. Wolton GM, Nesbitt RS, Calloway AR, Loper GL, Jones, P: Particle analysis for the detection of gunshot residue: II: Occupational and environmental particles. J. Foren Sci 24 No. 2, 533-545 (1979)
4. Mosher PV, McVicar MJ, Randall ED, Slid EH: Gunshot residue similar particles produced by fireworks. Can Society Foren Sci J 31, No. 2, 157-168 (1998)
5. Garofano L, Capra M, Ferrari GP, Bizzaro D, Di Tullio D, Dell'Olio A, Ghitti A: Gunshot residue further studies on particles of environmental and occupational origin. Foren Sci Intl 103, 1-21 (1999)
6. Basu S: Formation of gunshot residue. J Foren Sci 27, No.1, 72-91 (1982)
7. Halderman JD, Chase MD: Automotive Brake Systems, 2nd ed, Chapter 2, Prentice Hall, NJ (2000)
8. Giaclone JR: Scanning electron microscopy/energy dispersive x-ray analysis (SEM/EDS) of forensic microtrace particles collected on carbon-conductive adhesive tape. Scanning 19, 232-233 (1997)

Activities of the European Network of Forensic Science Institutes Working Group "Firearms" with Special Focus on European Gunshot Residue Work

LUDWIG NIEWÖHNER

Dept. of Gunshot Traces, Forensic Science Institute of the Bundeskriminalamt, Wiesbaden, Germany

ENFSI is the abbreviation of the European Network of Forensic Science Institutes (ENFSI), and was founded in 1993 by the directors of 9 national forensic science laboratories in Europe. Currently more than 40 directors of European forensic labs are ordinary members of that organization or are just applying for a membership.

The aim of ENFSI is to promote co-operation between list members and their laboratories. This is achieved through:

- discussion of managerial questions, effective utilization of forensic science, scientific development, and standards of practice
- exchange of quality assurance methods and procedures, training, and scientific exchange programs
- and co-operation with other international organizations.

Therefore special working groups were established for the different forensic fields of work. The ENFSI working group "Firearms" was approved by the ENFSI Board in 1995, and covers the fields of firearm examination, gunshot residues (GSR), evaluation of shooting distances, and ballistics. Currently, representatives of 28 ENFSI members are attending the annual working group meetings.

Within the common framework for ENFSI working groups, the working group "Firearms" is actually promoting the following projects:

- establishing international data collections on GSR and firearms with access to all working group members
- preparing and performing a proficiency test on GSR
- coordinating the interpretation of results
- combining research activities and providing education and training.

Working groups report on the European proficiency test activities, including the preparation of identical GSR test samples and examples of some of the European research projects on GSR.

Preparation of an In-house GSR Standard

WAYNE D. NIEMEYER

McCrone Associates, Inc., Westmont, Illinois

Using automated analysis software to identify gunshot residue (GSR) particles in the scanning electron microscope (SEM) requires careful quality assurance of the system. In addition to checking the qualitative and quantitative performance of the energy dispersive X-ray (EDX) system one must also ensure SEM performance such as stage positioning, brightness/contrast, and beam current parameters.

Simple particle manipulation techniques can be used to prepare a custom GSR standard to conform with the particular SEM in use at the laboratory. The work can be performed using a stereo microscope with at least X80 magnification capability.

Procure a spent cartridge casing and a copper jacketed bullet. Using a stiff needle or pick, gently scrape the inside of the cartridge casing near the primer and lower sidewall. Invert the cartridge over a glass petri dish and gently tap the side of the cartridge to force the powder out into the dish. Over separate petri dishes use a fine file to produce particles of brass from the casing and copper/lead from the bullet. As an option, cut the bullet open to expose the lead and file off particles.

Prepare another petri dish with iron (or other low average atomic number material) filings. Keep the petri dishes covered and stored in a secure area for future use to prepare more references if necessary.

Prepare a "very fine" grade tungsten needle by sharpening a 24-gauge (0.52mm) tungsten wire[1]. Place the needle into a suitable needle holder. Attach a 12mm diameter double sided carbon tape (preferably with a smooth surface) to a SEM stub. Scribe a grid onto the tape using a stiff needle or probe. Use the stereomicroscope to locate sub-10 micrometer dark, shiny spherical/ellipsoidal particles in the petri dishes. Carefully insert the needle into the field of view and, while maintaining about a 20-30 degree angle, touch the needle on the particle. While keeping the needle in the field of view, move the dish aside, place the SEM stub into the field of view, and place the particle on the tape in a grid square. Continue this process until particles representing all types are mounted.

Prepare the reference SEM stub in the same manner as for submitted SEM GSR kits. Set the SEM parameters (BEI, accelerating voltage, beam current) for optimized imaging for GSR analysis. If parameters are unknown, use the iron particles to adjust the graylevel to about 100 (measured in the EDS imaging window). In the SEM locate each particle, note the stage coordinates, graylevel intensity, and collect an EDS spectrum. Upon completion of the manual search, set up the automated parameters and appropriate measurements and run the test on the reference stub. Compare results to the manual search, especially stage coordinates to ensure that one particle is not being counted twice or more in overlapping fields of view.

With proper care, the in-house SEM GSR standard will last for many years.

Reference:

Teetsov, Anna: Preparation and Use of Needles and Micropipets for Handling Very Small Particles, *Microscopy Today*, #00-2, 8-16, February/March 2000.

Food Structure and Functionality Symposium

Effects of Microfluidization on the Matrix of Mozzarella Cheeses

P.H. COOKE, M.H. TUNICK, E.L. MALIN

Eastern Regional Research Center, Agricultural Research Service, U.S. Department of Agriculture, Wyndmoor, PA, USA

The complexity of physical and chemical properties of milk products offers many opportunities to develop new and unusual formulations. Special functional characteristics can be developed through novel processing and engineering. In traditional Mozzarella cheeses the milk proteins form an extensive, continuous phase separated by a discontinuous phase filled with milk fats, and the interface between the phases contains most of the microbial population. Spatial dimensions of features in both phases range from 10^{-3} to 10^{-6} m. The arrangement and composition of the phases apparently regulates the physical properties of the product, so an understanding of the molecular interactions within and between the phases could provide many important clues to guide further design. We have examined the structure of the protein matrix in Mozzarella cheeses in order to understand the effects of various compositions and processing steps on functional properties. Integrated microscopic imaging (SEM, TEM and AFM) and image transformation indicate that the matrix contains a pervasive structural repeat, around 10^{-8} m, similar to the dimensions of casein subunits observed in milk micelles and caseinates[1]. Studies using different rennets and processed sources of milk protein show that organization related to the subunit-repeat changes during a few weeks of refrigerated storage, suggesting a link between molecular organization and other measurable, functional properties[2–4].

Microfluidization of milk changes the basic structural organization of Mozzarella cheeses. For extreme parameters of both temperature and pressure (173 MPa/54 C), this processing approach transforms the typical two phase structure into a persistent emulsion with resolved features on a nanometer scale and functional properties that are not typical (5). Microscopic imaging reveals that the 15 nm subunit-repeat in the continuous phase is restricted to small areas, intercalated among numerous small fat droplets ranging from 20 to over 200 nm in diameter. Many of the protein subunits are distributed at the interface of the fat droplets, and this atypical pattern of organization does not change after 6 weeks of refrigerated storage. Moderate conditions (104 MPa/43 C) of homogenization result in fewer, larger droplets with a broader range of sizes, and minimal conditions (35 MPa/10 C) result in products that resemble the classical structure of Mozzarella. The results indicate that microfluidized milk under the extreme conditions does not produce typical Mozzarella cheeses, but suitable conditions might be found for designing a variety of other nanostructured milk products with advantageous functional properties.

References

1. Cooke PH, Tunick MH, Malin EL, Smith PW, Holsinger VH: Electron-density patterns in low-fat Mozzarella cheese during refrigerated storage. In *Chemistry of Structure- Function Relationships in Cheese,* (Eds. Malin EL and Tunick MH). Plenum Press, NY (1995) 311-320
2. Tunick MH, Mackey KL, Sheih JJ, Smith, PW, Cooke PH, Malin EL: Rheology and microstructure of low-fat Mozzarella cheese. *Intl Dairy J* 3, 649-662 (1993)
3. Tunick MH, Cooke PH, Malin EL, Smith PW, Holsinger VH: Reorganization of casein submicelles in Mozzarella cheese during storage. *Intl Dairy J* 7, 149-155 (1997)
4. Tunick MH, Cooke PH, Malin EL, Smith PW, Holsinger VH: Imaging of casein submicelles in Mozzarella cheeses by transmission electron microscopy. *Amer Lab* 30,44-47 (1998)
5. Van Hekken DL, Smith PW, Tunick ML, Malin EL, Holsinger VH: Textural properties of Mozzarella cheeses from milks with 1 or 3.2% fat homogenized at varying pressure and temperature. *J Dairy Sci* 82(Suppl 1)19 (1999)

The Stabilisation of Air in Foods Containing Fat — A Universal Mechanism

B.E. BROOKER

Institute of Food Research, Colney Lane, Norwich, UK

Many foods owe their characteristic rheological and organoleptic properties to the presence of an entrapped gas phase. Although some such foams are stabilised only by an adsorbed interfacial film, usually of protein, most foams owe their stability to the additional presence of fat. In the latter, complex interactions between fat and protein at the gas-water interface produce structures that are responsible for the observed stability.

In the case of foods containing globular fat, such as cream or confectionery emulsions, the incorporation of air produces a protein stabilised air-water interface and at the same time, globules of fat become permanently attached to the bubble surface as a result of coalescence of the air-water and fat-water interfaces. In the case of whipping cream, additional globule-globule interactions produce a series of cross links between bubbles that form a stable three-dimensional structure in which de-stabilisation caused by drainage is minimised. Similar fat-protein interactions can and have been demonstrated in toppings, frozen desserts, confectionery products and ice cream.

In some of these systems where a disperse fat phase is produced in the presence of highly surface active molecules, such as phospholipids or emulsifiers, an additional process takes place. The reduction in surface tension at the fat globule surface results in the ejection of fat crystals into the aqueous phase. In the course of this process the crys-

tals become enveloped in a layer of the oil-water interface and as a result become hydrophilic in their behaviour; e.g., they do not aggregate in aqueous systems. When gas is incorporated into the emulsion, the behaviour of hydrophilic crystals is similar to that observed for globules in that they become attached to the surface of bubbles in large numbers by the coalescence of the air-water and crystal-water interfaces. In foods such as desserts and bakery batters and doughs, crystal attachment allows the entrapment of large volumes of air by encouraging the stabilisation of small bubbles that would otherwise de-stabilise because of the high pressure of gas inside them.

In the case of baked products, crystal attachment to bubbles has another important significance. During baking, the fat crystals melt and leave behind their crystal-water interface that is incorporated into the bubble surface as the latter expands. Without this source of additional interface, bubbles in baked systems undergo one of two fates, neither of which is consistent with the formation of high volume products with fine crumb structure. They either break, allowing entrapped gas to escape from the system or they must coalesce with neighbouring bubbles to increase the ratio of their surface to volume. The attachment of crystals to bubbles in these products must therefore be seen as a mechanism for the transfer of interfacial material from the surface of fat droplets to bubbles.

It can thus be seen that in the many food systems containing globular fat and/or hydrophilic fat crystals, bubble stabilisation involves attachment of the fat phase to their surfaces by a common mechanism that involves coalescence of the air-water interface with the interface at the surface of the fat phase. For foods containing soluble protein and a fat phase, this mechanism is universal.

A Study of Fat Bloom and Anti-Bloom Agents

KATHY GROVES, P.J. SUBRAMANIAM, R.A. CURTIS, M.E. SAUNDERS, O.C. MURPHY

Leatherhead Food Research Association, Leatherhead, Surrey, England

This paper presents the results of a study of the effects of incorporation of four different anti-bloom fats and butterfat on the fat bloom development in tempered plain chocolate containing cocoa butter.

Bloom is the general term used to describe the crystallisation of either fat or sugar on the surface of chocolate. Fat bloom on chocolate is normally preceded by a loss of gloss and is visually apparent as white areas on the surface of the chocolate. The development of fat bloom is a problem in chocolate products but can occur in other fat systems and compound coatings.

Cocoa butter is polymorphic fat and can therefore form different crystalline or liquid-crystalline structures with different melting points. It is widely published that there are six polymorphic forms, although some research has postulated only four forms. Merken & Vaeck (1980) suggest that form III is a mixture of forms II and IV, and Fincke (1955) and Hernqvist (1987) claim that form VI is the same as form V except for the separation of the liquid triglyceride portion, making the form VI a higher-melting form. The most preferred form is form V as it has been found to give the highest level of contraction and gloss. In a well-tempered chocolate the transformation of form V to the more stable form VI has been identified as the cause of bloom using X-ray diffraction (Cebula & Ziegleder, 1993). Using microscopy it was found that the crystals in bloomed chocolate are identical to those in form VI cocoa butter (Jewell, 1974; Cruickshank & Jewell, 1977; Timms, 1984).

If, as is thought, the formation of bloom is a solid-state transformation, then anything that increases the liquid fat phase, such as butterfat, will delay bloom (confirmed in practice). However, this is not always so, as some liquid fats e.g. olive, and almond oil, accelerate the transformation to form VI (Timms, 1984). Published literature shows that many different ingredients could have anti-bloom properties. A common approach is the addition of butterfat. However, this has the negative effect of softening chocolate texture. This has led to the search for other anti-bloom agents.

In this study, the effects of addition of anti-bloom fats were evaluated in a standard plain chocolate. The aim was to see how these fats affected bloom development under different storage conditions. Six batches of chocolates were made, with cocoa butter (control), butterfat and four anti-bloom fats. The products were stored under different storage conditions. Gloss was assessed visually and hardness was measured using a Stable Microsystems TAXT2 Texture Analyser. Melting profiles of the chocolates were assessed after 1 week's storage at 20°C using a TA Instruments DSC 2920. Melting profiles of the different chocolates were used to estimate the percentage of liquid fat in the samples at 20°C and at 28°C. Bloom development was assessed using a stereomicroscope, and the surfaces of the chocolates were examined by cold-stage scanning electron microscopy.

The anti-bloom fats were found to be better at delaying bloom formation than butterfat and gave acceptable gloss. Three of the fats were similar in terms of hardness to the control, and one was similar to butterfat. Microscopy showed interesting differences in the size and shape of the bloom crystals and in their distribution over the surface. Accelerated storage conditions produced some very long needle-like crystals in the control and some of the other samples, possibly due to fractionation of the fat. These crystals had not been seen before in bloomed chocolate and may have been due to the fractionation of the cocoa butter during bloom development.

This work has shown some interesting effects of certain anti-bloom fats on texture, behaviour and bloom crystal appearance. Further work on the effects of anti-bloom fats in other products should advance understanding of chocolate stability further.

References

1. Cebula D. J., & Ziegleder, G. (1993). "Studies of bloom formation using X-ray diffraction from chocolates after long term storage". Fett Wissenschaft Technologie, 95 (9), 340–3
2. Cruickshank, D. A. Jewell, G. G. (1977). "Structural studies on tempered cocoa butter". Leatherhead Food RA Research Reports No. 256.
3. Fincke, H. (1955). Zucker-und Süsswarenwirtschaft, 8, 140–3
4. Hernqvist, L. (1987). "Chocolate temper" in "Industrial Chocolate Manufacture and Use". Ed. S.T. Beckett, pp159–71. Blackie USA and Canada: Van Nostrand Reinhold Company, New York.
5. Jewell, G. G. (1974). "Electron microscopy of chocolate. Part I. Structure of bloom on plain chocolate". Leatherhead Food RA Research Reports No. 202.
6. Merken, G. V. & Vaeck, S.V. (1980). "Study of polymorphism in cocoa butter by differential scanning calorimetry". Lebensmittel-Wissenschaft und Technologie, 13 (6), 314–7
7. Timms, R.E. (1984). "Phase behaviour of fats and their mixtures". Progress in Lipid Research, 23 (1), 1–38.

Fundamental Characteristics and Utilization of Milk Whey Protein

NAOFUMI KITABATAKE

Research Institute for Food Science, Kyoto University, Kyoto, Japan

Whey proteins from bovine milk are used for bakery, dairy, beverage, meat, and fish products as additive to improve and keep quality of products. The properties of heat-induced gels made from whey proteins are influenced by the heating conditions: protein concentration, pH, and heating temperature. Salts also affect the gelation of whey proteins, and the properties of the gels. Whey protein isolate (WPI) give a transparent gel or sol by heating under specific condition, although heat treatment usually produces a turbid suspension or gel. Heat-denatured protein molecules are in a soluble form in these transparent gels or sols, which are generally superior to their turbid counterparts as food materials. Preheated WPI under salt-free conditions, that is, transparent liquid, produces a transparent gel upon reheating in the presence of NaCl. This preheated WPI material, process whey protein (PWP), not only has properties similar to those of WPI over a wider range of conditions, but also has other novel characteristics as a food ingredient. The PWP can produce a transparent gel or a viscous liquid even at room temperature and can produce either a stable emulsion or an emulsion gel only by addition of salt. PWP is already being used in several processed foods because of superior functionalities. The PWP appears to consist of soluble linear aggregates of heat-denatured whey protein molecules. Such fine-stranded structures have been observed in heated ovalbumin and bovine serum albumin. Those fine-stranded structures might correspond to linear aggregates of heat-denatured globular protein molecules.

To clarify the details of the functionality of PWP the purified B-lactoglobulin A was used for further investigation. The B-lactoglobulin A preheated under salt-free condition gives transparent liquid on heating and produces a transparent gel upon reheating in the presence of NaCl as well as PWP.

WPI is believed to be a digestible protein ingredient because it is used for infant formula. However, B-lactoglobulin in WPI cannot be hydrolyzed by pepsins, including porcine, rat, bovine, human, carp pepsin in vivo and in vitro. On the other hand, B-lactoglobulin in PWP is easily hydrolyzed by any kind of pepsin. This means that PWP is more digestible in the stomach than WPI. Other protein components except B-lactoglobulin can be easily hydrolyzed by pepsin. Based on this results, we developed a new method to purify B-lactoglobulin from WPI using crude porcine pepsin. Using this method, a large quantity of native B-lactoglobulin was purified and a nutritional test of native B-lactoglobulin and heated B-lactoglobulin was done with rats. This test showed that the heated B-lactoglobulin is superior to unheated B-lactoglobulin for growth of rats.

Protein-protein Interactions during the Manufacture and Storage of Dried Milk Powder

A.B MCKENNA

New Zealand Dairy Research Institute, Palmerston North, New Zealand

The protein-protein interactions that occur during manufacture of milk powder products have a major influence on solubility. During standard powder manufacture, these protein interactions occur when the casein micelles come into close contact at the surface of fat globules and during concentrated heating.

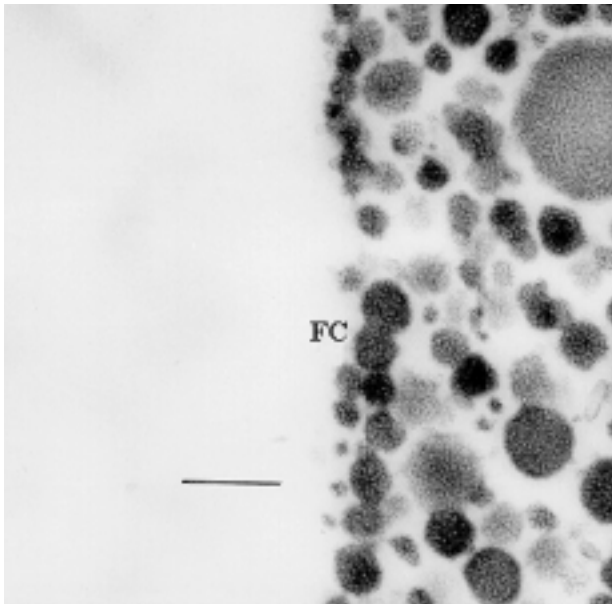

FIG. 1 Transmission electron micrograph of high protein skim milk powder showing fused casein micelles on the surface of the powder particle. FC = fused casein micelles. Bar = 0.2 μm.

During manufacture of high protein powders, the protein interactions occur when lactose is removed during ultrafiltration and diafiltration forcing the casein micelles close together. Upon spray drying the formation of an air/water interface is instrumental in forcing protein components into close contact. The interactions between proteins continue upon storage of the dry powders. This is particularly the case at the surface of the particles and at higher storage temperatures (Fig. 1).

Influence of Composition and Process Conditions on Microstructure of Amorphous Starch/Protein Powders

ANNEMARIE SCHOONMAN,* GUY MAYOR,*
CHRIS BISPERINK,† JOB UBBINK*

*Nestlé Research Center, CH-1000 Lausanne 26, Switzerland; †Current affiliation: DMV International, 5460 BA Veghel, The Netherlands

An important goal of food research is to develop desirable food structure and texture. Structure and texture in food are the result of interactions among the food components and the phase transitions induced in them during processing and storage. Here, we present an investigation of the physical and structural properties of maltodextrin/sodium caseinate powders as a function of composition and processing conditions.

Surface area, density and porosity of powders are known to be strongly affected by processing, composition, particle size, temperature and storage conditions. Nitrogen adsorption data were compared with data obtained from density measurements and with microscopic observations from image analysis. Powders are obtained by spray and freeze drying and differ in the volume of nitrogen injected into the maltodextrin DE 12 / sodium caseinate concentrate prior to drying. The percentage of proteins in the powders was also varied.

Nitrogen adsorption data were used to calculate the surface areas of various dried powders utilizing the Brunauer, Emmet and Teller (BET) method. Differences in the structure of dried foams, as affected by the composition of the powder and the volume of gas injected during the foaming process, were correlated with a variation in specific surface area. Measured surface areas were all below 5 m^2/g but varied by two orders of magnitude. The differences in surface areas are attributed to porosity effects and formation of cracks. The surface area increased with increasing volume of nitrogen injected and increasing amount of proteins in the powder.

Helium pycnometry measurements and microscopic data showed a strong influence of the percentage of sodium caseinate added to the concentrate on the porosity and microstructure of the powders. An increasing amount of sodium caseinate leads to higher porosities in powders with the same volume of nitrogen gas injected. As expected, the amount of nitrogen gas injected prior to drying is an important factor controlling the microstructure and bubble size distribution of the foam. A higher volume of injected nitrogen gas increases both the open and the closed porosity and diminishes the thickness of the wall between adjacent cells.

The bubble size distribution is shown to be different in freeze-dried and spray-dried powders. Freeze-dried powders show a more homogeneous distribution of the pores in the matrix.

Monitoring Moisture Mobility and Migration in Model Bilayered Food Systems by NMR, MRI, and Mechanical Assessment

YOA WANG, IRWIN A. TAUB AND ANN BARRETT

Combat Feeding Program, Natick Soldier Center, US Army SBCCOM, Natick MA

Model multi-layered food systems were designed in order to mimic the structure of actual sandwich-type products in which moisture content and water activity differ. Such a water activity gradient is the driving force for migration of moisture, which can affect product characteristics and stability.

In a model bread-barbeque chicken bilayer system, time-domain proton (^1H) nuclear magnetic resonance was employed to monitor the change in mobility of water in both layers[1], and also the migration of water from filler to bread. Specifically, the NMR longitudinal relaxation time (T_1) of water in the filler was initially higher than that in the bread; however, this difference was lessened after storage, indicating migration of water into the lower water activity bread layer. Migration was faster at high temperatures and was also retarded by incorporation of glycerol, which reduced water activity in both bread and filler. Moisture distribution profiles were furthermore visually captured through magnetic resonance imaging[2]. A linear relationship between proton NMR T_1 relaxation time and sample moisture content was determined, which provides a non-invasive method to assess moisture content in complex food systems.

In model bread-cheese sandwich systems, in which water activity gradients were varied by bread glycerol content, measurements of moisture migration were coupled with textural assessment of both the constructed sandwiches and individual components. Compressive force-deformation functions of components, prior to and after storage, were used to mathematically construct predicted force-deformation relationships of the composites[3]. Differences between the predicted and actual force-deformation functions were due to, and can be predictive of, migration of moisture.

These advanced techniques can be used to monitor and to assess the physical effects of water mobility/migration in multilayer foods.

References

Belton PS, Colquhoun IJ, Hills BP: 1993. Application of NMR to Food Science. In: *Annual Reports on NMR Spectroscopy*. Pp. 1-53. G.A. Webb, Editor. Academic Press, London.

Schmidt SJ, Lai HM: 1991. Use of NMR and MRI to Study Water Relations in Foods. Pp. 405-452. In: *Water Relationships in Food*. H. Levine and L. Slade, Editors. Plenum Press, New York.

Peleg M: 1993. Calculation of the Compressive Stress-Strain Relationships of Layered Arrays of Cellular Solids Using Equation Solving Computer Software. *Journal of Cellular Plastics*, 29:286-293.

Cryo-Electron Microscopy in the Biomedical Sciences

Electron Cryomicroscopy of Biological Assemblies

WAH CHIU

National Center for Macromolecular Imaging, Verna & Marrs McLean Department of Biochemistry and Molecular Biology, Baylor College of Medicine, Houston, TX, USA

Introduction

A fundamental theme in cell and molecular biology research centers is the structure-function relationships of macromolecular assemblies that are responsible for biological processes. X-ray crystallography and NMR spectroscopy are well-established approaches for obtaining atomic structures of individual macromolecules. However, many biologically active components cannot be studied readily using these techniques owing to their large size, biochemical/structural heterogeneity, or membrane association. Electron cyromicroscopy is an emerging structural technique that is superbly suited to study complex macromolecular assemblies of various sizes and forms, as occur in cells. These include filaments, bundles, membranes, ion channels, receptors, protein-nucleic acid complexes and viruses.

Experimental Method

Electron cyromicroscopic technique requires the specimens that have been highly purified so that the observed structures can be related to the well-defined molecular components. The concentration of the samples is less than 1mg/ml in a standard buffer. In general, one would avoid high salt, glycerol and sucrose in the sample. A 5 µl sample is applied to a grid which is either holey or has a thin carbon film across the holes. The sample is blotted by a filter paper and plunged into liquid ethane for quick freezing.[1] The frozen grid is transferred to a cyro-specimen transfer station in which the grid is loaded into the cyro-specimen holder. The frozen hydrated specimen is maintained at temperature below –165°C during the entire observation. Low dose (~10 electrons/Å^2) is used to record images. In this whole process of specimen preparation and data collection, the new investigators are usually frustrated by the unsuitable thickness of the embedding ice; the inappropriate concentration of the specimens on each grid area; the excessive ice contamination on the specimen; and the specimen movement seen in the micrograph. However, all of these problems can eventually be overcome through experience.

Data Analysis

Image recorded from frozen hydrated biological machines has low contrast partly due to the low dose and partly due to the choice of defocus to ensure the recording of the high-resolution data. In order to assess the data quality, it often requires an extensive computational analysis of the digitized image data. The computed diffraction pattern of the specimen area will show how far signal is detected in the Fourier space.[2] In order to retrieve the three-dimensional image of the biological assembly, one needs multiple images of the same object in different orientations.[3] The number of images needed to perform a reconstruction depends on the targeted resolution and size of the machine. The major tasks of image analysis are to determine and refine the orientations of each image of the machine; to make image corrections due to the contrast transfer function of the microscope and other experimental factors that dampen the high resolution Fourier amplitudes; and to merge the data coherently from machines recorded in different micrographs. Finally, the three-dimensional map of the assembly is computed and interpreted with advanced graphics tools. In some of the complex biological machines that are made up of multiple molecular components, its structural interpretations will be made simpler with animation made from the structure.[4]

Biological Applications

Electron cryomicroscopy is fundamentally a high-resolution tool.[5] For some biological molecules that form two-dimensional crystals, the application of electron cryomicroscopy has resulted in the determination of the tertiary fold of protein.[6] In instances where crystals cannot be formed, atomic resolution information can be gleaned by combining high resolution structures of individual components determined by X-ray crystallography or NMR with image-derived reconstructions at moderate resolution.[8] This can provide unique and critical information on the mechanism of these complexes such as actin, microtubule and ribosome. Finally, image reconstructions have been used as initial models that facilitate phasing of crystals of large assembly by X-ray diffraction analysis.[9,10]

Acknowledgment

This research has been supported by NCRR of NIH grant P41RR02250.

References

1. Dubochet J, *et al.*: Cryo-electron microscopy of vitrified specimens. *Q Rev Biophys* 21, 129–228 (1988)
2. Zhou ZH, Hardt S, Wang B, Sherman MB, Jakana J, Chiu W: CTF determination of images of ice-embedded single particles using a graphics interface. *J Struct Biol* 116, 216–22 (1996)
3. Crowther RA, Amos LA, Finch JT, De Rosier DJ, Klug A: Three-dimensional reconstructions of spherical viruses by Fourier synthesis from electron micrographs. *Nature* 226, 421–5 (1970)
4. Dougherty MT, Chiu W: Using animation to enhance 3D visualiztion: a strategy for a production and environment. In *Microscopy and Microanalysis* 452–453 (1998)
5. Chiu W, McGough A, Sherman MB, Schmid MF: High resolution electron cryomicroscopy of macromolecular assemblies. *Trends Cell Biol* 9, 154–159 (1999)
6. Henderson R, Baldwin JM, Ceska TA, Zemlin F, Beckmann E, Downing KH: Model for the structure of bacteriorhodopsin based on high-resolution electron cryomicroscopy. *J Mol Biol* 213, 899–929 (1990)
7. Nogales E, Wolf SG, Downing KH: Structure of the alpha beta tubulin dimer by electron crystallography. *Nature* 391, 199–203 (1998)
8. Milligan RA: Protein-protein interactions in the rigor actomysin complex. *Proc Natl Acad Sci USA* 93, 21–6 (1996)
9. Ban N, *et al.*: A 9 Å resolution X-ray crystallographic map of the large ribosomal subunit. *Cell* 93, 1105–15 (1998)
10. Prasad BVV, Hardy M, Dokland T, Bella J, Rossman MG, Estes MK: X-ray crystallographic structure of Norwak virus capsid. *Science* 286, 287–290 (1999)

Tandem Cryo-Scanning Transmission and Cryo-High Resolution Secondary Electron Microscopy (SE-I) of Bio-Molecular Complexes

ROBERT P. APKARIAN AND KEVIN L. CARAN

Integrated Microscopy and Microanalytical Facility, Department of Chemistry, Emory University, Atlanta, GA 30322

Cryo-electron microscopy methods are evolving into powerful tools for the spatial characterization of bio-molecular complexes assembled in nature and whose synthesis is genetically directed. Molecular studies that seek to elucidate cell function or characterize natural and synthetic bio-polymers are greatly complemented by cryo-electron microscopy. Bio-polymers composed of phospholipids, amino acid or nucleic acid sequences, are routinely analyzed spectroscopically (mass spectrometry and NMR) and by X-ray crystallography.[1,2] Additionally, these polymers are now characterized at the 1-10 nm level of resolution in isolated aqueous systems by tandem cryo-HRSEM/STEM. Large protein bio-polymers, organelles, vesicles, viruses and cells represent a challenge to spectroscopic techniques due to their complex biological compartmentalization. The context in which spectroscopic techniques can analyze molecular moieties is limited to purified and isolated preparations. Cryo-electron microscopy methods allow molecular imaging of systems composed of heterogeneous molecular entities such as integral membrane proteins that may function as receptors, and cell surface recognition and attachment sites.[3] Tandem cryo-HRSEM/STEM represents another approach to imaging vitrified thin specimens that complement cryo-TEM structural analysis.

Pure phospholipid vesicles and genetically engineered elastin-mimetic block copolymers are routinely cryo-immobilized in a vitreous film of ice on coated grids by plunging-freezing in liquid ethane (–183°C).[4] Aqueous suspensions (10 µl) of protein or phospholipid vesicles and coacervates are applied onto a carbon coated grid, blotted with either a capillary tube or filter paper, and plunge frozen in freshly melted ethane. Grids are mounted onto the Oxford CT-3500 cryoholder held within the preparation chamber at –170°C. Under a positive pressure with cooled and dry nitrogen gas the double shuttered cryoholder is transferred to a Denton DV-602 Cr coater and sputtered with a 1 nm thick film. Specimen temperature never rises above –168°C during the coating process. The cryoholder is transferred through the atmosphere and into the lens of a Topcon DS-130 Schottky field emission microscope, operated at 25kV. The specimen is constantly maintained below 1×10^{-7} torr throughout specimen stage heating to –110°C and imaging procedures. Tandem cryo-STEM/HRSEM imaging provides two recorded images (4.8 Mbytes/ea.) in 30-sec photoscans.

Monatomic chromium films provided rich contrasts of frozen-hydrated biopolymers in both recording modes without structural decoration and provide protection from beam damage. Although more modest levels of structural resolution are available (1–5 nm) with cryo-STEM/HRSEM than by cryo-TEM, topographic contrasts are readily available to assess tertiary features of protein polymers. Further, multiple recordings and complex computer reconstruction methods necessary to process low contrast cryo-TEM data are circumvented. The comparatively low voltage (25kV) source used on the DS-130F STEM/HRSEM and the microscope's ability to remove ice contamination on the coated specimen surface through in-lens sublimation greatly enhances specimen stability and recording accuracy.

The grid-plunge-freeze method and cryo-HRSEM have provided topographic data with vistas of viruses, fibronectin fibrils, phospholipid vesicles and elastin polymers.[5,6,7,8] Structural analysis of biological macromolecular complexes, both isolated and within biological compartments (cells) are further scrutinized by cryo-STEM phase contrasts and in tandem with cryo-HRSEM provide an excellent tools for molecular studies.

References

1. McMillan, R.A., Caran, K.L., Apkarian, R.P., Conticello, V.P. High resolution topographic imaging of environmentally responsive elastin-mimetic hydrogels under native conditions: evidence for structural rearrangements during the phase transition. *Macromolecules*. 1999: 32, 9067-9070.
2. Menger, F.M., Caran, K.L., Apkarian, R.P., In-lens cryo-high-resolution scanning electron microscopy of large vesicles. *Langmuir*. 2000: 16, 98-101.
3. Apkarian, R.P., Caran, K.L., Robinson, K.A. Topographic imaging of chromium-coated frozen-hydrated cell and macromolecular complexes by in-lens field emission Scanning Electron Microscopy. *Microsc. and Microanal*. 1999, 5:3, 197-207.
4. Ryan, K.P., Purse, D.H., Robinson, S.G., Wood., J.W. The relative efficiency of cryogens used for plunge-cooling biological specimens. *J. Microsc*. 1987, 145:1, 89-96.
5. Chen Y, Centonze VE, Nilbert ML, Borisy G (1994) Cryo-scanning electron microscopy of reovirus structure. *52nd Ann Proc Microsc Soc Amer* 134-135.
6. Chen Y, Zardi L, Pesciotta Peters DM (1997) High-resolution cryo-scanning electron microscopy study of the macromolecular structure of fibronectin fibrils. *Scanning* 19:349-355.
7. Caran, K.L., Apkarian, R.P., Menger, F.M. Examination of large unilamellar vesicles (LUVs) using cryo-HRSEM and cryo-STEM. *57th Ann. Proc. Microsc. Soc. America.* 1999: 1210-1211.
8. Qu, Y., Payne, S.C., Apkarian, R.P., and Conticello, V.P. Self-assembly of polypeptide multi-block copolymer modeled on arachnid dragline silk proteins. *J. Am. Chem. Soc*. 2000 (in-press).

Morphology of Fresh -Frozen Hydrated Platelets Assessed by Cryo-High Resolution Scanning Electron Microscopy

KEITH A. ROBINSON, PH.D., NICOLAS A.F. CHRONOS, M.D., ROBERT P. APKARIAN, PH.D.

Atlanta Cardiovascular Research Institute and Emory University, Atlanta, GA, USA

Novel cryo-immobilization and -imaging techniques allow the capacity to observe the morphology of cells without the artifactual distortions induced by chemical fixation and processing. In the case of blood platelets viewed by high-resolution scanning and scanning transmission electron microscopy novel cryo-imaging strategies provide the opportunity for observation of the cells in suspension in the hydrated state, and correlate surface and overall shape structural changes to functional assessments such as aggregometry in response to physiologic agonists. To assess the morphology of quiescent and stimulated blood platelets using this new technique, we obtained platelet-rich plasma (PRP) from pigs and human donors.

Whole blood (26 ml) was obtained by needle puncture of the median ear artery (pig) or cephalic vein (human) and mixed with 3 ml acidified citrated dextrose solution. Platelets were isolated by standard techniques and examined in the resting state or after stimulation with the physiologically relevant agonists thrombin (human and pig), collagen and adenosine diphosphate (pig only). Platelet suspensions were pipetted into gold carriers or onto formvar-coated copper mesh grids and cryofixed by plunging into liquid ethane (–183°C). The sample preparation and imaging strategy has been described in detail by Apkarian *et al.*[1] Briefly, following plunge freezing and for holders, cryofracture, samples were loaded into an Oxford Instruments preparation chamber. They were then transferred into the chamber of a Cr coater (Denton DV-602) with the stage and specimen maintained below –150°C. With an appropriate vacuum obtained, a 1 nm Cr film was deposited following which the samples were shuttled through atmosphere to the in-lens stage of the electron microscope. During this transfer the stage temperature did not rise above –120°C. The DS-130F microscope (Topcon, beam diameter ~1 nm) with in-lens CT-3500 Oxford cryo-stage fitted with dual cold finger anti-contamination traps and a Varian 860 cold cathode discharge gauge for monitoring the vacuum at the specimen was used for documentation of platelet morphology at high magnification and resolution. The microscope was operated at 25kV and the specimens imaged at temperatures of –110°C and –160°C; the cold stage was warmed to –110°C to sublime away ice crystals formed during transfer to the microscope. Images (4.8 Mb) were recorded with a Pentium based GW video capture board and processed with Adobe Photoshop as tagged image format (TIF) files. The images were used to assess platelet and platelet microparticle size and morphologic features of activation.

In samples from pig and human whole platelets were clearly visible at low magnification (~2000X) on the fractured surface of the frozen PRP droplet. There was no evidence of fracture planes that extended into the cell interior. Control platelets were consistently discoid in shape and displayed smooth plasma membranes with occasional evidence of curvilinear steps or folds at the disc edges. In contrast stimulated platelets were considerably larger size and often showed ~50–200 nm surface blebs which may correspond to platelet microparticles known to form after activation with various agonists. In the case of thrombin stimulation, prominent pseudopodia and cytoplasmic densities were also observed. For human platelets, various stages of activation were clearly delineated within the sample stimulated with thrombin 0.5 units/ml; fully dendritic platelets with striking stellate morphology were also detected. The above changes were obtained at the effective concentration to induce ~50% of maximum aggregation (EC_{50}) and thus were correlated to aggregometry.

These experiments demonstrate the feasibility of a new technique to evaluate the morphology of unfixed blood platelets using a simple preparation method.[1] Furthermore we have shown the capacity to distinguish marked changes in platelet surface morphology very early after activation with physiologically relevant agonists.[2] In a manner similar to previous studies this method can be used to correlate platelet morphology to functionally significant responses.[3] Ongoing studies will be focused on refining

platelet preparation methods, extending the range of activation conditions, surface epitope labeling, and correlation with existing analytical techniques such as platelet aggregometry and flow cytometry.

Bibliography

1. Apkarian RP, Caran KL, Robinson KA. Topographic imaging of chromium-coated frozen-hydrated cells and macromolecular complexes by in-lens field emission SEM. *Microsc Microanal* 1999;5:197–207.
2. Wendt MC, Robinson KA, Chronos NAF, Caran KL, Apkarian RP. Application of high resolution (HR) SEM technique for imaging platelet morphology. *Microsc Microanal* 1999;5(Supp II):1116–1117.
3. Albrecht RM, Goodman SL, Simmons SR. Distribution and movement of membrane-associated platelet glycoproteins: use of colloidal gold with correlative video-enhanced light microscopy, low-voltage high-resolution scanning electron microscopy, and high-voltage transmission electron microscopy. *Am J of Anat* 1989;185:149–164.

Electron Backscattering Patterns

Channeling Effects in the Electron Microscope

S. J. PENNYCOOK

Solid State Division, Oak Ridge National Laboratory, Oak Ridge, Tennessee, USA

Electron channeling patterns come in many forms: electron backscattering patterns in the scanning electron microscope, electron channeling patterns in the scanning transmission electron microscope, and Kikuchi patterns in the transmission electron microscope. All have a common physical origin, and can be described either through a wave picture (diffraction) or a particle picture (channeling). The physical basis of these phenomena have been considered, while attempting to portray the correct quantum mechanical viewpoint in a non-mathematical manner, introducing the concepts of Bloch waves, diffraction channeling and a localized scattering event. This is sufficient to explain the similarity of electron channeling patterns and electron backscattering patterns through the principle of reciprocity. These patterns are formed using a large detector to integrate over the scattered electron distribution, and are seen even from thin specimens. Kikuchi lines in transmission electron diffraction require thicker specimens to "fill in" between the sharp diffraction spots through multiple scattering events which then allow the channeling effects to be seen.

Resolution Concerns in Electron Backscatter Diffraction

D.J.DINGLEY

TexSEM Laboratories and EDAX, Draper, Utah

There are three aspects of resolution in electron backscatter diffraction that need to be addressed. The first is lattice spacing measurements extracted directly from the backscatter diffraction pattern. The second is the precision and accuracy of orientation measurement and the third is the spatial resolution of EBSD measurements.

The standard measurement of lattice spacing derives from the width of the Kikuchi bands and this provides a precision of 1 in 20. Use of Holtz rings surrounding prominent zone axes can improve this to 1 in 100 in favorable patterns. Lattice parameter measurements on the other hand can be obtained from points at which three Kikuchi lines intersect. These measurements provide values slightly better than 1 in 100. Statistical combinations can improve lattice parameter to 1 in 200.

Accuracy in the measurement of absolute orientations is determined by sample mounting procedures. Relative orientations are independent of the sample mount and depend entirely on accuracy of detecting the positions of the Kikuchi bands. Precision to better than 0.5 degrees is not uncommon.

Spatial resolution can be defined as the smallest distance over which a change in crystal phase or orientation can be determined. This depends on two factors, the volume from which EBSD patterns are generated and the ability of indexing software to deconvolute overlapping patterns. The former factor depends on the microscope operating voltage and electron beam diameter. Deconvolution of patterns requires clear identification of lines from both patterns and on the sampling procedures used in the indexing algorithm.

Pharmaceutics

Novel High Resolution Measurement of Bone Mineralite Size and Shape

STEVEN J. EPPELL,* WEIDONG TONG,* LISA KUHN,† MELVIN GLIMCHER†

*Dept. of Biomedical Engineering, Case Western Reserve University, Cleveland, OH; †Department of Orthopaedic Surgery, Harvard Medical School, Boston, MA

Advances in arthroplasty, tumor surgery and chemotherapy would all benefit from a superior bone substitute material. This ideal material would provide temporary mechanical support, allow for the controlled release of therapeutic

agents, and be amenable to normal physiological remodeling resulting in a native bony structure. A few commercial products are available to fill this need (i.e. Wright Medical Technology's Osteoset™ and Zimmer's Collagraft.™). Several groups have been active in exploring the mechanical, biological and pharmacokinetic properties of these and other potential substitute materials. The great majority of these materials utilize a powdered mineral component with characteristic dimensions >0.5 μm and most of them utilize hydroxyapatite as the chemical of choice.

As a first step in analyzing the mechanism by which these materials interact with the biological environment, we directly measured the full three dimensional shape of purified bone mineralites. This information is difficult to come by for three reasons: it is difficult to isolate the mineralites without changing them, they are poorly crystalline making unequivocal X-ray diffraction data difficult to obtain, electron microscopies providing projection data of supported mineralites have left open the question of mineralite thickness.

We isolated mineralites using a previously published method involving hydrazine extraction and plasma ashing. Mineralites were dispersed by sonication in a chilled 100% ethanol solution and aliquoted directly onto a cleaved mica surface. Residual ethanol was evaporated in a desicator for ~12 hours. Subsequently samples were imaged using an atomic force microscope (AFM). Deposition conditions were adjusted so that individual mineralites were well separated on the surface. Images were processed using mathematical morphology to remove tip broadening. These filtered images were analyzed by taking two line scans through the mid-point of each mineralite: one along the long axis and one along the intermediate axis of the mineralite.

Measurements taken from 280 individual mineralites residing in different locations on several samples revealed two classes of mineralites: thick (having heights >2 nm) and thin (having heights < 2 nm). By number, ~98% of the mineralites were thin. However, the Ca ions were approximately equally divided between the thick and thin mineralites. Concentrating our analysis on the thin mineralites showed monomodal distributions of heights and widths: mean height = 0.61 nm ± 0.19 nm, mean width = 10 nm ± 2.8 nm. The lengths generally displayed a multimodal distribution with peaks separated by ~6 nm suggesting that the fundamental building block of the mineral component of bone is a plate having dimensions of ~6 nm × 10 nm × 0.61 nm. These blocks then assemble by adding units preferentially along one axis with the dominant structure being a dimer having dimensions of 12 nm × 10 nm × 0.61 nm. This finding is consistent with the suggestion of Landis *et al.* that bone mineralites are constructed by fusion of small individual pieces. This could be accomplished with formation of a grain boundary or other low order assembly requiring less activation energy than needed to form a single crystal. There was some correlation between width and length with the best-fit line having a slope of ~0.5. The mean length:height ratio of the thin mineralites was 20.3 ± 5.6 (a thin plate like shape) in stark contrast to the mean ratio for the thick mineralites of 2.7 ± 1.1 (a nearly cuboidal shape).

In summary, we have demonstrated that AFM is capable of providing information regarding the structure of bone on a size scale commensurate with x-ray diffraction and transmission electron microscopy. Our data show that mature bovine cortical bone mineralites are predominantly plate like in shape, having a mean length/thickness ratio of 20.3. These mineralites appear to be one unit cell thick, to grow preferentially along one axis, and to have mean dimensions of 12 nm × 10 nm × 0.61 nm. About two percent of the mineralites have orders of magnitude larger thickness values and are not plate like in shape, having a mean length/thickness ratio around 2.7.

Imaging of Pharmaceutical Excipients by Time-of-Flight, Secondary Ion Mass Spectrometry

MARK NICHOLAS

Analytical Research, AstraZeneca R&D Mölndal, Mölndal, Sweden

TOF-SIMS is useful in the pharmaceutical industry for the analysis of solid dosage forms. TOF-SIMS chemical images can be used to show the location of the drug and excipients as formulated and to monitor physical or chemical changes in the formulation as a function of time, temperature, and humidity. Physical changes could include interlayer movement of drug or excipients, for example.

Time-of-flight, secondary ion mass spectrometry (TOF-SIMS) is a microanalytical technique which is capable of chemical imaging of solid surfaces with submicron (for atomic ions) to micron (for polyatomic ions) lateral resolution. A tightly-focussed (~0.2μm), high-energy (25keV), $^{69}Ga^{+}$ primary ion beam deposits energy in the sample surface. Randomization of this energy results in secondary ions being forced from the top 1nm near the impact site. These ions are pulled into a mass spectrometer for mass analysis.

The raw data file generated in such an analysis includes both the flight times for each ion detected and the position of the ion beam when the ion was produced. This information permits the analyst to plot intensity for a selected ion as a function of position on the sample surface and to do so after the analysis has been completed.

A mixture of three pharmaceutical excipients [hydroxypropyl cellulose (HPC), hydroxypropyl methylcellulose (HPMC), and hydroxypropyl methylcellulose phthalate (HPMC-P)] is used as a model system to investigate options for processing of raw TOF-SIMS data. The mixture was made by simply grinding the three compounds together using an agate mortar and pestle and taking a random sample for analysis.

The default condition for the chemical imaging of a mixture of this nature is to choose a characteristic ion for each compound and to produce images of these ions. For a polymeric compound, such as those of this model system, the characteristic ion is only one of the hundreds of fragment ions arising from the compound. The ion which is most useful in differentiating one component from the others in the mixture which is chosen. For HPC, HPMC, and HPMC-P in the positive ion mode, $C_3H_7O^+$, $C_2H_5O^+$, and $C_8H_5O_3^+$, respectively, are imaged. To create a composite image, colors are assigned to each of the images: $C_3H_7O^+$ (blue), $C_2H_5O^+$ (green), and $C_8H_5O_3^+$ (red). In addition, images of sodium (Na^+) and silicon (Si^+) impurities are assigned yellow and magenta, respectively. [The resulting summed image (Fig. 1b) shows the HPMC-P as orange due to the high levels of $C_8H_5O_3^+$ *and* $C_2H_5O^+$ in the spectrum of HPMC-P. The total ion image (Fig. 1a) shows that the ion intensity in a TOF-SIMS image is affected by topography.]

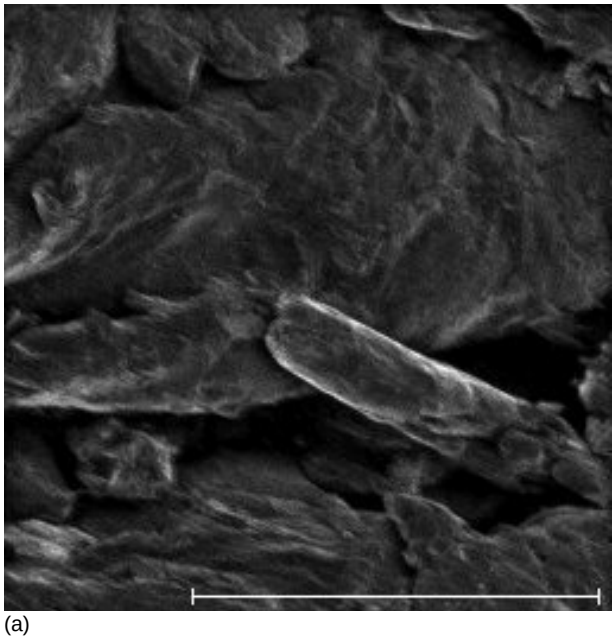

(a)

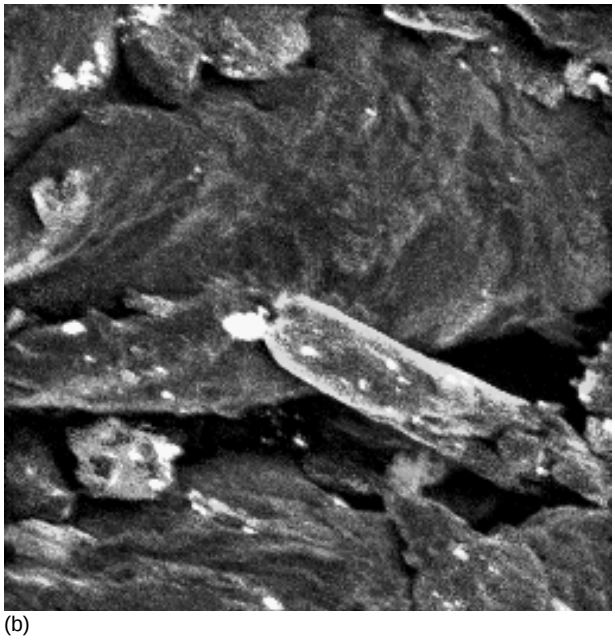

(b)

FIG. 1 TOF-SIMS ion images of a mixture of HPC, HPMC, and HPMC-P. (a) Total ion image showing variation in secondary ion yield with topography. The bar is 100µm. (b) Composite image: HPC (blue), HPMC (green), HPMC-P (orange), sodium (yellow), and silicon (magenta).

One disadvantage of this approach is that much signal is being thrown away, since only one ion out of the entire fragmentation spectrum for each compound is being used. Furthermore, one characteristic ion per compound may be insufficient to differentiate between two components if they have very similar mass spectra. An alternative to this univariate approach is to image a new variable (composed of a weighted sum of the entire mass spectrum) which is even more characteristic of a given compound than is any single ion. This possibility plus the possibility of automating the entire ion selection and imaging process is what is offered by the use of principal components analysis, partial least squares regression, and other multivariate techniques.

Protective Effects of Melatonin as a Free Radical Scavenger in the Formation of Gastric Ulcer: A Light And Scanning Electron Microscope Study

G. ŞENER,* K. PASKALOĞLU,* S. ARBAK†, C. HÜRDAĞ,† G. AYANOĞLU-DÜLGER*

School of Pharmacy, *Dept. of Pharmacology and School of Medicine, †Dept. of Histology and Embryology, Marmara University, Istanbul, Turkey

Introduction

Nonsteroidal anti-inflammatory drugs (NSAIDs) are considered to be a risk factor in causing GI damage and development of gastroduodenal ulcers. More recently, direct involvement of oxygen-derived free radicals has been implicated in the mechanism of gastrointestinal ulceration.[1,2] Omeprazole and famotidine are among the most widely used anti-ulcer drugs and are known to be effective inhibitors of gastric acid secretion.[3,4] They have also been demonstrated to have a protective effect against experimentally induced gastric lesions and this was attributed to their anti-secretory effects as well as their direct cyto-protective effects. On the other hand, *in vivo* and *in vitro* studies have demonstrated the antioxidant properties of pineal hormone melatonin, and it was shown to scavenge both the hydroxyl and peroxyl radicals. The present study was planned to investigate the cytoprotective role of melatonin by comparing its protective effect against sali-

cylate induced gastric lesions with that of omeprazole and famotidine.

Materials and Methods

Wistar albino rats were divided into 6 groups (n: 7): 1) control group; 2) starvation group, deprived of food for 3 and 48 h before death; 3) ASA group (200 mg/kg aspirin orally, suspended in 1 % methyl cellulose in water); 4) famotidine group (40 mg/kg famotidine, 3 h before ASA; 5) omeprazole group (20 µmol/kg omeprazol, 1 h before ASA; 6) melatonin group (10 mg/kg melatonin i.p., 30 min before ASA)

Gastric acidity, gastric tissue glutathione, lipid peroxidation and myeloperoxidase levels were determined in gastric tissue of experimental groups. For light microscopy, samples were fixed in 10 % formalin solution and stained with haematoxylin and eosin, whereas for scanning electron microscopy, samples underwent 2.5 % phosphate-buffered glutaraldehyde fixation. Following routine processes, sections were investigated by light and scanning electron microscopes.

Results

Pre-treatment of Wistar albino rats with omeprazole, famotidine and melatonin significantly decreased the ulcer index. Gastric lipid peroxidation, glutathione and myeloperoxidase activity, which were increased significantly by acetyl salicylic acid, were decreased by omeprazole, famotidine and melatonin. Light microscopy indicated that the degree of surface epithelial damage, hemorrhage, leukocyte infiltration and glandular degeneration in the lamina propria due to acetyl salicylic acid administration were in lesser degree in the omeprazole and famotidine group as compared to the ASA group, while melatonin group sections represented a minimal degree of mucosal damage. Scanning electron microscopical observations revealed that epithelial desquamation and hemorrhage were minimal in the melatonin group, whereas a moderate degree of exposed lamina propria due to epithelial desquamation, fibrin deposits and echinocytes, suggested mucosal damage in the famotidine and omeprazole groups.

Discussion and Conclusion

Investigators[1–4] proposed that gastric mucosa free radicals and lipid peroxides are injurious, offensive factors, and glutathione is a protecting factor. Acetyl salicilic acid may contribute to gastric injury through a variety of mechanisms, among which glutathione depletion and lipid peroxidation increase. Melatonin, while inhibiting lipid peroxidation, helped in preservation of glutathione levels by providing its strong antioxidant ability. Omeprazole and famotidine inhibited glutathione depletion in proportion to their efficiency as antioxidants. These findings suggest that active oxygene species and lipid peroxidation have an important role in the formation of gastric mucosal damage caused by acetyl salicylic acid and both omeprazole and famotidine may protect the gastric tissue against this damage, although they were not as efficient as melatonin.

References

1. Alican I, Toker F, Arbak S, Yeğen BÇ, Yalçin AS, Oktay Ş: Gastric lipid peroxidation, glutathione and calcium channel blockers in the stress- induced ulcer model in rats. Pharmacol Res, 30(2) : 123–135, 1994
2. Pihan G, Regillo C, Szabo S: Free radicals and lipid peroxidation in ethanol- or aspirin –induced gastric mucosal injury. Dig Dis Sci, 32(12): 1395–1402, 1987
3. van Zyl JM, Kriegler A, van der Walt BJ: Anti-oxidant properties of H2 reseptor antagonists. Biochem Pharmacol, 45 (12): 2389–2396, 1993
4. Lapenna D, Gioia S, Ciofani G, Festi D, Cuccurullo F: Antioxidant properties of omeprazole: FEBS Lett, 382: 189–192, 1996

Proniosomes: Characterization of a Novel Formulation for Hydrophobic Drug Delivery

DAVID G. RHODES AND ALMIRA BLAZEK

Department of Pharmaceutical Sciences, University of Connecticut School of Pharmacy, Storrs, CT, USA

Many of the most active drugs have minimal aqueous solubility. Delivery of hydrophobic or amphiphilic drugs is a long-standing challenge for the pharmaceutical scientist. Among the available formulations are liposomes or similar assemblies of nonionic surfactant called niosomes. Niosomes are effective carriers because hydrophobic drugs can partition into the hydrophobic portion of a multilamellar niosome and then be released slowly as the niosome degrades *in vivo*. Niosomes are an improvement over liposomes, because of the low cost of materials and decreased susceptibility to enzymatic degradation. Unfortunately, like liposomes, aqueous suspensions of niosomes are still susceptible to physical degradation and hydrolysis.

Our group has developed a dry formulation, called "proniosomes," which can quickly produce high quality niosomes [Hu,C. and Rhodes, D.G. (1999) Proniosomes: A Novel Drug Carrier Preparation. Int. J. Pharmaceutics 185; 23-35]. The proniosomes are prepared by coating carrier particles with the niosome components: Span, dicetyl phosphate, cholesterol, and drug. Because proniosomes are dry until being reconstituted for use, the carrier and drug are less susceptible to hydrolytic degradation. Because the proniosomes can be produced immediately prior to use, they are not subject to physical degradation by aggregation or precipitation. Characterization of proniosomes and proniosome-derived niosomes using transmission and scanning electron microscopy and other methods has shown that this preparation yields a superior product in terms of uniformity and release characteristics. We recently developed

a new formulation based on coated hollow spheres of soluble carrier. The key advantage of this system is that the amount of dissolved carrier which accompanies the dose can be minimized. Using this system, we have been able to optimize the particle loading to produce a proniosome whose physical and chemical characteristics make it an excellent candidate for a new dosage form.

Niosomes were originally produced with 0.2 g surfactant/g carrier (sorbitol), and were produced using a time consuming batch process. Due to the solubility of the carrier powder, the rate of application was severely limited. If solvent were not allowed to evaporate, a slurry would form and the powder particle morphology would change markedly. Several higher throughput approaches were attempted and most niosome characteristics were not affected significantly by this variation. Still, the production was limited by the carrier solubility, and rapid mass production was not likely to be feasible. Moreover, upon dissolution of the proniosomes, a high concentration of dissolved carrier affected the entrapment of the drug. Efforts to use less soluble carriers such as cellulose derivatives or silicates were not successful due to high concentrations of large particulate which were left in solution upon reconstitution.

A novel approach has now been developed based on a safe, approved carrier material, maltodextrin. The maltodextrin powders were available in a number of different particle morphologies and were found to be insoluble in chloroform. Because the carrier was water soluble, however, no large residue was left following reconstitution. In addition, because the carrier was insoluble in organic solvent, the rate of sample application could be greatly increased and a wider range of sample loading conditions could be tested. Further, a hollow particle carrier has been tested which allows significant reduction in the carrier mass required to support a surfactant film. At present, it has been demonstrated that high quality niosomes can be produced with loading up to 27 g surfactant / g carrier. Using this system, particle loading has only a minor effect on the properties of the niosomes.

Based on the characterizations performed to date, this novel process appears to be capable of reproducibly making large quantities of proniosomes. Compared to conventional niosomes, proniosome-derived niosomes are more uniform and have very reproducible release properties.

Supported by funding from NIGMS GM55973.

Thursday, May 11

Applications of SEM in Forensic Science

Latest Developments in Analytical Forensic SEMs

J.P. KRÜSEMANN

Electron Optics Division, FEI Company, Eindhoven, The Netherlands

Environmental Scanning Electron Microscope (ESEM)

One of the latest developments in microscopy is the environmental scanning electron microscope (ESEM). The ESEM allows imaging and analysis of uncoated, otherwise vacuum unstable, specimens. The ESEM offers the possibility to image the specimen surface in a gaseous environment (using water vapour) at chamber pressures in the range of 0.1 to 1.0 Torr. Imaging is done by employing backscatter detection, for atomic number contrast, or the dedicated gaseous secondary electron detector (GSED) for secondary electron imaging giving topographic information. When operating in the "low vacuum" range it is the ideal scanning electron microscope for all forensic investigations. This SEM is very suitable for imaging non-conducting materials at high kV. For many materials such as plastics, polymers, glass, wood, paints, fibres, hairs, fingerprints, insects, etc., the ESEM allows these types of specimen to be viewed in the natural uncoated state.

It can also be used as traditional high vacuum SEM.

Gunshot residue analysis

In forensic sciences, gunshot residue analysis is an important issue. The analysis of gunshot residue (GSR) can be performed through dedicated GSR software ensuring reliable, fast and fully unattended analysis—if desired, even in an overnight period of time. The software also identifies other indicative particles like the particles which originate from the bullet, containing a large amount of lead (Pb). Other particles of interest are titanium (Ti) and zinc (Zn) as found in lead free ammunition. Also other more environmental related particles can be characterised by the system to provide additional information about the suspect and crime scene.

Using GSR under low vacuum conditions has a large benefit. The samples do not require any conductive coating, thus no destruction of the evidence will occur. Using water vapour as a gas will eliminate the charging effects of non-conducting particles and fibres on the uncoated sample.

The GSR software employs the latest advances in X-ray spectrum processing techniques by combining region of interest (ROI), spectrum stripping routines and rule-based (intelligent) analysis methods. These methods provide the

flexibility needed to correctly interpret the spectra from inhomogeneous, often irregular and small particles.

The choice between different chamber conditions makes the ESEM the solution for a wide variety of GSR applications.

Classification of Pipe Bomb Fragments Using Optical Microscopy and Scanning Electron Microscopy

M.J. Platek, O.J. Gregory,* C. Cummisky,* Q. Lou,* J.C. Oxley,† J.L. Smith,† E. Resende†

Department of Electrical and Computer Engineering, URI; *Chemical Engineering Dept., URI; †Chemistry Dept., URI, USA

This study is a continuation of a much larger research program started more than a year ago to correlate the energy of the propellant used in pipe bombs to the number of fragments produced and the microstructure and fracture surface morphology of individual bomb fragments. Initially, this work compared the relative amounts of flat face fracture (planar shear surfaces) and fibrous fracture on individual fragments with the energy of the propellants used and the number of fragments produced for a given type and size of bomb. This SEM investigation focused on the fragmentation of relatively thick walled pipes that are commonly employed in bombs. The pipes were made of AISI 1030 steel, with an as received microstructure consisting of alpha ferrite and pearlite. Since the ratio of the pipe diameter to the wall thickness was approximately 15:1, and must be > 20:1 to have only biaxial stresses acting on the wall, it was assumed that triaxial stress states existed within the wall of the pipe. Consistent with this stress state in thick wall pipes, higher energy propellants such as bullseye yielded fracture surfaces with more planar shear and fewer fibrous features than those fracture surfaces associated with lower energy propellants such as black powder.

These findings led to the investigation of microstructural changes within the fragments using optical microscopy. The average grain size and aspect ratio of individual grains were evaluated for pipe bomb fragments produced from different propellants. It was observed that low energy propellants produced an equiaxed grain structure (consisting of alpha ferrite grains and isolated pearlite colonies) and moderately energetic propellants produced elongated ferrite grains with distorted slip bands. Higher energy propellants resulted in elongated ferrite grains and highly distorted slip bands as well as the presence of twins in the ferrite grains. Preliminary indications also revealed a variation in the microstructure across the fragment (through thickness) as might be expected with thick fragments that are under a triaxial stress state. Measurements of the reduction in wall thickness for the different propellants used were made and the macroscopic strain within the individual fragments was consistent with the extent of deformation of the ferrite grains. Finally, the microstructures obtained from optical microscopy were cross-referenced with the surface morphology using the scanning electron microscope.

Murder or Suicide—In-depth Investigation Finds the Truth

Eric Nelson, David Frey,* Wayne Niemeyer†

Former Assistant District Attorney, Richmond County, Brooklyn, New York; *Office of the District Attorney, Richmond County, Staten Island, New York; †McCrone Associates, Inc., Westmont, Illinois, USA

On the morning of November 4, 1996 a man called "911" saying that his wife was dead. Responding personnel were told by the husband that his wife committed suicide.

She was found, face up, in bed with her head lying in the middle of a pillow and her right hand, palm up, lying on the pillow to the right side of her head. A single gunshot was found through the pillow under her head and near her right hand. Crime scene detectives determined that the gun had been discharged at a 46 degree angle to the horizontal plane of the bed away from her head and that the gun was fired from a distance of ½″ to 2″ away from the pillow case.

The handgun, a .25 caliber semi-automatic pistol, was found on the foot of the bed by her left foot. The husband claimed he found the gun near the left thigh, picked it up in "anger" and accidentally discharged the gun towards an open walk-in closet. Investigators found no evidence of ballistics damage near the closet. Blood was found on the gun but there was no indication of high velocity spatter, nor was there any indication of high velocity spatter on the bedding materials.

A second pillow was found on the deceased's mid-section and had two perforations in the pillow case but no penetration into the pillow. The crime lab determined that the perforations were consistent with a gun firing at loose contact against the pillow case with a crease or fold.

The medical examiner found no evidence of residues in the hair near the entrance wound, no tattooing, stippling, or soot. There was no evidence of singeing by the wound, on the face, or the right hand. The right hand also had no evidence of visible gunshot residue.

Investigators reconstructed the crime scene for further testing. An FBI Visual Information Specialist was asked to conduct computer simulations to determine if the gunshot wound could have been self-inflicted. Test firings were also conducted with the handgun using similar pillows and pillow cases. Only with a wrapped gun were the holes in the pillow case found on the victim's mid-section perfectly recreated. Recreations, live and computer simulated, revealed that, even at a minimum distance of 6″, it would

have been impossible for the decedent to have fired the killing shot.

SEM tape lift stubs were used by the medical examiner to obtain tape lift samples from the decedent's right hand, face, and left hand for testing at McCrone Associates to determine the presence/absence of gunshot residue (GSR). The results revealed:

1) 42 particles on the right hand stub
2) 0 particles on the face stub
3) 0 particles on the left hand stub

The decedent's nightgown was also sent to McCrone lab for additional tape lift analysis of the right and left arm/shoulder areas. The results revealed:

1) 7 particles on the right sleeve
2) 0 particles on the left sleeve

These results were not consistent with a suicide due to so few GSR particles found. To illustrate the inconsistency, additional tests were conducted at the crime lab in which the handgun was thoroughly cleaned before test firings by a female detective. Tape lift samplings were made from the shooting hand after each firing and a total of four SEM stubs were analyzed. Each stub contained hundreds/thousands of GSR particles.

The GSR particle results from the decedent were more consistent with particle transfer from the pillow under her head or from being touched by the shooter, suspected by the investigators to be the husband.

Crime scene recreations, computer simulations, lack of GSR on the decedent, led investigators to the conclusion that the victim's death could not have been the result of a suicide. Confronted with overwhelming evidence, the woman's husband pleaded guilty to killing her.

Multiple Line Scanning of Elemental X-rays: Sulfur Index of Hair and Other Forensic Applications

SAMARENDRA BASU

Albany State University, Albany, Georgia, USA

"Deflection modulation imaging of elements" in the scanning electron microscope (SEM) with energy-dispersive X-rays (EDX) is designed to produce a desired large number of X-ray line scans across the sample surface by deflection modulation (DM) of the scan signal (***Y***) in the line scanning mode. A modification of the speed and time for X and Y scans of the analog scan generator, the ability to vary the number of lines per frame (e.g. 48–100, 110–375, etc.) in an automated manner by a potentiometer for the X-speed, and the ability to remove the X-ray continuum and noise by a threshold setting to countrate, underscore the technicalities of this image processing technique (Basu, 1990). This technique has been utilized in this report as a *fingerprint technique* for qualitative area distribution analysis of individual elements present in trace evidence, such as gunshot residue (GSR) particles, metallic scrapings, glass fragments, and human head hairs. The most interesting observation to be confirmed here is the sudden rise in the uptake of sulfur within the endodermal portion of the root of scalp hair. This parameter was previously termed "Sulfur Index" (S-index) (Basu, 1986a). It has been shown in this report that this parameter varies remarkably from one individual to another.

The DM line scanning technique uses a line scan ratemeter to accept and to smooth out an elemental window signal from a multichannel analyzer of a spectrometer (EDAX Si-Li), and then to provide an attenuated analog DC output for vertical deflection (*Y*) on the CRT screen of an AMR 1000 SEM. Except for the "tailing effect" due to R-C distortion, all other problems of analog line scanning are avoided. The recording time is 30 min, 40 sec for each elemental image. Whenever necessary the sample image is superimposed on the DM image. Gunshot residue particles (GSR) were collected by police officers with field-ready kits prepared by a modified "glue-lift" technique in which toluene was used as a solvent for rubber cement (Basu, 1986b). Both plucked and combed hairs with attached roots were sonicated to have no or little attached sheath cells. The S-index (dIs/dx cpm per cm at x = 0, proximal end) was determined from measurements of the background corrected Sk - intensity in the "spot mode" at several distances up to about 1.5 cm from the proximal end of each hair.

The DM line scanning technique accentuates both concentration and topography dependent X-ray intensity variations. With smooth surfaces, such as base plate of victim's watch, watch band and glass fragments of the crime scene, the concentration dependence of the X-ray intensity predominates. The elemental images of these show losses or removal of thin platings and/or surface textures by friction. The scraped trace evidence are found on suspect's clothing, suggesting that these were exchanged as per Locard's principle (Locard, 1928). With spheroidal and irregular objects, such as GSR, the elemental images are pseudotopographic but they suggest homogeneous condensation of elements (Pb, Sb, Ba), particularly in micron or half-micron size particles. The S-indices of 23 individuals measured in the "spot mode" and confirmed by DM line scanning were found to be in an unusually wide range; namely, from 200 to 420,000 cpm/cm, and they are all different for these individuals. The S-index technique has passed a proficiency test and should be tried in casework when statistical data is obtained to individualize human head hair.

The DM line scanning technique is clearly a novel technique for producing visually improved elemental distribution images of trace evidence. This technique can be a useful tool for examining minute toolmarks, condensed matter, cometary dusts, microchips, electroplating, electrolysis, and corrosion.

References

Basu S: Hair comparison in the sem-edx based upon increased sulfur intensity along the length of hair: Evidence of a sulfur pump. In *Microbeam Analysis - 1986.* (AD Romig, Jr, WF Chambers, Eds). San Francisco Press, San Francisco, Proceedings MAS/EMSA meeting (1986a) 457–460

Basu S: The mechanism of gunshot residue deposition and its probing characteristics to reconstruct shootings. In *Electron Microscopy in Forensic, Occupational, and Environmental Health Sciences* (S Basu, JR Millette, Eds). Plenum Press, New York (1986b) 1–22

Basu S: Deflection modulation imaging of elements in the scanning electron microscope with energy-dispersive x-rays. *J. Comput. Assisted Microscop* 2(1), 25–45 (1990)

Locard E: Dust and its analysis. *The Police Journal* 1(1), 177-192 (1928)

SEM Analysis of Trace Evidence in the RCMP Forensic Laboratories

JACQUELINE DEMERS-KOHLS

Royal Canadian Mounted Police, Central Forensic Laboratory, Ottawa, Ontario, Canada

Scanning electron microscopy/energy dispersive x-ray (SEM/EDX) analysis has been an integral part of forensic casework at the Royal Canadian Mounted Police. The Canadian federal police force has a total of six laboratories across Canada, two of which are equipped with SEM/EDX.

SEM is a powerful tool in the analysis of trace evidence. Equipped with an EDX detector and a wavelength dispersive X-ray detector (WDX), it can be used in the identification of elements, sample comparisons and physical matches. Following are some SEM considerations used in casework conducted at the Central Forensic Laboratory.

Identification of elements:

Explosives: The most common explosive seen in SEM analysis is the emulsion explosive. Many of its components are easily identified using SEM/EDX. Several compositions exist, but the most common components are glass microballoons, aluminum flakes, sodium and ammonium nitrates, and iron oxide. Most explosives are sensitive to the beam, and care must be taken when selecting the SEM conditions—low accelerating voltage (kV) and probe current are suggested.

When searching residue for detonator cap fragments, one should look for metal (usually aluminum) with crevasses and crimps that might contain elements indicative of detonator material, such as lead particulate and occasionally Ba/S.

Ammunition Analysis: By Canadian law, shots used to hunt migratory birds must be "non-toxic" (<1% lead). For SEM analysis, each shot is embedded in quick setting epoxy and ground down to reveal the inner matrix. Because lead is a soft metal, each shot is mounted separately to avoid cross-contamination during the grinding process. The kV should be high (25 kV) for the detection of lead. The probe current should be between 0.5–2 nAmp. Usually the analysis is qualitative since lead, if present, is generally a major component. If lead is found to be at a concentration of approximately 1% a quantitative analysis (WDX) is performed.

The analysis of ammunition components is useful in determining the presence of unusual components, such as high Sn or Ba/Ca/Si indicative of certain brands of ammunition. It can also support findings in GSR or bullet smears. For this application it is recommended to use a long EDX acquisition time (200 seconds) in order to determine the presence of trace levels of antimony in lead (0.5 - 3.5% Sb).

Comparison and Physical Match

Tool Marks: The topographic backscatter detection mode (BSED) is ideal for this application. Carbon coating is recommended if surface contamination is present. The initial observation should be performed at a long working distance (WD) and low magnification to locate gross features. Move to a shorter WD to improve the backscatter signal, and a higher magnification to detect smaller features. The kV and probe current should be kept low for beam sensitive samples and fine surface detail, but can be increased for improved BSED.

The SEM can also be used for comparisons/physical matches of postage stamps, cutting wheel fragments, unusual alloys, rifling marks and firing pin impressions.

Automated Particle Analysis:

Gunshot Residue: The RJLee© Personal SEM (PSEM) is used for GSR since automated analysis was a design consideration when the PSEM was created.

When doing automation analysis, quality assurance must not be compromised. It must be considered in the methodology approach, analytical parameters and performance checks. Parameter sheets should be used for pre-run checks, exhibit continuity and post run comments.

The specimen current should be monitored to confirm instrument stability and to ensure that the analysis was uninterrupted.

The PSEM is also used for automated analysis of cosmetics and soils.

Light Element Analysis:

The analysis of light elements can be useful as supportive evidence for compound identification. The nature of the compound can make the analysis difficult, seen by a noticeable decrease in count rate. This can sometimes be avoided by moving the beam during acquisition. Selection of kV is much more critical in this application. The best detector resolution should be used.

Trace elements:

Because of its lower detection limit and more accurate quantitative analysis, WDX is used for the analysis of trace elements. WDX generally requires a higher probe current, longer acquisition time and good sample conductivity. It is usually used in conjunction with EDX, where EDX identifies major components, and WDX identifies/confirms trace elements.

Food Structure and Functionality Symposium

Immunolocalization of Surface Antigens on *Campylobacter jejuni* using FESEM and a Back-Scatter Electron Detector

DELILAH F. WOOD,† ROBERT MANDRELL, ANNA H. BATES, AND PAULINE C. YU

U.S. Department of Agriculture, Agricultural Research Service, Western Regional Research Center. 800 Buchanan St., Albany, CA, USA

†Formerly published as Delilah W. Irving.

Campylobacter jejuni is one of the most common causes of food poisoning in humans in the US. Poultry are thought to be the main source of the bacteria, however; there is no definitive method for differentiating bacterial species on food surfaces. Most bacteria have surface molecules that are species specific and some of the molecules may be responsible for the adhesion of the bacteria to food surfaces. Monoclonal antibodies (MAbs) can be produced that bind to antigens on these surface molecules, and they facilitate identification of bacterial species and strains in immunoassays and complex environments. When coupled with an appropriate label, fluorescence and scanning electron microscopy (SEM) allow visualization of antibodies bound to antigens on bacteria in complex environments; e.g. *C. jejuni* on food surfaces.

Specific surface antigens on *C. jejuni* have been identified and MAbs that bind to them have been produced. The bacterial surface antigens have been labeled with MAbs and fluorescent anti-mouse secondary antibodies and the bacteria observed by confocal microscopy. Confocal microscopy is an excellent tool; however, the resolution is insufficient to recognize structural details. High-resolution images can be obtained of bacteria using field emission SEM, and, when combined with an appropriate electron-dense label (gold), the binding site of the antibody (therefore, the specific antigen) is located.

Gold particles can be made in various sizes and conjugated to an antibody. Smaller particles allow more precision in the localization of surface molecules. Gold particles were viewed using electron back-scattering techniques. Gold particles are visible using secondary electron detection. However, secondary electrons only give superficial information and bacterial surfaces contain other particles that may be of similar dimensions as the gold particles, therefore the gold particles are not distinct. Back-scattered electrons produce images of increasing brightness as a function of increasing molecular weight. Therefore, the heavier gold particles appear bright against the darker bacterium.

Campylobacter jejuni cells from culture were incubated with anti-*C. jejuni* MAbs, the cells were rinsed, then incubated with 15nm and 30nm gold-conjugated anti-MAbs. The labeled bacteria were fixed overnight at 23%C in 3% glutaraldehyde in phosphate buffered saline (PBS), pH 7.4, and rinsed three times in PBS. The samples were pelleted between each step. The pellets were resuspended and post-fixed in 1% aqueous osmium tetroxide overnight at 4%C and rinsed three times in water (pelleted between each step). The pellets were re-suspended in water and filtered through 0.2 mm Nuclepore filters that had been pretreated in 0.1% poly-L-lysine to increase adherence of the bacteria to the filter. The filters containing bacteria were placed between hard plastic mesh, fastened together to keep the filters flat and maintain orientation of the bacteria and treated as a unit throughout subsequent steps. The mesh unit was dehydrated in ethanol and critical point dried. The filters were removed from the mesh unit and mounted on specimen stubs and sputter coated with gold-palladium. Samples were observed and photographed using both a standard secondary electron detector to obtain high resolution secondary images (Fig 1A), and a YAG (ytrium-aluminum-garnet) back-scatter electron detector to locate the gold particles on bacterial surfaces (Fig 1B).

Spiral and coccoid forms of *C. jejuni* were observed (Fig. 1A), however, the immunogold labeled antibodies were located predominately on the coccoid forms (Fig. 1B). These results indicate either that the MAb-defined antigen was not expressed on the spiral cells, or that the antigen is better exposed on the coccoid form rather than the spiral form. It has not been determined whether the specific antigen identified is associated with adhesion of *C. jejuni* to food surfaces. However, the results indicate that the form of the bacteria affects the surface availability of antigens; which may be important in identifying antigens responsible for the adhesion of *C. jejuni* to food. Most significantly, a method has been identified that will readily characterize the surface-available antigens.

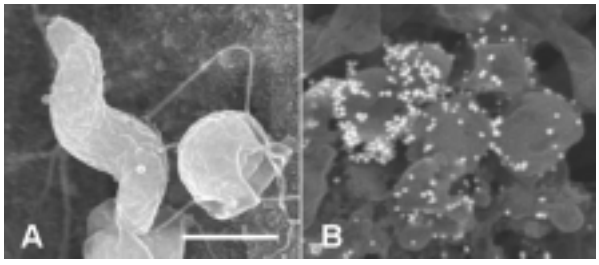

FIG. 1 *Campylobacter jejuni*. A. Secondary electron image showing both the spiral (left) and coccoid (right) forms. B. Back-scatter electron image showing gold label on the coccoid form of the bacterium. Bar = 500nm.

Acknowledgments

The authors wish to thank William Roth (Nissei-Sanyo America) for taking the photographs and Donald Becker and Daniel Becker (Hitachi) for facilitating the use of the equipment.

Particle Distribution in Microscopy Images of Cryo-sectioned Sausages as affected by Fat Content

RAGNI OFSTAD, VIBEKE HØST, ØYVIND LANGSRUD AND ACHIM KOHLER

MATFORSK-Norwegian Food Research Institute, Osloveien, Norway

Introduction

It is previously reported that the type of meat and fat, the levels of moisture and fat, and the comminution process influence the microstructure as well as the sensory quality of finely comminuted meat products[1–3]. The precise quantification of structures will be the first essential step for predictive modelling of sensory properties such as texture and juiciness.

The aim of this work was:

a) To quantify the fat particle distribution pattern in light microscopy images of cryo-sectioned sausages
b) To use multivariate analyses of variance to identify significant differences in the fat distribution pattern among treatments.

Materials and Methods

Nine different pork/fat trim sausages were prepared with three levels of fat (15, 20, 25%) and three levels of chopping (short, medium and long time) in dual trials (day 1 and 2). One sausage from each of the 18 samples was prepared for microscopy, i.e. frozen in liquid nitrogen, cryo-sectioned (10 µm), stained by Nile Red and examined with a fluorescent microscope (129×). A CCD camera (Hitachi KP-D50 colour digital) was used to capture five images from randomly selected regions.

Image processing was performed using Image Pro-Plus 3.0 according to Kohler *et al.*[4] With the area distribution method one gains an array of variables from each image. It is therefore natural to use multivariate methods in order to classify the microscopy images. A new method for multivariate analyses of variance[5] was used to identify significant differences among treatments. This method (Fifty-fifty MANOVA) handles highly correlated responses and it can be used to analyse continuous curves.

Results

Figure 1 shows examples of images taken from the sausages. The pictures give a qualitative impression of differences in fat content and particle distribution. All bright objects were counted and their areas were calculated. Based on these data, a smoothed histogram was obtained for each sample. A logarithmic scale was used on the x-axis (log area). To focus on the information on the images related to the fat particle distribution, and not differences related to the fat content, all the histograms were standardised (area=1). These distributions (curves) were used as responses in Fifty-fifty MANOVA. The difference in area distribution of the fat particles among the three fat levels was clearly significant ($p<0.01$). The effect of chopping time and the day-to-day variation was however not significant.

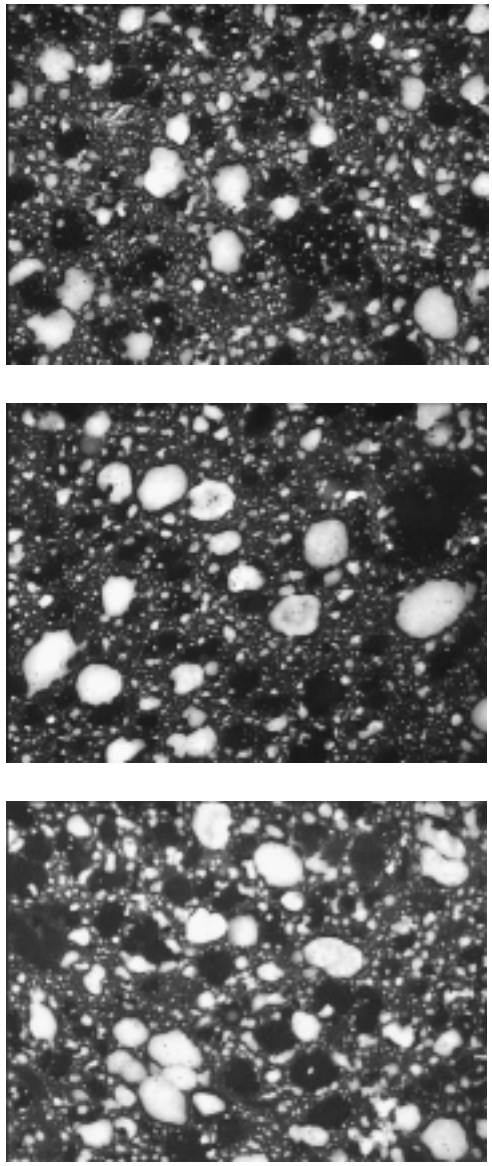

(a)

(b)

(c)

FIG. 1 Images of cryo-sectioned sausages with different fat levels, 15% (a), 20% (b) and 25% (c) fat.

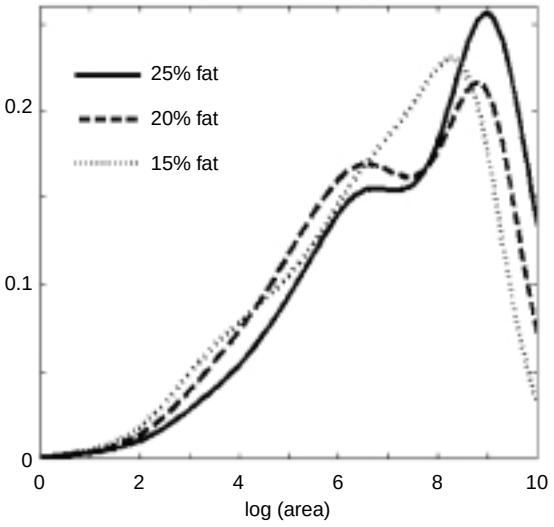

FIG. 2 Average area fraction distribution of the fat filled pores on images of cry-sectioned sausages with three levels of fat.

To illustrate the fat level differences, an average area fraction distribution within each fat level was calculated. The distributions for the different fat levels are shown in Figure 2. At 15 % fat there is one peak, at 20% there are two peaks and at 25% fat content there is one peak and one saddle point, which indicates that there are two peaks overlapping. Thus, in the high-fat batter (20, 25%) the fat is either emulsified to small droplets or remains as bigger droplets and/or agglomerates of droplets restricted by intact cell membranes and/or the protein-matrix. The higher average diameter of the fat droplets in the low fat samples may be due to less restriction of the higher moisture protein matrix embedding them.[1]

Conclusion

1. In the experimental design performed, the fat distribution pattern was only significantly dependent on the fat content.
2. The combination of area distribution method and multivariate statistics seemed possible to use to find differences in structures relevant for quality parameters.

References

Lee CM: Microstructure of meat emulsions in relation to fat stabilisation. Fd Microstructure 4 63–72, 1985.

Koolmees PA, Moerman PC, Zidjderveld MHG: Image analysis of the fat dispersion in a comminuted meat system. Fd Microstructure 8 81–90, 1989.

Colomenero FJ, Barreto G., Mota N, Carballo J: Influence of protein and fat content and cooking temperature on texture and sensory evaluation of bologna sausage. Lebensm.-Wiss. U. Technol. 28 481–487, 1995.

Kohler A, Hoest V, Ofstad R: Image analysis of particle distribution in microscopy images of cryo-sectioned sausages. Submitted, 2000.

Langsrud Ø: Fifty-fifty MANOVA: Multivariate Analysis of Variance for Collinear Responses. In preparation, 2000.

Ultrastructure of Fouled Microfiltration and Ultrafiltration Membranes

YAN JING, BRYONY J. JAMES

Research Center for Surface and Materials Science,
Department of Chemical and Materials Engineering,
The University of Auckland, Auckland, New Zealand

Membrane separation is a technology experiencing rapid growth, particularly in the field of food processing[1]. One of the major factors limiting the economical feasibility of membrane separation technologies is the problem of "fouling." An understanding of the fundamental mechanisms of membrane fouling is essential if the optimum performance of this technique is to be realised.

Surface morphology and internal microstructure of a membrane have a great effect on fouling and separation performance. Unfortunately, because of the nature of proteins and the polymeric membrane, studying the structure of the filtration materials and fouled layer is difficult. This is especially true in the study of the internal membrane structure[2]. In this study the microstructure and ultrastructure of the fouled membrane were examined using a number of techniques.

Scanning Electron Microscopy (SEM), Atomic Force Microscopy (AFM) and X-ray Photoelectron Spectroscopy (XPS) were used to investigate the physical evidence of the formation of a gel layer on the surface of the membrane, the internal fouling within the membrane structure and the effect of pressure on permeate flux and fouling. A new method has been developed to study internal membrane structure using high-resolution FEG-SEM with a low accelerating voltage.

Two Osmonics© membranes were used: a microfiltration membrane (pore size of 3 µm) and an ultrafiltration membrane (molecular weight cutoff 3,500). Filtration of 10% (w/w) skim milk powder was performed on a high-pressure flat sheet with cross-flow configuration. Characteristics of a fouled membrane were studied in terms of transmembrane pressure and filtration time, some results are summarised here.

Surface morphology and internal microstructure of the unused membrane.

SEM and AFM were used in conjunction. The skin layer of the microfiltration membrane showed a finger like substructure and sieve like top layer. The membrane surface had a varied pore size with a maximum size of approximately 0.35 µm. This was larger than the product specification.

The ultrafiltration membrane showed nodules, in various sizes, which spread across the entire surface. A cross section of the membrane revealed a smooth fouling resistant layer at the surface, a nodular layer in the middle and a foam like layer with voids connected to the support layer.

Fouling on the surface of the membrane

A gel layer had formed on the surface of both membranes after filtration. The structure of the surface of the fouled membrane was seen more clearly under AFM than SEM.

Fouling within the membrane structure

XPS analysis showed internal fouling occurred after filtration. It is believed this could be attributed to the interaction between milk proteins and the membrane polymer and protein-protein reaction[3]. SEM cross sections, using a novel sample preparation technique, of the fouled microfiltration membrane presented strong physical evidence to prove this assumption. These clearly showed protein-protein interaction and interaction between protein and the pore walls of the membrane, thus forming agglomerates. This led to pore plugging and narrowing and finally total blockage of the pores.

From the results of this study it may be concluded that:

1. AFM is an appropriate and convenient technique for examining the upper surface of fouled membranes.
2. SEM, using appropriate sample preparation, is the best technique for examining the internal structure of a fouled membrane.

In terms of the filtration parameters affecting fouling it would appear that in ultrafiltration permeate flux increases with pressure, whereas in microfiltration there is a critical pressure above which permeate flux decreases. This is due to the effect of concentration polarization and consolidation of the foulant, which is observed under SEM.

References

1. B. Hallstrom, G. Tragardh and J. L. Nilsson, "Membrane Technology in the Food Industry", Engineering and Food, vol. 3 Advanced Processes, Elsevier Applied Science, London, pp. 194-208
2. K. J. Kim, V. Chen and A. G. Fane, "Characterization of Clean and Fouled Membrane Using Metal Colloids", Journal of Membrane Science, vol. 88, 1994, pp. 93-101.
3. George Belfort, Robert H. Davis, Andrew L. Zydney, "The Behavior of Suspensions and Macromolecular Solutions in Crossflow Microfiltration", Journal of Membrane Science, vol. 96, 1994, pp1-58.

The Microstructure of Corn Tortillas During Baking

CASSANDRA MCDONOUGH, ELLY SUHENDRO, AND LLOYD W. ROONEY

Cereal Quality Lab, Soil and Crop Sciences, Texas A&M University, College Station, TX, USA

The basic structural changes that corn tortillas undergo during baking were documented with an Electroscan environmental scanning electron microscope. Samples were collected after the tortillas passed across each of the three tiers in the oven, placed in air-tight plastic bags and stored at –4°C until viewing. Corn is traditionally cooked in alkali to soften the kernel, partially gelatinize the starch, denature the protein, and remove the pericarp; it is then ground into masa. Masa consists of small pieces of germ, pericarp, aleurone and endosperm, and free starch granules, cell fragments, and dissolved or dispersed solids and lipids in water. The masa is held together by a 'glue' that is composed of leached amylose and amylopectin from the starch, denatured protein and lipids. The masa is die-cut into a disk shape and baked in a 3-tier oven, with temperatures of tiers 1, 2, and 3 ranging from 280–470°C. The texture of the unbaked tortilla disks was very dense, with no air cells. Intact starch granules and small endosperm pieces were embedded in the starchy matrix of the masa. When the unbaked tortilla disk entered the oven, there was no expansion until the disk was heated. The heat flashed the moisture off the surface of the tortilla, so the starch on the surface remained ungelatinized. After passing through the 1st tier of the oven, small channels formed where the steam began to escape the interior, but the microstructure of the tortilla was not dramatically different from the masa disk. On the 2nd tier, the starch in the interior was further gelatinized, but that on both surfaces retained birefringence. Some expansion continued and one or more central air voids formed as the steam continued trying to leave the disk. On the 3rd tier, the tortilla flipped over once again so the first side was again exposed to heat. By this time, the starchy matrix was dehydrated enough to start to set its crumb structure. The tortilla crumb was characterized by large central voids due to expansion of the gases during heating (visually observed as 'puffing' like a balloon), and small air holes/channels that formed just beneath either surface, a few of which broke through to the surface. Even though the center of the tortilla puffed in the oven, the outer edges of the disk remain sealed. In the crumb, cell walls were further degraded until they were no longer visible, there was further loss of starch crystallinity to the point where roughly 60% of the starch was fully or partially gelatinized, and the protein was further degraded. As soon as the tortillas left the oven and fell to the cooling conveyer, they collapsed quickly as the heated gases cooled to near ambient temperature. The inner surfaces may fuse together if they are still moist enough at this point, though some will remain separated, which impacts the textural quality of the tortilla.

Use of Confocal Microscopy and the Green Fluorescent Protein in Ecological Studies of *Salmonella* on Plant Surfaces

M.T. BRANDL , R.E. MANDRELL

Food Safety and Health, USDA/ARS, WRRC, Albany, California, USA

In recent years , human infection with virulent strains of *Salmonella enterica* (*S.e.*) linked to contamination of food has been the source of great concern. Although generally associated with consumption of meat products, outbreaks of salmonellosis are increasingly linked to contaminated fruits and vegetables in the United States as well as in many foreign countries (3). In particular, large international outbreaks of *Salmonella* infections have originated from sprouts grown from contaminated seeds (4) and many outbreaks have been linked to cilantro, parsley and melon in the United States (2). The interaction of *Salmonella* with its vertebrate hosts has been the object of intense studies. In contrast, our understanding of how this enteric pathogen colonizes plant surfaces is lacking. We have transformed a strain of *S.e.* serovar Thompson that was linked to an epidemic from cilantro, with a gene encoding the green fluorescent protein (GFP) from *Aequoria victoria* (1). This GFP-labeled strain (*S.e.* Thompson pWM1007) was used for in situ investigation of colonization of cilantro plants in conjunction with confocal microscopy.

Young cilantro plants were inoculated with a suspension of *S.e*. Thompson pWM1007 at a final concentration of $1x10^4$ cells per g leaf tissue. The plants were incubated at room temperature in a dew chamber immediately following inoculation. Inoculated cilantro leaves were sampled at regular time intervals after inoculation, and bacterial populations on the leaves were observed directly with 40x and 63x objective lenses on a confocal laser scanning microscope (CLSM) (TCS4D, Leica Lasertechnik, Germany) equipped with argon, krypton, and He/Ne lasers. GFP/fluorescein and LP590 filters were used to simultaneously monitor the fluorescent signals from the *Salmonella* cells and the leaf, respectively.

Cilantro leaves sampled immediately after inoculation harbored single cells of GFP-labeled *S.e.* Thompson distributed at low density on the leaf surface. Major changes in colonization were observed as early as 2 days postinoculation. The *Salmonella* population had reached high densities in the vein areas of the leaf, and distinct microcolonies were present. Leaf surface areas between the veins also hosted *Salmonella* cells, but at much lower density. Transversal (xz) scans revealed that the cells were located on the cuticle of healthy leaf tissue. However, high numbers of *Salmonella* cells were observed within the cuticle and epidermal cells of cilantro leaves where lesions were present. Examination of healthy senescent leaves, 9 days postinoculation, showed that *Salmonella* had reached very high populations on the veins and their vicinity.

We have investigated the spatial and temporal distribution of *Salmonella* on the leaf surface of cilantro. Our study revealed that *Salmonella* had the ability to colonize the cilantro phyllosphere and that it achieved high populations on leaves in the vein area, in lesions, and on senescent tissue. This study was facilitated by the use of GFP as an intrinsic fluorochrome which circumvents the disruptive sample preparation associated with other labeling methods, and the use of CLSM which prevents out of focus fluorescence from contaminating the focal plane image.

References

1. Chalfie M, Tu Y, Euskirchen G, Ward WW, Prasher DC: Green fluorescent protein as a marker for gene expression. *Science* 263, 802-805 (1994)
2. Farrar J. Personal Communication
3. Hedberg CW, MacDonald KL and Osterholm MT: Changing epidemiology of food-borne disease: a Minnesota perspective. *Clin. Infect. Dis.* 18, 671-682 (1994)
4. Taormina PJ,Beuchat LR, Sleutsker L : Infections associated with eating seed sprouts: an international concern. *Emerg. Infect. Dis*. 5 (5),1-6 (1999)

Ultrastructural and Textural Changes in Fresh and Processed Apricot (*Prunus Armeniaca L.*)

ETELKA KOVÁCS,* Z. KRISTÓF† AND P. SASS‡

*Central Food Research Institute, Dept. Microbiology & Postharvest Physiology, Budapest, Hungary; †Eötvös Loránd University, Institute of Plant Anatomy, Budapest, Hungary; ‡Szent István University, Institute of Postharvest Technology, Budapest, Hungary

Two apricot cultivars (cv Magyar, cv Bergeron) were harvested in different time, then stored at 4–6°C, 90 % relative humidity for 30 days. A part of fruits (as a function of harvest and storage time) were deep freezed and lyophilized, then investigated by SEM and TEM. Texture of fresh fruits was measured by penetrometer on different points of each fruit. Data were analyzed by principal component analysis. The cell wall structure and decomposition of fresh fruits were studied by chemical analysis. The activity of β-galactosidase and polygalacturonase of different samples were determined as a function of harvest, stored time.

The firmness of fruits cv Magyar kajszi were significantly different according to the harvest. During storage the firmness values changed a little. Firmness of cv Bergeron did not differ as a function of harvest and slowly changed as a function of storage time.

The total pectin content decreased in both investigated cultivars. The activity of enzymes was different as a function of harvest, storage, and cultivars.

The ultrastucture was different in cultivars, harvest, and storage.

A Microscopic Investigation of Fruit Development in *Schinus molle*

HOWARD J. ARNOTT AND DELILAH F. WOOD*†

The University of Texas at Arlington, Arlington, Texas; *The United States Department of Agriculture (USDA) Laboratory, Albany, California, USA

†Formerly published as Delilah W. Irving.

The California Pepper Tree, *Schinus molle* L., a large evergreen tree which produces colorful rose-pink berries in the fall is a popular cultivar in California. The fruits of *S. molle* are similar to those of *S. terebinthifoliu*s, the species which produces the pink peppercorns of commerce and, like the latter, has also been sold as a spice. The flowers and fruits used in this research were collected in Northern California, and shipped overnight to Texas for fixation and processing. Hand and cryostat sections of fresh materials and paraffin sections were examined by light microscopy. Some flowers and fruits were fixed in formalin-acetic acid-alcohol, but others were fixed in glutaraldehyde and postfixed in osmium tetroxide. All SEM specimens were critical point dried, sputter coated with gold/palladium, mounted on aluminum stubs and examined. Digital images were produced directly from both light and electron microscopes. For comparison, rehydrated commercial fruits of *S. terebinthifoliu*s were also studied.

The flowers of *S. molle* are cream in color and have a floral pattern consistent with other members of the Anacardiaceae. The flowers are functionally unisexual and found on separate trees. Unisexuality comes about through the malformation of either the stamens or the ovary in the respective otherwise perfect flowers. In female flowers the ovary surface is smooth and glossy, unlike that of the aborting ovary in male flowers. The ovary is initially "bowling pin" shaped, but through development changes into a sphere-shape. The bulbous red-purple stigmas remain after pollination but do not grow. As the ovary grows the surface remains smooth but its color changes to green and then to a pink/purple.

Early in development of the *S. molle* flowers and fruits, a system of resin canals begins to develop. This system consists of a series of interconnected branching spaces which enter from the peduncle and whose derivatives enter the receptacle and then pass into the developing fruit wall. This system is represented in the mature fruit by a series of large resin canals (Fig 1a) encircling the entire fruit and occupying a substantial volume of the fruit wall. The resin canals are filled with a watery material when fresh (Fig 1b). A similar system of resin canals is found in the mature fruits of *S. terebinthifolius*. The cells involved in resin canal formation are derived from normal pericarp wall cells, they are smaller, and more tightly packed. The cells immediately surrounding the canals are often crushed and distinct from the normal pericarp cells (Fig 1b).

In the fruits of the California Pepper trees which were examined, pollination occurs and the embryo undergoes early development but then appears to abort. Unlike the embryo, the fruit and seed continue to develop increasing "normally" in size and changing in color. Both the seed coat and fruit develop concurrently, maintaining their size relationships as ontogeny progresses. In the seed, however, a very large central cavity develops in the position where the embryo should be found. This was determined by comparison with mature fruits of *S. terebinthifoliu*s (from a commercial source) where embryos were observed with two cotyledons and some endosperm entirely filling the concordant space that is represented by a cavity in *S. molle*. No mature embryos were observed in hundreds of "mature" fruits examined. The abortion of embryos is an effective means of controlling plant distribution. Many exotic plants have been introduced as ornamentals and have become problems due to their naturalization in an area. *Schinus terebinthifolius*, for example, is a serious problem in southern Florida where birds have aided in its dispersal[1,2].

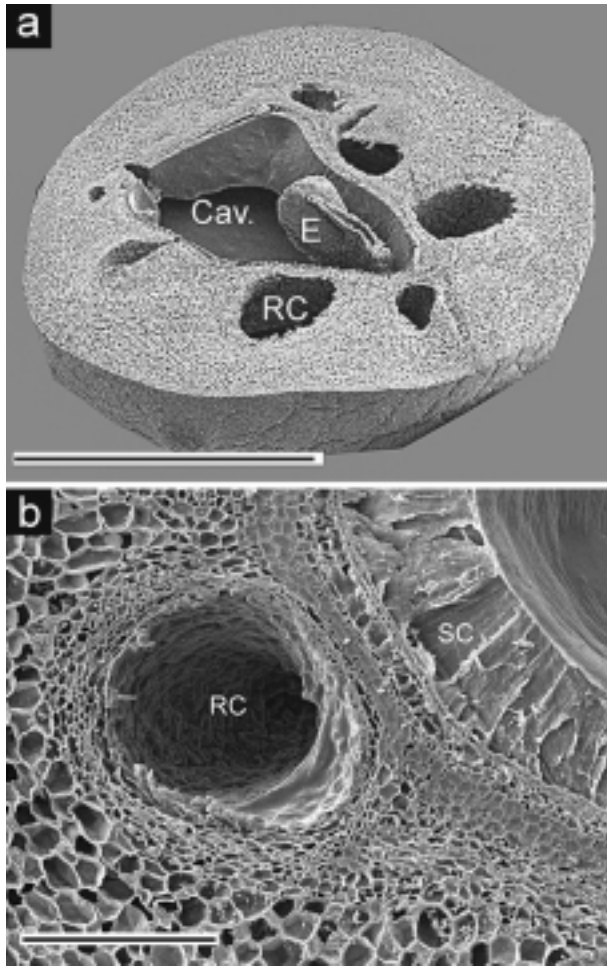

FIG. 1 Scanning electron micrographs showing cross sections of *Schinus molle*. a. The whole fruit showing a series of resin canals (RC), the aborted embryo (E) and the embryo cavity (Cav). Bar = 2mm. b. The fruit wall showing a resin canal (RC) and the seed coat (SC). Bar = 200 mm

References

1. Panetta FD, McKee J:Recruitment of the invasive ornamental, *Schinus terebinthifolius*, is dependent upon frugivores. *Aust J Ecol* 22, 432-438 (1997)
2. Jones DT, Doren RF: The distribution, biology and control of *Schinus terebinthifolius* in southern Florida, with special reference to everglades national park. In *Plant Invasions: Studies from North America and Europe*, pp. 81-93, (Eds. Brock JH, Wade M, Pysek P, Green D, Backhuys Publishers, Leiden, The Netherlands (1997)

Application of Composite Coatings to Prolong Storage Life of Refrigerated Strawberries

M.A. GARCÍA,* M.N. MARTINO*†, AND N.E. ZARITZKY*†,

*Centro de Investigación y Desarrollo en Criotecnología de Alimentos (CIDCA). CONICET. Fac. de Cs. Exactas; †Dto de Ing. Química. Fac. de Ingeniería. UNLP, 47 y 116, (1900) La Plata, Argentina

Introduction

Semi-permeable coatings can be used to extend storage life of fruits due to their barrier properties[1]. The analysis of the effect of each component of the coating is very important to develop formulations with specific purposes. Starch, cellulose derivatives or proteins may give a suitable cohesive and continuous matrix. These hydrophilic compounds are efficient barriers against gases and lipids but are poor barriers against moisture. Plasticizers are included to enhance flexibility and lipids to reduce moisture loss[1,2]. Antimicrobial and antioxidant agents are also added to coating formulations. Thus, composite films and coatings can be formulated to combine the advantages of the different components. The objective of this work was to analyze the effect of formulation on the performance of starch-based coatings applied on fruits with a short storage life.

Materials and Methods

Suspensions of 20g/L corn starch (Molinos Río de la Plata, Argentina) or a high amylose corn starch (Amylomaize VII, Amaizo, USA) were gelatinized with NaOH [3]. To compare the effect of each component 20g/L glycerol or sorbitol as plasticizers (Merck, USA), 2g/L sunflower oil (AGD, Argentina), 0.2g/L potassium sorbate and citric acid to reach pH 4, were added in different formulations. Emulsions were homogenized at 7800 rpm and inmediately used to obtain either coatings or films. Strawberries (*Fragaria ×ananassa*, cv Selva), at commercial ripening stage (75% redness color), grown in greenhouses of a local farm were harvested and immediately treated. Coating was applied by dipping the strawberries in the formulations [3]. Uncoated (control) and coated strawberry samples were stored at 0°C and 84.8% relative humidity. The same fruits were weighed at the beginning of the experiment and during storage and weight loss was expressed as percentage loss of initial weight. Colorimetric measurements were carried out with a Minolta colorimeter CR 300 Series (Japan); Hunter scale was used recording lightness (L) and chromaticity parameters a and b. Petrifilm^{TM} plates (3M, USA) were used to count aerobic mesophilic, psychrotrophic, molds and yeasts and coliforms microorganisms in coated strawberries. SEM of the films was performed with a JEOL JSMP 100 (Japan) electron microscope. Modifications of the crystalline structure of films stored at 20°C and 63.8% relative humidity were evaluated by DSC, in a Polymer Laboratories DSC (Rheometric Scientific, Surrey, UK) working under a PL-V5.41 software, and by X-ray diffraction, in a diffractometer Phillips PW 1390 (The Netherlands) using Ka Cu radiation (γ = 1.5418Å) [4]. Water vapor permeabilities (WVP) of different coating formulations were determined using cylindrical carrot samples as described in a previous work, [5]. CO_2 and O_2 permeabilities of films were assessed by the accumulation method in an especially designed stainless steel cell [4].

Results and Discussion

Quality attributes of refrigerated coated strawberries: All plasticized coatings reduced weight loss compared to the control (Fig. 1a). Strawberries with amylomaize coatings showed significantly ($P<0.05$) lower weight loss than those with corn ones. Weight loss of fruits coated with formulations without plasticizer were similar to that of control fruits due to pores and cracks formed in the coatings. Sorbitol coatings led to significantly lower fruit weight loss than glycerol for both corn and amylomaize coatings. The presence of lipid phase significantly decreased ($P<0.05$) weight loss of fruits (Fig. 1a), what was allowed to maintain high quality fruit for long storage times at 0°C. This result was attributed to the reduction in water vapor permeability of the coatings; the effect of lipids was independent of starch and plasticizer types.

The effect of coatings on surface color of strawberries was also analyzed because this quality attribute may determine consumer acceptability of the fruit. Both plasticizers significantly ($P<0.05$) delayed surface color development, showing smaller lightness modifications (ΔL) with time. Formulations containing glycerol gave better surface color results compared to sorbitol ones. Lipid addition did not modify significantly ($P<0.05$) surface color results regardless of the plasticizer used in the formulation (Fig. 1b). ANOVA showed a significant effect ($P<0.05$) of coating in decreasing microbial counts. The presence of 0.2g/L potassium sorbate in the coatings combined with critic acid provided a local high and effective concentration of the preservative because coatings act as surface retention agents.

Barrier properties and film microstructure: plasticizer was necessary for film integrity to avoid pores and cracks

observed by SEM. Amylomaize films with higher amylose content showed higher crystallinity (measured by DSC and X-ray diffraction) and lower permeabilities than corn starch films. Gas permeability is strongly related to the crystallinity of the polymeric chains [5]. Plasticized starch-based films and coatings showed higher permeability to CO_2 than to O_2. The delay in color change (Fig. 1b) and in the modification of physiological parameters such as acidity, anthocyanin and sugars [3] were attributed to the selective gas permeability of the coatings. The addition of lipids decreased water vapor permeability due to the hydrophobicity; this effect could explain the higher performance in decreasing fruit weight loss of coatings with lipids. Thus, composite starch-based coatings extended storage life of strawberries, decreasing water loss and improving fruit quality.

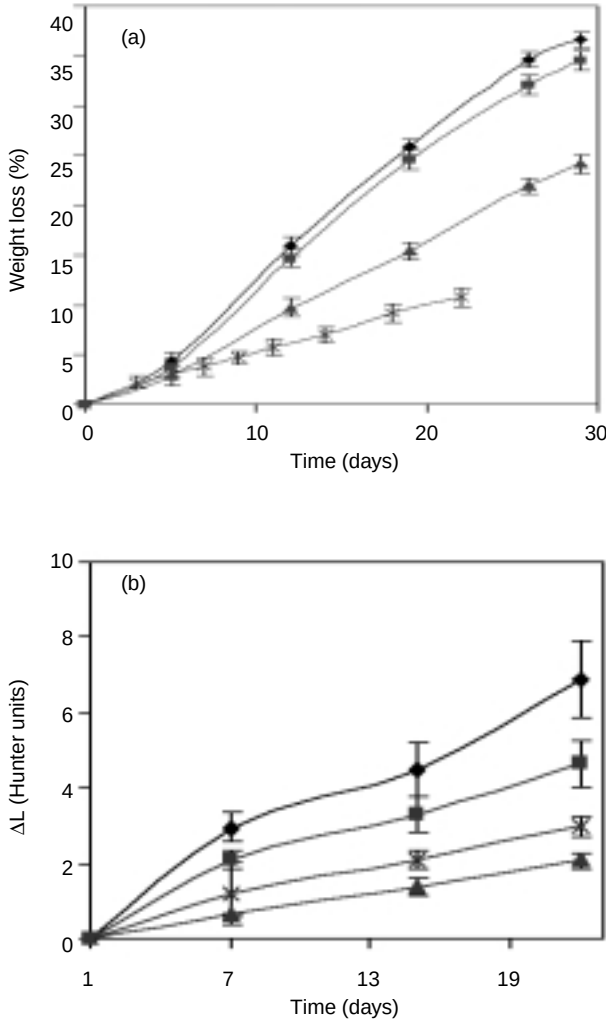

Fig. 1 Coating formulation effect on a) weight loss and b) lightness differences during storage at 0°C of strawberries. Control samples, without coating (◆) and fruits coated with amylomaize coatings: without plasticizers (■), with 20g/L sorbitol (▲) and with 20g/L sorbitol and 2g/L sunflower oil (×). Bars indicate standard errors.

References

1. Baldwin EA, Nisperos MO, Hagenmaier RD, Baker RA: Use of lipids in coatings for food products. Food Technol. 51 (6), 56-62 (1997).
2. Krochta, J.M. and De Mulder-Johnston, C. 1997. "Edible and biodegradable polymer films: challenges and opportunities." Food Technol. 51(2): 61-77.
3. García, M.A., Martino, M.N. and Zaritzky, N.E. 1998. "Plasticizer effect on starch-based coatings applied to strawberries (*Fragaria × ananassa*)." J. Agric. Food Chem. 46: 3758–3767.
4. García, M.A., Martino, M.N. and Zaritzky, N.E. 1999. "Edible starch films and coatings characterization: SEM, water vapor and gas permeabilities." J. Scanning Microscopies. 21 (5): 348–353.
5. Mc Hugh, T.H. and Krochta, J.M. 1994. "Sorbitol- vs glycerol-plasticized whey protein edible films: integrated oxygen permeability and tensile property evaluation." J Agric. Food Chem. 42 (4): 841–845.

Effects of Ozone on the Surface of Loblolly Pine (*Pinus taeda*) Needles

ZHU H. NING AND KAMRAN K. ABDOLLAHI

Southern University, Urban Forestry Program, Division of Agricultural Sciences, College of Agricultural, Family and Consumer Sciences, Baton Rouge, Louisiana, USA

There is evidence of ozone effects on plant anatomy. Evans and Miller[1] studied ozone damage to ponderosa pine and reported in cases of severe injury, the cell contents, including the chloroplasts, aggregated into one or more dark masses in the middle of the cell or near the cell wall. Finally the cell walls collapsed. Stewart *et al.*[2] found that, along with other stresses, ozone caused hypertrophy of the epithelial tissue of the resin canals, with granulation of transfusion and mesophyll parenchyma. They indicated that collapse of the cell wall best characterized necrosis caused by ozone. Cytological changes in needles of pitch pine seedlings stressed by ozone were determined by McQuattie and Schier[3]. The most pronounced changes occurred in the outer mesophyll. At a low level of ozone, the cytoplasm became more densely stained. Accumulation of dense materials appeared at intermediate treatment concentrations, and at high concentration localized cell collapse and deterioration became evident.

How ozone affects the leaf surface protective layer, such as cuticle, a wax-containing layer or layers covering the outer walls of the epidermal cells to prevent water loss and fungal invasion, is still unknown. The intent of this study is to provide some answers regarding this question.

Loblolly pine, a common urban shade tree used over a wide geographical range in the South was chosen as the experimental plant. Four feet high saplings were used because this is the most frequent size used in planting or transplanting urban tree species. The experiments on ozone exposure were conducted using a system for ozone exposure and measurement of gas exchange. The use of expo-

sure and measurements in a controlled environment are of importance when studying the mechanisms of pollutant injury. It avoids the influence of other biotic and abiotic factors in the field affecting the occurrence and manifestation of damage. Experiments were conducted in a completely randomized design of ozone treatments, with the experimental units being the chambers (cuvettes) for ozone exposure. Two treatments were used for ozone exposure and they are urban ambient ozone (concentration at 0.08 ppm), and 2× urban ambient ozone (concentration at 0.16 ppm). Each treatment was replicated three times. Exposure duration was seven hours per day.

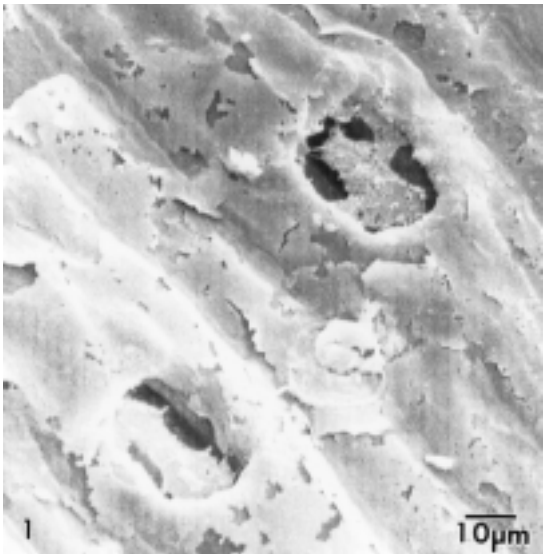

Fig. 1. Needle surface of a loblolly pine exposed to urban ambient ozone concentration. The surface is naturally heavily cutinized to prevent water loss. The cuticle (wax deposit) extends across the openings of the sunken stomata.

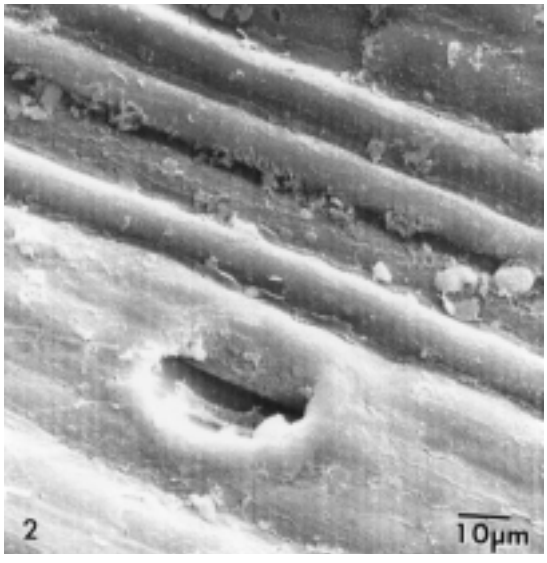

Fig. 2. Needle surface of a loblolly pine exposed to 2x urban ambient ozone concentration. Cuticle on the surface of the pine needle was partially destroyed. The amount of wax deposit over the stomata was significantly reduced.

Light and electron microscopy were employed to examine the effects of ozone on anatomy of the pine needles. Needle samples were collected daily from the upper portion of the experimental plants, and examined quickly for visible injury. Samples for microscopic examination were fixed and processed promptly. They were cut to 1mm and fixed overnight at 4°C in 4% glutaraldehyde buffered with 0.07M cacodylate at pH of 7.2-7.4. After washing thoroughly in the buffer, samples were dehydrated in a graded ethanol series and dried in a PELCO CPD2 Critical Point Dryer, and then coated in a Hummer V Sputter Coater. A Cambridge 150 scanning electron microscope was used for examination.

SEM observation revealed leaf surface damage induced by ozone exposure. Normally, the surface of a pine needle is heavily cutinized to prevent water loss. The cuticle extends across the openings of the sunken stomata (Fig.1). When the loblolly pine was exposed to ozone, cuticle on the surface of the needles was partially destroyed. The amount of wax deposit over the stomata was significantly reduced (Fig. 2). The major components of the cuticle are lipids. There is sufficient observational evidence indicating dissociation of lipids caused by ozone exposure. Subsequently, the cuticle layer was partially destroyed. Such damages to the needle surface cuticle would result in increased transpiration (water loss) and reduced drought tolerance. Since water plays an important role in photosynthesis, damage to the needle surface cuticle, indirectly, would affect photosynthetic capacity. However, to substantiate these findings, additional research and analysis need to be performed.

References

1. Evans, L. S. and P. R. Miller, 1973. Ozone damage to ponderosa pine: a histological and histochemical appraisal. American Journal of Botany, 59:297–304
2. McQuattie, C. J. and G. A. Schier, 1993. Effects of ozone and aluminum on pitch pine (Pinus rigida) seedlings: needle ultrastructure. Canadian Journal of Botany. 43:419–427
3. Stewart, D., Treshaw, M. and F.M. Harner, 1973. Pathological anatomy of conifer needle necrosis. Canadian Journal of Botany. 51:1213–1219

Graphic Arts Aspects of Microscopy

Introduction of Color in Grayscale Scientific Imaging

ARON BLAYVAS

Department of Anthropology, Hunter College, CUNY, New York, NY, USA

Colorizing of an image in grayscale imaging is usually referred to as pseudo- color. Since a grayscale image provides information only about luminosity, the addition of color information is normally considered as arbitrary. In digital imaging the image exists as a spatial data structure — SDS — where each specific value of luminosity refers to a point specified by a pair of coordinates in a 2-dimensional space, although it isn't necessary to store the coordinates explicitly. In a gray scale image only one single value is assigned to each pair of coordinates. A full color image needs three values rather then one, and no one of the three should be a derivative of any of the two others. In mathematical terms, the cortege at each point should consist of independent values.

With the use of multiple filters or instruments to image the same object for creation of a same-field-of-view image, it becomes possible to build a full color image where color isn't arbitrary. If at least two images of the same object are created independently, the third image can be calculated from two independent originals visualizing the absolute or relative difference between them. Assigned colors are not arbitrary, but are unique to the specimen and the mode of imaging. However, the interpretation of the resulting color image cannot rely on life experience, as is the case in optical imaging, since the image depends on the applied method.

A color image consists of three color components (planes) (although for some color spaces such as CMYK there are 4 color planes). The assignment of a gray image to a color plane is not objectively predefined. There are some basic concepts that should be considered:

1. Any color can be represented in terms of hue, saturation, and luminosity. There are several color models, or spaces, incorporating this approach; e.g. HLS. Hue (H) represents the azimuth in the color wheel (in degrees — from 0° to 359°) or some other value defining a point in the color spectrum. Luminosity (L, or B in other models) shows how bright the gray equivalent of the color image will be. Saturation (S) shows how much gray (in % — from 0 to 100) is blended with the pure color. In pseudo color schemes different hues are used for different classes, while inside a class the luminosity or saturation are modified.
2. Psychologically it is easier to read a color scheme if the significance of classes follows the transition from cool colors to warm. Cools are associated with blue, and warm tones with red. However, this is just a direction, not an objective assignment.
3. There is a highly subjective, but useful concept of "outstanding" and "backstepping" colors. Two adjacent bright colors seem not to be in the same plane. One of them is an "outstanding" color and it seems to be closer to the viewer — for instance, red or yellow on dark blue background, while a light blue on black background makes an impression of a hole. These effects may be useful in diagramming, mapping, and adding graphic information to an image. However, for creating color images from gray originals, in general, it should be avoided.

Creating a full color image from two gray images requires imaging software and programming in order to create the third conform gray image for the absent color plane. Such a utility is created in Visual basic 6.0 based on the Component Object Model with a component from LEADTOOLS (v. 10.0 LEAD Technology, Inc). Although it could be done with a proprietary algorithm computing values for each pixel individually, this approach results in a very slow performance, because everything is computed at a high level with a number of function calls equal to the number of pixels times the number of loops. Using supplied internal image processing functions, the process is faster by about 100 times, so that processing of one pair of grayscale images and creation of color image takes 1 second average for images up to 2 MB on a 450 MHz computer. The color assignment is as follows: image created on a light microscope with a polarizing filter is used for the blue plane, the other from electron scanning microscope — for the green plane, and the synthesized differential image — to the red plane. Color image synthesis from gray scale same-field-of-view images shows significant potential in scientific imaging, because it is essentially objective, not arbitrary, as conventional pseudo color schemes.

Beauty is in the "Eye" of the Beholder: Morphology and Color in Analytical Microscopy

HAVIVA M. GOLDMAN, TIMOTHY G. BROMAGE, ARON BLAYVAS, AND C. DAVID THOMAS*

Department of Anthropology, Hunter College, CUNY, New York, NY, USA; *The University of Melbourne, School of Dental Science, Department of Oral Anatomy, Melbourne, Australia

Due to increased sophistication of available computer hardware and software, PC based image analysis has become an increasingly integral component of microscopy research. Automated image analytical procedures afforded by such advances greatly increase our ability to analyze large numbers of specimens at greater resolution than previously possible. Below, we describe image analytical procedures that utilize color rendering and graphic overlays to

improve the visualization and quantification of data related to our research interests in bone histology. We emphasize the use of color because the human eye-brain complex is much more adept at morphological discrimination in color than in levels of grey.

Our histological sections have been prepared for use in both scanning electron (SEM) and light microscopes (LM)[1]. The SEM and LM are both equipped with motorized stages and output to an image analysis software program. We can therefore obtain same-field of view digital grey-scale, tiled images across the entire bone cortex in both microscopy modes.

Resulting LM and SEM images are each montaged into single images using a procedure we developed employing Microsoft Visual Basic 6.0 programming combined with LEADTOOLS imaging functions (v. 10, LEAD Technologies, Inc., Charlotte, NC). A compromise in image size and quality is reached such that global biological phenomena can be observed at a higher resolution than possible with a macro-lens, while the image is still manageable in size.

Once images are montaged, we apply a variety of imaging procedures to produce both visual and quantitative results. In our case, we are interested in producing data concerning two material properties of bone: preferred collagen fiber orientation and relative mineralization. Our imaging procedures allow us to examine each of these properties individually, as well as to explore the relationship between the two properties. Using a broad range of imaging software, we are able to customize our imaging needs for individual biological problems.

In order to visualize our data across montages of entire bone cross-sections, we use color look-up-tables (LUTs). The human psycho-visual system is designed such as to bring image focus onto the central portion of the retina, which consists of cones to the exclusion of rods (which are more peripherally located). Morphological details are more acutely visualized by cones insofar as each cone is associated with one optic nerve fiber, but not so well discriminated by rods which are required to combine their inputs from numerous cells into one fiber[2]. Cones are also responsible for generating visual signals we interpret as color, versus grey level visualization by the rod retina. Therefore, humans are well adapted to the color visualization of fine detail in contrast to the appreciation of the same images rendered in grey levels.

The choice of LUTs used in the present study of bone is based on those described in Boyde & Riggs[3] created using features of Adobe Photoshop 5.0. Here, 256 grey-level data is converted into eight or sixteen discrete colors by binning specific ranges of grey as represented by a single color. Our choice of LUT follows a thermal scale, such that dark greys are represented by cool colors (blues and greens), while lighter greys are represented by progressively warmer colors (oranges and reds). Such a thermal scale is useful in the case of mineralization and collagen fiber orientation, where brightness in the grey image correlates directly to the degree of mineralization and orientation, respectively. These colorized bins are easily converted in quantifiable data by calculating the quantity of pixels occupied by each bin.

We have also developed an Optimas macro that divides the bone cross-section into sixteen biologically meaningful sectors within which data are calculated[4]. Segmentation lines are retained as a binary overlay on the montage. As with our LUT procedure, the combination of quantitative and visualization procedures in the segmentation program enhances our understanding of image data.

Finally, we have developed imaging procedures that integrate information from multiple microscopy sources, producing quantifiable data concerning the relationship between histological variables in a visually interpretable way. We have developed two approaches. The first is a statistical method that outputs a continuous RGB color scheme, allowing for robust quantitative comparisons at the pixel level. We also employ a routine that utilizes color LUTs. Both of these methods allow for enhanced visualization of correspondences between the two image sources due to their use of contrasting colors. The two image analytical procedures can be used alone or in combination, depending on the needs of a particular application.

Acknowledgments

This research was made possible by NSF (SBR-9727689) and L.S.B. Leakey Foundation grants to HMG and equipment grants provided by NASA and NSF (SBR-9512373) and Graduate Research Initiative to the Analytical Microscopy and Imaging Center in Anthropology, Hunter College.

References

1. Goldman HM, Kindsvater J, Bromage TG: Correlative light and backscattered electron microscopy of bone - Part I: specimen preparation methods. Scanning 21, 40-43 (1999).
2. Tansley, K: Vision in Vertebrates. Chapman and Hall: London, Pp. 14-26 (1965).
3. Boyde A, Riggs CM: The quantitative study of the orientation of collagen in compact bone slices. Bone 11, 35-39 (1990).
4. Feik SA, Thomas CDL, Bruns R, Clement JG: Regional variations in cross-sectional geometry n the femoral mid-shaft: sex and age differences. Am J Phys Anthropol (in press).

Microscopy Techniques and their Applications

Data Tailings: Recapture of Derivative Microscopy Images Into The Digital Domain

ROBERT V. BLYSTONE AND ERICA GUTIERREZ

Department of Biology, Trinity University, San Antonio, Texas

A tailing is defined as the residue left over from refining a raw material such as an ore. The older scientific literature is replete with derivative microscope images which today are considered as residues of bygone research. Camera lucida drawings and paraffin models were often used to represent objects seen in the microscope; however, by today's standards these published images are just data tailings, residues cast aside by new mining techniques. We have devised methodologies by which these image data tailings can be recaptured into the digital domain and yield new interpretations.

Two subjects are illustrative of the methodologies: embryo development and compact bone organization. Numerous camera lucida drawings of chick embryo development were executed and published in the first decades of the twentieth century. We will demonstrate how twelve camera lucida frames of chick heart development can be converted into a 450 frame movie animating development from 20 to 100 hours. A two-dimensional photograph of a published paraffin model of bone from mid century was converted into a rotatable three-dimensional model within the computer. Once in the digital domain, these older data sets take on new relevance and can suggest new approaches to analysis.

The camera lucida animation results suggested taking stained chick embryo whole mounts of different ages and creating developmental animations. The three-dimensional bone morphology reconstructions suggested new ways of representing optical slices of compact bone sections. The implementation of these methods has high instructional value in the undergraduate classroom and at the same time reveals new interpretations of developmental movements and of anatomical associations. Software involved in the work includes NIH-Image, Adobe Photoshop, Gryphon Morph, and SurfDriver. The revisiting of older published microscopy images by newer computational means offers much promise.

Sponsored support: NSF USE 95-945805

Ordered Chaos: Management of a Multi-user Facility

VICTORIA E. CENTONZE

Dept. of Cellular and Structural Biology, University of Texas Health Science Center at San Antonio, San Antonio, TX

The successful multi-user facility must respond to the needs of its client base on various levels to ensure broad availability of the resident technology. Accessibility is in all cases the major component.

Recently the Department of Cellular and Structural Biology at UTHSCSA has established a digital optical imaging facility as a core resource for investigators both on the UTHSCSA campus and the surrounding region. The facility contains several multi-parameter microscopes equipped with digital acquisition, capable of wide-field epi-fluorescence imaging, multiple real-time ion measurements, and measurements of cellular constituent interactions using fluorescence resonance energy transfer. The Optical Imaging Facility also has a multi-channel confocal laser scanning microscope and a multiphoton excitation imaging system. These optical sectioning imaging systems provide improved axial resolution over wide-field fluorescence microscopes, thus enabling the collection of fluorescent signal from a single focal plane without interference from signal emanating from over- or under-lying material.

Since our client base is varied it is essential to create a welcoming environment where the barriers to use of the instrumentation are minimized. We offer instruction to clients tailored to their individual needs in order that they may apply the technology to is fullest potential in their research program. Clients proficient in the use of the equipment are allowed 24-hour access to the instrumentation on a first-come basis for both acquisition and processing of data.

Each of our acquisition systems collects either 12- or 14-bit depth images. These digital data may be analyzed and processed to final images on-site. Alternatively, the data may be converted to 8-bit depth data and ported to image processing and analysis software commonly available on personal computers. Conversion to formats acceptable for both PC and Mac operating systems is encouraged.

Data may be distributed to other sites on disk (Zip, Jazz or CD), via a local area network, or through a dedicated server. The availability of various data transmission modes enhances the flexibility of the facility, thus eliminating what could be a major obstacle to efficient use of a core facility.

The overall goal in operating this facility is to allow the investigators easy access to sophisticated technology and to provide them with the instruction and support so that they can be responsible for acquisition, analysis and archiving of their own data.

3-Dimensional Microscopy/Confocal

Study of the Retinal Image Quality in the Human Eye by Confocal Principle

GUO LI*†, JERRI TRIBBLE,† HARRY ZWICK,* JAMES NESS,* MICHAEL REDDIX,‡ DAVID JACK LUND,* BRUCE STUCK,* SUAN BIGGERSTAFF,† AND JOHN D'ANDRE†

*US Army Medical Research Detachment, Walter Reed Army Institute of Research; †Naval Health Research Center Detachment; Brooks Air Force Base, San Antonio, Texas; ‡US Navy Medical Service Corps, USA

The image quality of the human eye may be evaluated by the double pass point spread function (PSF) or line spread function (LSF) of the human eye.[1–8] This technique has been extensively studied theoretically and experimentally since the 1950s.[1–8] This method not only may measure the on-axis PSFs or LSFs of the human eye to evaluate the foveal image quality but also may measure off-axis PSF and LSF to evaluate peripheral image quality.[6–8]

The confocal principle was applied to the double pass method to measure the PSF of the human eye and an artificial eye. The experimental setup for confocal double pass method is shown in Fig. 1. Applications of the confocal principle for improving the ratio of signal-to-noise of the PSF were demonstrated when different confocal pinhole size and position, illuminating beam size, wavelength and polarization, and on and off axis of illumination were applied.

At infinitesimal time interval a CSLO generates the PFS of an eye and composes sequential PSFs into a real time image of the eye. However, the feasibility of the confocal principle for CSLO and how the confocal principle incorporates the PSF of an eye have not been clarified in detail. In this paper the feasibility of the confocal principle for studying of retinal images was investigated. We studied all aspects of confocal principle regarding the improvements of retinal image quality.

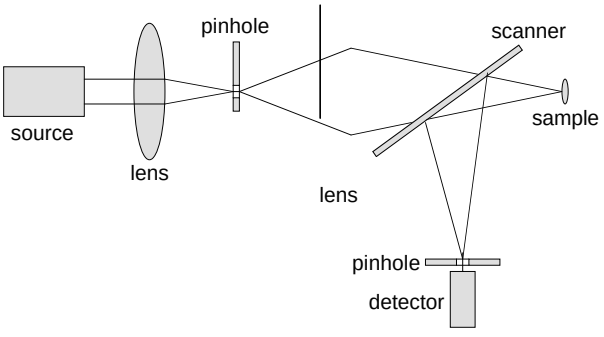

FIG. 1 The conventional confocal scanning microscope

References

1. G. Westheimer and F. W. Campell, "Light Distribution in the Image Formed by the Living Human Eye," J. Opt. Soc. Am., 52, pp. 1040-1045, 1962.
2. F. W. Campell and D. G. Green, "Optical and Retinal Factor affecting Visual Resolution," J. Physiol. 181, pp. 576-593, 1965.
3. F. W. Campbell and R. W. Gibisch, "Optical Image Quality of the Human Eye" J. Physiol. 186, pp. 558-578, 1966.
4. R. W. Gubisch, "Optical Performance of the Human Eye," J. Opt. Soc. Am., 57, pp. 407-415, 1967.
5. F. J. J. Blommaert and J. A. J. Roufs, "The Foveal Point Spread Function as a Determinant for Detail Vision," Vis. Res., 21, pp. 1223-1333, 1981.
6. W. Lotmar and T. Lotmar, "Peripheral Astigmatism in the Human Eye: Experimental Data and Theoretical Predictions," J. Opt. Soc. Am 64, pp. 510-513, 1974.
7. J. A. M. Jennings and W. N. Charman, "Off-Axis Image Quality in the Human Eye," Vis. Res. 21, pp. 445-455, 1982.
8. G. Li, H. Zwick, J. Ness, J. Tribble, J. Lund, and B. Stuck, "Evaluate the Retinal Image Quality in the Living Human Eye," presented in 1998 OSA Annual Meeting, Baltimore, MD, October 5, 1998.

Two-photon Micro-spectroscopy of Chloroplasts from *Arabidopsis thaliana*

FU-JEN KAO*†, BAI-LING LIN,‡ PING-CHIN CHENG¶

*Department of Physics, National Sun Yat-sen University, Kaohsiung, Taiwan; †Center for Neuroscience, National Sun Yat-sen University, Kaohsiung, Taiwan; ‡Institute of Molecular Biology, Academia Sinica, Taipei, Taiwan; ¶Advanced Microscopy and Imaging Laboratory, Department of Electrical Engineering, State University of New York, Buffalo, NY, USA

Two-photon excitation (TPE) has been widely applied in confocal microscopy to obtain in-depth and exotic 3D microscopic images (Denk *et al.*, 1990). TPE has the advantages of deeper penetration, less spherical aberration, and limited excitation volume (Gu and Sheppard, 1995). In this study, we employ TPE under a microscope to obtain the spectrum of chloroplast. In this way, the location of excitation can be pinpointed and the excited volume is limited so that background noise from out of focused volume can be minimized. We found that the protoplasts from *Arabidopsis thaliana* may exhibit different fluorescence spectra depending on whether chloroplasts exist in the cells. In addition, the fluorescence spectrum from the chloroplast is a time-dependent function of exposure. Intense illumination with a mode-locked Ti:sapphire laser as well as ultraviolet light (~365 nm) from a mercury arc lamp can drastically change the fluorescence spectra of chloroplasts. This change in spectra may reflect the degree of damage in chloroplasts. In contrast, the 488 nm line from an argon ion laser does not cause change in spectra.

A mode-locked Ti:sapphire laser (Spectra Physics, Tsunami) pumped by a frequency doubled solid state laser (Coherent, Verdi) provides the excitation femtosecond laser beam. An Olympus BX microscope is modified to accommodate the beam so that a tightly focused spot is formed on the image plane. A fiber coupled monochromator (Oriel, 77250) and a liquid nitrogen cooled CCD camera (SpectraSource, Orbis II) are integrated to form a very sensitive spectrometer as shown in Fig. 1. Average beam power as high as 238 mW at 790 nm was incident on the samples. Assuming a 10× objective is used, average beam intensity can reach 3KW/cm^2 at the focused spot, while instantaneous intensity can be as high as 3.7x10^{10}W/cm^2. Nonlinear optical excitation is feasible at such intensity. A set of neutral density filters was used to adjust the beam intensity.

It is well known that chloroplasts exhibit red fluorescence generally centered around 670 nm which ranges from 650 nm to 690 nm. We have found that chloroplasts also exhibit broadband greenish fluorescence ranging from 470 nm to 620 nm. The spectra of chloroplasts evolve as a function of exposure. The change in spectra can be induced either by two-photon excitation under intense irradiation of focused femtosecond pulses or by UV light from mercury arc lamp. The red fluorescence is especially susceptible to exposure. It is quickly quenched even at relatively low incident intensity. The broadband green fluorescence, however, is much more resilient to irradiation. This part of TPE time-sequenced spectra from the chloroplasts is shown in Fig. 2. The spectral response of the chloroplasts is quite exotic in that the intensity of the fluorescence rises in the beginning of irradiation and then decays to minimal at extended exposure. The spectral changes under TPE indicate that one has to be careful in applying two-photon confocal microscopy. Tightly focused laser pulses could induce damages to samples through nonlinear optical excitation.

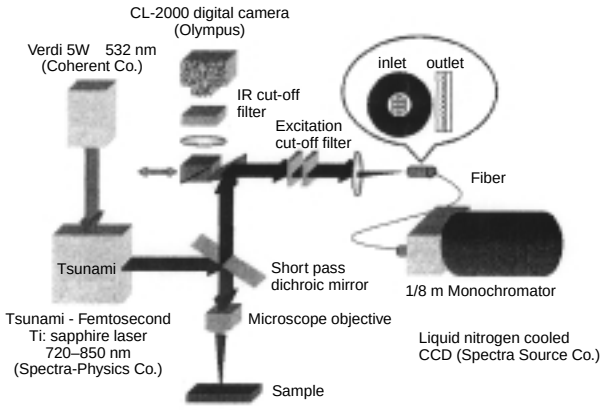

FIG. 1 Schematics of the setup of two-photon microspectroscopy

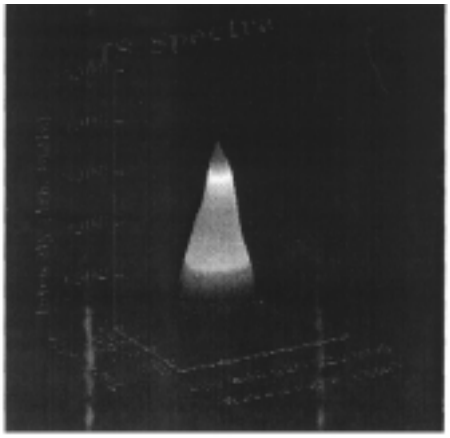

FIG. 2 Time-sequenced plot of fluorescence spectra of chloroplasts

*Supported by the Academic Excellence Program of the Ministry of Education (89-B-FA08-1-4), Taipei, Taiwan, Republic of China

References:

Denk W, Strickler JH, Webb WW: Two-photon laser scanning fluorescence microscopy. *Science* 248, 73-76 (1990)

Gu M, Sheppard CJR: Comparison of three-dimensional imaging properties between two-photon and single-photon fluorescence microscopy. J. of Microscopy 177, 128-137 (1995)

Konig K, Liang H, Berns MW, Tromberg BJ: Cell damage in a near-infrared multimode optical traps as a result of multiphoton absorption. Opt. Lett. 21, 1090-1092 (1996)

Confocal Laser Scanning Microscopy of Enhanced Green Fluorescent Protein (eGFP) Expression in Transgenic Mice

I. WALTER, H. PETZNEK,† D. KLEIN,† D. RIGLER,* M. MÜLLER,* B. SALMONS,‡ W.H. GÜNZBURG,† M. RENNER‡

Institute of Histology and Embryology, *Institute of Genetics and Animal Breeding, †Institute of Virology, University of Veterinary Sciences, Vienna, Austria, ‡Bavarian Nordic GmbH, Martinsried, Germany

The green fluorescent protein (GFP) of the jellyfish *Aequorea victoria* has been found to have fluorescein-like characteristics. GFP has become an important reporter of gene transfer and expression after transfection or infection experiments. Beside the wild type GFP, various forms like enhanced green fluorescent protein (eGFP) have been used[1,2]. Evaluation of tissue or cell specific gene expression would be of great interest especially when tissue specific promoters are used. Based on the method in Walter *et al.*[3] we processed organs of transgenic mice carrying the eGFP gene under control of the cytomegalovirus (CMV) or the mouse mammary tumor virus (MMTV) promoter for histology by formaldehyde fixation and embedding in paraffin. The CMV promoter is one of the most commonly used promoters for expression of transgenes in eukaryotic cells and is described as generally active[4]. The MMTV promoter is known as a mammary gland specific promoter.

Twenty five organs (liver, kidney, urinary bladder, adrenal gland, pancreas, spleen, esophagus, stomach, small intestine, large intestine, trachea, lung, parotid gland, heart, skeletal muscle, skin, mammary gland, submandibular gland, testis, epididymis, vesicular gland, thyroid gland, brain, spinal cord, eye) of CMVeGFP or MMTVeGFP transgenic mice and one control mouse (Balb/c) were obtained by dissection, fixed in 4% buffered formaldehyde for 6 hrs at room temperature, and embedded in Histocomp®. Sections were cut and mounted on poly-L-lysine pretreated glass slides. After deparaffinized in xylene, the sections were rehydrated in a descendent series of alcohol, washed and mounted with anti-fading medium. Deparaffinized sections were counterstained with propidium iodide at a concentration of 2 µl in 50 ml distilled water for 2 min at room temperature. Sections were evaluated with a confocal laser scanning microscope (TCS-NT, Leica) using a planapo 40× oil immersion objective (numerical aperture 1.4). An argon/krypton laser with filter setting for FITC/TRITC fluorescence was used for simultaneous two-channel detection. A series of 8 optical sections with an accumulation of 16 were merged respectively. Immunohistochemical staining with an antibody to eGFP (1:4000, Molecular Probes) was accomplished in comparison to fluorescence expression patterns of eGFP as control.

Differences between fluorescence and immunohistochemistry were few and limited to nerves, ganglia, and secretory ducts of the submandibular gland. Critical evaluation of fluorescent preparations is recommended as background fluorescence of tissues is frequent. It was demonstrated that under control of the CMV promoter eGFP expression was widespread but not ubiquitous. Further, within the permissive tissues eGFP expression was restricted to certain cell types. Beside eGFP expression in the mammary gland of female MMTVeGFP transgenic mice, male mice showed eGFP fluorescence in the ductus epididymis and in the accessory sexual glands.

In summary, evaluation of paraffin sections with a confocal laser scanning microscope is suitable for determining patterns of eGFP expression within organs and tissues at the single cell level. Screening of organs of transgene mice for eGFP fluorescence is recommended for detailed analysis of tissue and cell specific promoter activity.

Acknowledgement

The authors thank Mrs. M. Helmreich for her expert technical assistance.

References

1. Heim R, Cubitt AB, & Tsien, RY Improved green fluorescence. *Nature* 373, 663-664 (1995).
2. Klein D, Indraccolo S, von Rombs K, Amadori A, Salmons B, & Günzburg WH Rapid identification of viable retrovirus-ransduced cells using the green fluorescent protein as a marker. *Gene Therapy* 4, 1256-1260 (1997).
3. Walter I, Fleischmann M, Klein D, Müller M, Salmons B, Günzburg WH, Renner M. & Gelbmann W Rapid and sensitive detection of enhanced green fluorescent protein expression in paraffin sections by confocal laser scanning microscopy. *The Histochemical Journal* (2000, in press).
4. Bruening W, Giasson B, Mushynski W, & Durham HD Activation of stress-activated MAP protein kinases up-regulates the expression of transgenes driven by the cytomegalovirus immediate/early promoter. *Nucleic Acids Research* 26, 486-489 (1998).

Photoelastic Studies with a Laser-Scanning Microscope: Two Methods to Improve Precision

S. LÜTZE

Institut für Kunststoffprüfung und Kunststoffkunde, Universität Stuttgart, Stuttgart, Germany

1. Motivation, Set-up, and Materials

Photoelastic studies for the determination of stress fields in transparent samples and parts are well known. Previously published work concerns experiments in the linear stress-strain regime while the nonlinear case is mostly confined to qualitative evaluation of stress fields[1]. Sometimes calibration curves for the nonlinear stress-strain-relation are recorded which are then used in order to evaluate the experiments[2]. Model samples were investigated to estimate the degree of damage in reinforced composites[3]. In this paper results are reported that were obtained when stress fields rearranged in various materials after fiber breaks. For further investigations a new method has been developed which allows to correct the integral measurement effect on samples whose stress field has a rotational symmetry. Additionally, the sensitivity of the evaluation is improved.

Photoelastic studies can be carried out with a confocal laser scanning microscope by adapting a polarizer, an analyzer, and a quarter wave plate in the optical setup. When the laser beam is focussed upon the rear surface of the inspected specimen, the light wave travels twice through the sample like in reflection microscopy. However, the advantage is that no reflective layer is needed and that the image contrast is much higher. A phase image of the isochromatic can be calculated from three different isochromatic fringe pattern images phase being shifted with respect to each other by 60 degrees[3] (Figure 1). The evaluated samples consist of glass fibers (diameter 80 µm, length 3 mm) embedded in a polycarbonate matrix (PC 3200 Bayer AG). Calibration curves were obtained on samples without fibers. The correlation between stress σ and fringes δ is

$$\delta = a \cdot \sigma^3 + b\sigma^2\, c\sigma + d \qquad (1)$$

with material-specific constants a, b, and c.

2. Evaluation of the Photoelastic Laser-Scanning Images

A demodulation was carried out to obtain more information from phase images. Compared to the simple evaluation of fringes, the resolution of such grayscale images could be improved nearly up to the grayscale-resolution between two fringe orders (Figure 1). In the middle it is obvious that due to the higher resolution the local stress rearrangements can be evaluated quantitatively.

The measured effect is proportional to the integral of the optical birefringence along the path of light. Considering stress fields with rotational symmetry and a linear material-law Schuster and Scala[4] published a way to calculate the stress. The following equations solve the problem for a nonlinear material-law. A linear and nonlinear stress function (stress decreases with distance from the fiber with 1/r as known from crystals[5]) is regarded.

Linear:

$$\sigma_{ges}(z) = (\sigma_c - \sigma_n) \cdot \frac{R_i - \sqrt{z^2 + (R_o + s)}}{R_i + R_o} \tag{2}$$

Nonlinear:

$$\sigma_{ges}(z) = \frac{R_i \cdot R_o \cdot (\sigma_c - \sigma_n)}{\sqrt{z^2 + (R_o + s)} \cdot (R_i - R_o)} + \frac{\sigma_n \cdot R_i - \sigma_c \cdot R_o}{R_i - R_o} \tag{3}$$

The resulting total birefringence is

$$\delta_{ges} = \frac{4}{h_{kal}} \left[\left(\int_{G(R_o, R_i, s)}^{\frac{h}{2}} \delta_n(z) \cdot dz \right) + \left(\int_{0}^{G(R_o, R_i, s)} \delta_R(z) + \delta_n(z) \cdot dz \right) \right] \tag{4}$$

with

$$G(R_o, R_i, s) = \sqrt{R_i^2 - (R_0 + s)^2} \tag{5}$$

$$\delta_R(z) + \delta_n(z) = a \cdot \sigma_{ges}^3(z) + b \cdot \sigma_{ges}^2(z) + c \cdot \sigma_{ges}(z) + d \tag{6}$$

and

h	sample thickness
h_{kal}	thickness of calibration sample
R_o	fiber radius
R_i	radius of stress field
s	point of measurement
$\delta_n(z)$	local birefringence caused by far-field stress
$\delta_R(z)$	local birefringence caused by additional stress.

Equation (6) solved for σ_c and checked for uniqueness gives the solution (Figure 2).

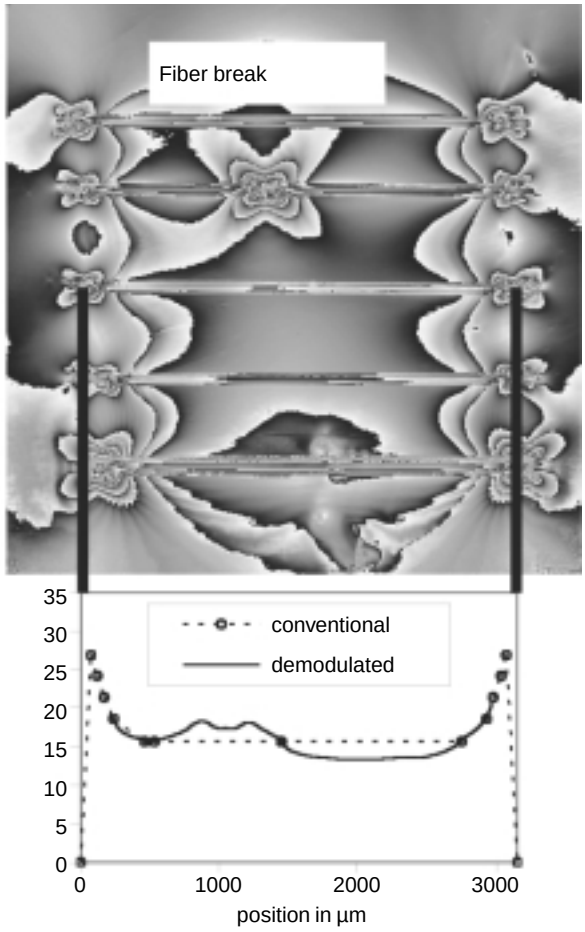

FIG. 1 Phase image of isochromatic fringe pattern (model-sample) and evaluation of stress along one fiber

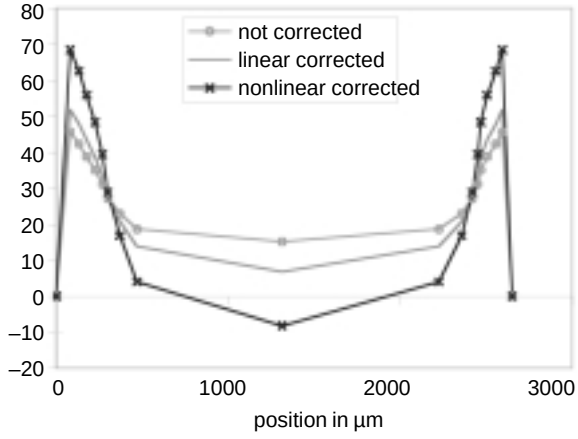

FIG. 2 Evaluation of stress along a fiber. Comparison between conventional, linear corrected, and nonlinear corrected values.

In the middle of the fiber the corrected stress decreases to negative values. As the shear stress is the main part of stress components the value should go down to zero. The higher stress peaks show that the load on the fibers is higher than anticipated. The estimation of stress field and stress displacements especially in model samples will be much more accurate when both ways of evaluation presented above are combined.

References

1. L. Dilandro, A. T. Dibenedetto and J. Groeger: The effect of fiber-matrix stress transfer on the strength of fiber-reinforced composite materials. Polymer Composites Vol. 9, 1988, pp. 209–221.
2. B. Fiedler: Mikromechanische Betrachtung der Lasteinleitung und Lastübertragung in Faserverstärkten Polymeren. PhD thesis. Technische Universität Hamburg-Harburg, 1998, p. 165.
3. S. Ritter, G. Busse: In-situ observation of the stress field of the failure process in single fibre reinforced polymers. Review of Progress in Quantitative Nondestructive Evaluation 17B, 1998, pp. 1201–1208.
4. D. M. Schuster, E. Scala: The mechanical interaction of sapphire whiskers with a birefrigent matrix. Transactions of the metallurgical society of AIME, 1964, pp. 1635–1640.
5. A. H. Cottrell: Dislocations and plastic flow in crystals. Clarendon Press, Oxford, 1965, p. 34.

High Intensity Scanning Microscopy with a Femtosecond Cr:Forsterite Laser

CHI-KUANG SUN, SHI-WEI CHU, TZU-MING LIU, AND PING CHIN CHENG*

Department of Electrical Engineering and Institute of Electro-Optical Engineering, National Taiwan University, Taipei 10617, TAIWAN R.O.C.; *Department of Electrical Engineering, State University of New York, Buffalo, NY

Accompanied by the improvements in ultrafast laser technology, there is a rapid advance in recent developments in high-intensity scanning microscopy. The primary advantage of this technique over laser scanning confocal microscopy derives from the confined excitation volume by using high-intensity-light induced multi-photon excitation fluorescence or high-order harmonic generation. This technique will not only provide a better z-axis resolution but also eliminate the need for a confocal pinhole[1]. The use of infrared excitation wavelength not only provides a deeper penetration depth but also avoids unnecessary out-of-focus photo-bleaching and photo-damages. However, the full potential of high-intensity scanning microscopy has not been realized due to the limited wavelength available in the market with a primary focus on Ti:sapphire lasers. Although this femtosecond source provides excellent images, comparative studies have shown that the Ti:sapphire wavelength is not optimized for penetrating thick biological tissues. An optimally penetrating optical source will take advantage of the diminishing scattering cross-section with wavelength, while avoiding the resonant molecular absorption of common tissue constituents such as water. In this paper we present a high-intensity microscopy technique by using a femtosecond Cr:forsterite laser source with a center wavelength of 1220–1240nm, which corresponds to the penetrating window in most biological tissues like human skin[2] and maize stem[3]. Other advantages of using the Cr:forsterite laser include that its two-photon fluorescence/second-harmonic-generation (SHG) falls in the red region and its three-photon fluorescence/third-harmonic-generation (THG) falls in the blue-to-green regions, which are visible and can be easily separated from the infrared pump-wavelength.

Like Ti:sapphire, Cr:forsterite is a broadband solid-state laser material tunable between 1167-1345 nm and is attractive for the generation of femtosecond pulse. Several hundreds miliwatts output power with pulses as short as 25 femtosecond have been produced from Cr:forsterite laser oscillators, which have been applied for optical coherent tomography[4] and transillumination imaging[5] of biomedical media, taking advantage of the high-transparency around 1250 nm. The laser constructed for this study uses a 19-mm-long Cr:forsterite crystal with a standard z-cavity and a semiconductor saturable absorber mirror. The laser is pumped with a 7W of 1064 nm light from a diode-pumped Nd:YVO_4 laser and produces 200 mW average output power with 130 fs pulsewidth tunable between 1220-1240 nm. Figure 1 shows an example of the SHG scanning image and its corresponding THG image of a bulk GaN sample (bandgap around 365nm) with a 50-μm-diameter circular defect, with the femtosecond Cr:forsterite laser source at 1230 nm. While the intensity of the SHG signal at 615 nm provides information on the strain-induced piezoelectric field, the intensity of the THG at 410 nm indicates the quality of interfaces. Figure 2 shows a photoexcited spectrum of a foliage leaf of *Epipremnum aureum* using the femtosecond Cr:forsterite laser. The sharp peak around 615 nm is SHG signal generated from bio-tissue interfaces and the broad peaks centered at 694 and 732 nm correspond to two-photon excited

FIG. 1 Laser scanning microscopy images of a bulk GaN sample with a femtosecond Cr:forsterite laser. (a) Third-harmonic-generation image. (b) Second-harmonic-generation image. (c) Transmission image.

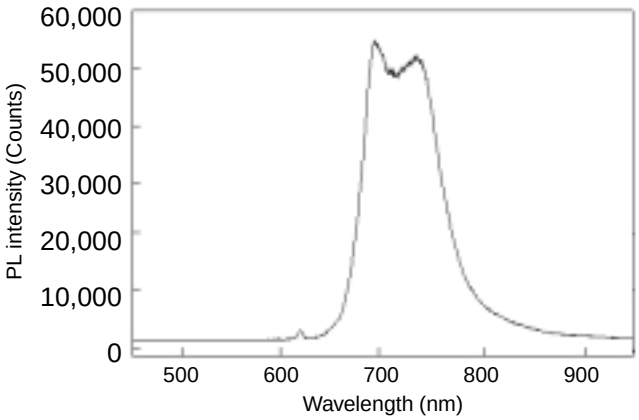

FIG. 2 Nonlinear PL spectrum of a foliage leaf of *Epipremnum aureum* excited by 1230 nm femtosecond light from a Cr:forsterite laser. The sharp peak around 615 nm is SHG signal and the broad peaks centered at 694 and 732 nm correspond to two-photon excited luminescence from chorophyll.

luminescence from chorophyll. We have also checked the luminescence from several widely used labeling dyes, including SYTO for nucleic acid stains, BODIPY TR for Amine-reactive probe, Alexa Fluor 594, Mitotracker, and Lysotracker. Excellent luminescent efficiency can be observed. Our study indicates that the Cr:forsterite laser can not only be an excellent substitute for Ti:sapphire lasers, but can also provide high penetration depth and information not available before. This project is sponsored by National Science Council of Taiwan R.O.C. though NSC 89-2215-E-002-004.

References

1. W. Denk, J. Strickler, and W. W. Webb, "Two-photon molecular excitation in laser scanning microscopy," *Science* 248, 73-76, 1990.
2. R. R. Anderson and J. A. Parrish, "The optics of human skin," *The Journal of Investigative Dermatology* 77, 13-19, 1981.
3. P. C. Cheng, S. J. Pan, A. Shih, K.-S. Kim, W. S. Liou, and M. S. Park, "Highly efficient upconverters for multiphoton fluorescence microscopy," *Journal of Microscopy* 189, 199-212, 1998.
4. B. E. Bouma, G. J. Tearney, I. P. Bilinsky, B. Golubovic, and J. G. Fujimoto, "Self-phase-modelated Kerr-lens modelocked Cr:forsterite laser source for optical coherence tomography," *Optics Letters* 21, 1839-1841, 1996.
5. S. K. Gayen, M. E. Zevallos, M. Alrubaiee, J. M. Evans, and R. R. Alfano, "Two-dimensional near-infrared transillumination imaging of biomedical media with a chromium-doped forsterite laser," *Applied Optics* 37, 5327-5336, 1998.

Probe Microscopy

Polymer-Based Materials to be Used as the Active Element in Microsensors: A Scanning Force Microscopy Study

TIMOTHY L. PORTER AND MICHAEL P. EASTMAN

Northern Arizona University, Departments of Physics and Chemistry, Flagstaff, AZ, USA

Polymer based materials may be incorporated as the active sensing elements in a variety of microsensor devices. Most of these devices take advantage of the fact that certain polymers will either expand or contract when exposed to various analytes. In order for this response to be measured, many devices incorporate a conducting material such as carbon-black within the nonconducting polymer matrix. This composite material is then deposited on some type of electrode configuration. In response to analytes, polymer expansion or contraction results in a measurable change in the conductivity of the polymer/carbon composite material. Arrays of these sensors may be used in conjunction with pattern recognition techniques for purposes of analyte recognition and quantification.[1] We have used the technique of scanning force microscopy (SFM) to investigate microstructural changes in the carbon-composite polymers PVA, PEVA, and PIB when exposed to the analytes hexane, toluene, water, ethanol, and acetone.

Using phase-contrast imaging, changes in the carbon nanoparticle distribution within the polymer matrix were measured as the polymers were exposed to the analytes in vapor phase. Changes in the surface area percentage of carbon within the composite material ranged from -21.37 % to 37.1 % for PVA, -8.9 % to 47.6 % for PEVA, and -95 % to 89 % for PIB. In most cases, the changes were reversible upon removal of the analyte vapor.

The carbon black organic polymer composites suffer from a number of problems. First, it is difficult to reliably reproduce the performance characteristics of a given set of chemiresistor elements due to uncontrollable variations in composite construction. Also, spin-coated or drop-coated carbon-black polymer composites are inherently metastable in nature and may change or degrade with time. These composite systems may not reliably adhere to a substrate surface. Repeated exposure of the metastable sensor element to analyte vapor may lead to annoying or misleading changes in performance characteristics. Finally, the carbon in the composite material may slowly release analyte material following exposure to analyte and thus have a slow recovery time.

We have also tested a new type of microsensor based on piezoresistive microcantilever technology. In these devices, polymeric volume changes (when exposed to analyte vapor) are measured directly by a piezoresistive micro-

cantilever in direct contact with the polymer. These devices have a number of important advantages over chemiresistor microsensor devices. They may operate in the liquid phase as well as the gas phase. The measured external sensor responses are simple resistance changes. Arrays of sensors would occupy only a small size (up to 100 on a 1 cm substrate). These sensors may also be applied to biomolecular systems, measuring the physical (or morphological) change of biological molecules bound to a substrate to the presence of analytes or other biological moieties. Also, no vibrating cantilever technologies are needed,[2] and the support electronics are very simple and can be made highly portable.

References

1. Eastman MP, Hughes RC, Ricco AJ, Patel SV, Jenkins MW: Application of the solubility parameter concept to the design of chemiresistor arrays. *J. Electrochem. Soc.* 146, 3907-3913 (1999)
2. Wachter EA, Thundat T: Micromechanical sensors for chemical and physical measurements. *Rev. Sci. Instrum.* 66(6), 3662-3667 (1995)

On the Electrical Properties of Dislocations in ZnS Using Electric Force Microscopy

G. F. BAI, V. F. PETRENKO, AND I. BAKER

Thayer School of Engineering, Dartmouth College, Hanover, NH, USA

Scanning probe microscopy has been used to study various defects, such as threading dislocations, screw dislocations, and grain boundaries on semiconductor surfaces. In our previous study, both grown-in and deformation-introduced dislocations in ZnS and ZnSe were detected by an intermittent mode of scanning force microscopy (SFM)[1]. However, the surface topography was the only information obtained. To detect an electric charge on dislocations a mode sensitive to an electric field has to be used. In this research, the electric potential of dislocations emerging on {110} cleavage surfaces of ZnS crystals was measured using electric force microscopy (EFM). The topography of the surface was recorded simultaneously using a non-contact mode of SFM. Undoped ZnS single crystals with the sphalerite structure were used. Dislocation bands predominantly consisting of either cation-type (Zn) or anion-type (S) dislocations were induced by scratching along either a $[\bar{1}1\bar{1}]$ or a $[1\bar{1}1]$ direction on a (110) surface. A significant difference of local distortions in electrical potential between the Zn and S dislocation bands was observed from the EFM images; see Fig. 1 and Fig. 2. In II-VI crystals, the lengths of induced dislocations are comparable with the width of the dislocation band[2]. This length of the dislocation is much larger than our scale of interest. Therefore, it is reasonable to make an assumption that the charge density is almost independent of the *z* direction. Thus, we can apply the two-dimensional Poisson's equation to the surface potential, data *V(x,y)* acquired by EFM:

$$\frac{\partial^2 V(x,y)}{\partial x^2} + \frac{\partial^2 V(x,y)}{\partial y^2} = -\frac{\rho_e(x,y)}{\varepsilon \cdot \varepsilon_0} \tag{1}$$

where ε_0 is 8.82×10^{-12} *F* m^{-1}, and for ZnS the dielectric constant ε is around 8.6. Thus, the volume density of charge $\rho_\varepsilon(x,y)$ was determined to be around +9 Cm^{-3} and –12 Cm^{-3} in the Zn and S dislocation bands, respectively. The dislocation densities were determined from surface topographic data *z(x,y)*, which was acquired by non-contact SFM, by calculating the local curvature of the surface using:

$$\frac{\partial^2 z(x,y)}{\partial x \partial y} \cdot \frac{1}{b_z} = \rho_d(x,y) \tag{2}$$

where b_z is the component of the Burgers' vector along the

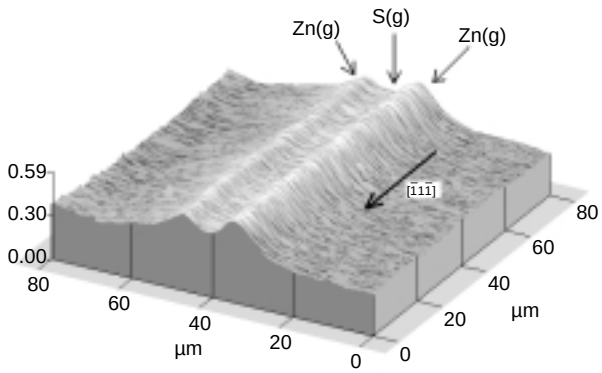

FIG. 1 A 3-D EFM image of a micro-scratching line with a direction of $[\bar{1}1\bar{1}]$. The Zn(g) dislocations moved out from both sides of the scratching line while S(g) dislocations remained in the central site of the scratching line.

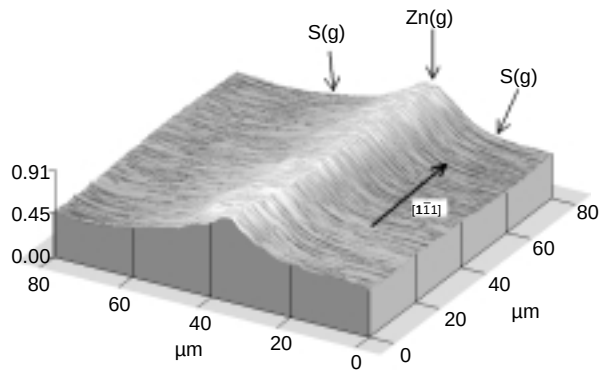

FIG. 2 A 3-D EFM image of a micro-scratching line with a direction of $[1\bar{1}1]$. The S(g) dislocations moved out from both sides of the scratching line while Zn(g) dislocations remained in the central site of the scratching line.

z direction and $\rho_d(x,y)$ is the density of dislocations. By dividing the local volume density of dislocation charge $\rho_e(x,y)$ by the absolute value of local dislocation density $|\rho_d(x,y)|$, we determined the linear densities of the dislocation charge in Zn-type and S-type dislocation bands to be around $+1.5 \times 10^{-10}$ Cm^{-1} for Zn dislocations and around -3.0×10^{-10} Cm^{-1} for S dislocations. Thus, the electric charges of resting Zn and S dislocations were determined quantitatively for the first time. The experimental results on both the donor- or acceptor-type behavior of the dislocations compare well with known theoretical models[3].

References

1. O. Nickolayev and V. F. Petrenko, "Study of dislocations in ZnSe and ZnS by scanning probe microscopy", Journal of Vacuum Science and Technology B 12(4), pp2443–2450 (1994)
2. Yu. A. Osip'yan, V. F. Petrenko, and G. K. Strukova, "Study of photoplastic effect at alpha and beta dislocations in CdS", Soviet Physics: Solid State, 15, pp1752–1174 (1973)
3. V. F. Petrenko and R. W. Whitworth, "Charged dislocations and the plastic deformation of II-VI compounds", Philosophical Magazine A, 41(5), pp681–699 (1980)

Study of NLO Materials with AFM

SAMUEL COHEN, MASATO NAKASHIMA, DIANE STEEVES

Materials Science Team, Natick Soldier Center, Soldier Systems Center, U.S. Army Soldier & Biological Chemical Command, Natick, MA, USA

One of the research programs being carried out at our laboratories is a study to find ways to counteract the effect of tunable lasers on the soldier in the battlefield. The use of lasers presents a potential threat since, even at low levels of energy, coherent laser radiation is capable of inflicting severe damage to the retina. Consequently, laser eye protection has become an area of great importance for soldier survivability. In this study atomic force microscopy (AFM) has been used to study the surface morphology of laser eye protective goggles that have been coated with nonlinear optical (NLO) film to act as protection against lasers (Haglund *et al.* 1997).

Studies have been made to characterize third order NLO material in liquid; however, in order to fabricate a solid NLO device, such materials may be incorporated into a solid host such as a polymer like polymethylmethacrylate (PMMA), that will show nonlinear refractive properties and reverse saturable absorption. Two functions of the AFM in this study were: (1) to examine the effect on polymer surface structure as a function of porphyrin concentration and (2) to examine the effect of intense photo irradiation on the film's surface to evaluate the stability of the system.

Materials that exhibit large third order (chi-3) NLO effects have shown potential for protection against laser irradiation. These materials need to allow the transmission of visible light at low intensities, but would reversibly block visible light and near infrared radiation at higher intensities, which are harmful to the eye. The material requirements include a variety of parameters such as a large NLO response, low switching energy, rapid switching times, mechanical toughness, high damage threshold, proccessability, and a wide temperature range of operation.

The materials that were examined are from the family of tetraphenylporphyrins (TPP) and tetrabenzporphyrins (TBP) that have been shown to exhibit high third order NLO response values. Zn-TPP was co-dissolved with poly methylmethacrylate) (PMMA) in chloroform at various concentrations (.17wt% PMMA, 2.8 wt%, 0.65wt% and 0.27 wt% Zn-TPP), and films were cast. AFM images of the films were obtained to determine if any order or orientation was introduced into the NLO materials as a result of incorporation into the polymer matrix.

Tapping mode AFM was employed using phase shift or phase contrast imaging because of its ability to differentiate compositional changes in heterogeneous samples. Parameters were established to ensure uniformity of procedure for all samples to see if there was any relationship between different percentages of TPP, surface morphology and functionality. The scan size was 1.0 micrometers and the scan rate was 1 Herz. At times the scan size was reduced to approximately 500nm. Integral gain and proportional gains were set at 1.0 and 2.0 respectively. The set point, which is related to the force by which the tip touches the sample, ranged between 1.5v and 2.0v and the Z range — the height of the sample was set to go no lower than 6.7nm and no higher than 100nm; however, some of the features on the surface measured approximately 4.3nm vertically — the mean height of some of the surface features was around 4.3nm.

We suggest that tapping mode AFM in the phase mode will further elucidate the structure/functionality relationship of NLO materials that are subjected to laser radiation.

Reference

Haglund, R.F., Afonso, C.N., Magruder, R.H., Massoldi, P., Osborne, D.H.: Effects of laser and particle beams on the synthesis and nonlinear optical response of nanostructures. PROC. SPIE-Int. Soc. Opt. Eng. 90-101 (1997)

Scanning Tunneling Microscopy and Spectroscopy of Organic Adsorbates: Metal-Phthalocyanines, Dipentylazoxybenzene, and Discotic Liquid Crystals on HOPG(0001)

M.HIETSCHOLD, K.WALZER

Institute of Physics, Chemnitz University of Technology, Chemnitz, Germany

We have prepared monolayers and sub-monolayers of Cu- and Sn-phthalocyanines (Pc) on (0001) planes of highly

oriented pyrolytic graphite (HOPG) substrates by thermal evaporation in UHV. In-situ STM investigation allows insight into the mechanism of the growth of the first adsorbed layer. Especially, there are characteristic linear chains of single molecules at low and medium coverages which follow the main crystallographic directions on the HOPG(0001) surface. Both of these metal-Pc molecules have a fourfold symmetry but Cu-Pc molecules are pretty flat whereas Sn-Pc molecules have their central Sn-atom protruding out of the molecular plane. In the case of the non-planar Sn-Pc molecules, we can distinguish even completely the 3-dimensional orientation of the molecule with respect to the substrate plane. There is evidence that the first molecules adsorbed are oriented with their central atoms towards the substrate surface whereas molecules deposited atop of already adsorbed ones are oriented in the opposite direction. Local current-voltage characteristics show a semiconducting behavior with some features at the gap edges.

Ordered monolayers of some liquid crystals can be prepared at ambient conditions by spriting a droplet of the isotropic liquid phase on a crystalline substrate. Usually, the nematic phase of most such (more or less planar) molecular systems show the arrangement of molecules as parallel stripes covering the substrate surface. In the case of the fairly nonplanar dipentylazoxybenzene on HOPG(0001), we could observe two ordered arrangements — one appearing as parallel stripes and, in addition, a more open parallelogram pattern. We propose a microscopic model explaining these two arrangements.

Finally, we have investigated the discotic liquid crystal Pb-octa-(2-ethylhexyloxy)-phthalocyanine prepared at ambient on HOPG(0001). The molecules of this substance have a Pc kernel which is surrounded by linear chains directed radially outwards. It has been proven to be impossible to image some ordered pattern or to get any reasonable STM image from these molecules which seem to be highly flexible and always in some (at least internal) movement. On the other hand, reproducible current-voltage characteristics over the adsorbate layer in UHV have been obtained. This paradoxon is explained by some pinning of single molecules under the STM tip during the time the characteristics are taken.

Microcratering within the Lunar Reglolith: A Fibonacci Series

ERNEST C. HAMMOND, JR.

Department of Physics, Morgan State University, Baltimore, MD, USA

Since the Apollo 11 mission to the moon, there has been substantial analysis of the lunar rocks and soil grains, utilizing more recent advances in electron probe technologies. It is the objective of this research to revisit the theories concerning the microcratering within the lunar regolith. Recent theories have included the idea that the microcratering phenomenon was caused by meteroic impacting onto the lunar surface during the early lunar history. Other theories have suggested that the microcratering was a result of secondary ejector associated with micro-meteoric and meteoric impact. This research team suggests that the microcratering may have been associated with primordial dust during and before the formation of our solar system. An examination of the debris field within each microcrater reveals the unique number of Fibonacci series of particles.

Characterization of Electron Beam Damage on a Low-k Dielectric Film using AFM

JEREMIAS D. ROMERO, JONNIE BARRAGAN, AND BRYAN TRACY

Advanced Micro Devices, Sunnyvale, CA

Introduction

The degradation of SiO_2 induced by electron beam has been characterized by many authors (1-5). The degradation, described as the dissociation of SiO_2 resulting in oxygen loss, is usually accompanied by volume loss and or volume distortion. The extent of damage depends upon the oxide preparation techniques, and that the denser the film, the more resistant it is to damage. Low dielectric constant films (low-k) for semiconductor applications are generally SiO_2 based, low density, high porosity and contains Si-H and or Si-CH_3 as the main ingredients to attain low-k properties. These properties generally result in poor mechanical strength. It is expected that these materials would have a greater extent of damage under the electron beam. In this paper, electron beam damage of a low-k film has been characterized by atomic force microscopy (AFM). The observed damage is a volume change from the loss of materials caused by the rastering of the electron beam during imaging. Varying accelerating voltages (keV) at constant current density showed the damage to be directly proportional to the accelerating voltages (keV). The motivation of the paper then is to determine a range of voltages and exposure times where damage is at a minimum.

Experimental

A low-k SiO_2 based film, with a dielectric constant 2.03, density of 1.26g/cm^3 and porosity equals 36% has been chosen for this study. The film thickness is 4000A. To induce damage, the film was exposed under SEM electron beam using 5 microns raster size at varying accelerating voltages. The accelerating voltage (keV) used was 0.8keV, 1keV, 2keV, and 5keV at a constant current density. The exposure times were also varied from 10sec, 30sec and 90sec at each voltage. AFM was then used to image the exposed surface to determine and quantify the extent of damage.

Results and Discussion

Figure 1 shows electron beam damage of the sample surface before and after exposure of 2keV electron beam for 10sec. It clear that even under a short period of exposure time, damage with a depth of ~550A can occur. Increasing the exposure time from 10sec to 30sec, and 90sec, shown in Figure 2, increases the damage in linear fashion. Also shown in Figure 2, by decreasing the accelerating voltage from 2keV to 1keV, damage significantly decreases by almost two orders of magnitude. At 0.8keV, the damage is negligible even at the highest 90sec exposure times.

Using 5keV and 2keV conditions, the extent of damage is too high that imaging can extremely alter the surface. Surface details will be lost, and obtaining a sharp and accurate representation of the surface will be difficult, if not impossible. At 1keV and 0.8keV, the damage is negligible that a more accurate representation of the surface can be attained.

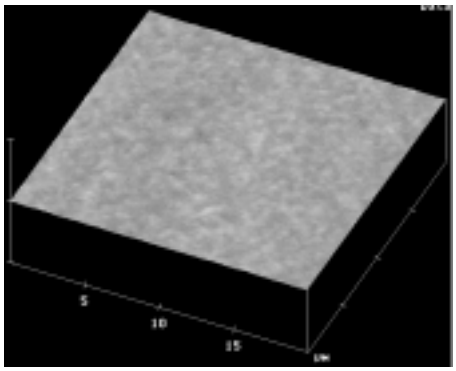

(a) Undamaged area

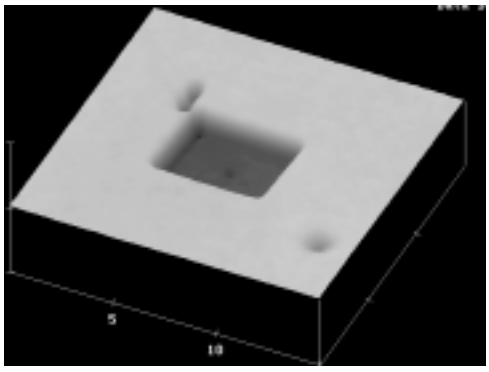

(b) Damage at 2keV, 10sec exposure

FIG. 1 Damage with 550A depth in a form of crater from electron beam exposure.

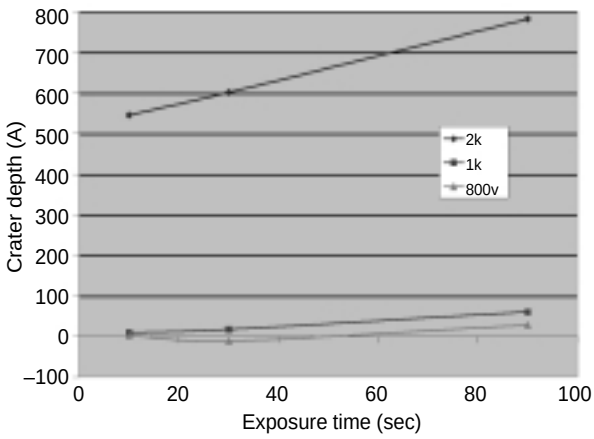

FIG. 2 Damage from 2keV, 1keV, and 800eV from 10sec to 90sec exposure.

Conclusion

Electron beam damage on a low-k dielectric film has been characterized using AFM. It was shown that to have the least amount of damage on the film surface during SEM inspection, accelerating voltages equal to or lower than 1keV is required. At these low accelerating voltages, exposure times up to 90sec still results in acceptable damage without compromising the surface.

References

1. Calliari L, Dapor M, Gonzo L, Marchetti F: Role of Core Levels' in the Electron Induced Dissociation of Silicon Dioxide. *Desorption Induced by Electronic Transition DIET IV. Proceedings of the Fourth International Workshop*, 373-378 (1990)
2. Zeller MV, Sobol PE: AES Study of Thermally Grown and Sputter Deposited SiO2 films on Si and SiC. *Symposium of Molecular Electronics and Biocomputers*, 401 (1988)
3. Juliet P, Blanchard B: An AES Study of the Electron-induced Dissociation of SiO2. *Surface and Interface Analysis*, 9, 371, (1986)
4. Pantic DM, Kapoor VJ, Young PG: Electron-beam Induced Damage on PECVD Si3N4 and SiO2 Films on InP. *Proceedings of the Symposium on Dielectric Films on Compound Semiconductors*, 88-15, 187-202 (1987)
5. King P: Auger Spectroscopy in Semiconductor Microanalysis-Applications and Artifacts. *Scanning* 20, 161 (1998)

Study and Observation of Ultrastructure of Calcium Oxalate Urinary Stones in Atomic Force Microscopy

B. CHEN, Y. CHEN, Z. WANG, G. LIU

Department of Urology, The First Affiliated Hospital, Lanzhou Medical College, China

Understanding the ultrastructure of calculus and the behavior and reaction of the crystal and the matrix, and the nature in crystal properties were the goals of this atomic force microscopy (AFM) study.

Materials and Methods

In this experiment, the ultrastructure of ten calcium oxalate urinary stones (CaOx) from ten patients who have

renal pelvic stones were studied not only by AFM but also by X-ray diffraction and scanning electron microscopy (SEM). At first, the composition of these polished samples was examined by the normal chemical qualitative analysis. At the same time, the collected powder of stones was analyzed by X-ray diffraction. Then all stones, which had been observed by AFM and SEM, were decalcified by treatment with the ethylenedia minetetraaceti acid solution (EDTA). Decalcified stones were also examined by AFM and SEM.

Results

We have obtained the AFM scan images of single crystal**s** in CaOx, and simultaneously observed the clear-cut crystal matrix. The single crystal appeared as a plate-like, striped-mass with no regular shape. The matrix's appearance was hardly different before or after it was decalcified in AFM. The crystal and matrix's images were very likely in the central nucleus region and the peripheral region in CaOx. Based on the facts above, together with the X-ray diffraction extinction rule and contrasted to the analogue in crystallography, we inferred that the space configuration of calculus oxalate was AB_2X_4. So the association between the crystal and the organic matrix may be depend upon an ion key, which was between $Ca^{2+}$and the protein matrix, carried with negative charge.

Conclusion

AFM is a practical and credible method for studying the ultrastructure of human calculus oxalate urinary stones. The single crystal's dimension was between 830nm-2670nm. The findings suggested that the corresponding matrix might absorb the microsmall crystal**s** in their different growth periods. The organic matrix appeared as a changeable fiber net filled with crystals, which was called "ghost" in past documents. The direct and synchronous observation of calculus not to be decalcified can be realized by AFM. Though the AB_2X_4 space configuration of CaOx was only a hypothesis, it reminded us that the matrix might determine the calculus growth and final external form. The combination and aggregation of the matrix and crystal was the most important stone formation.

Advances in Applications of Scanning Microscopy

Infection and Disease Development of *Diplocarpon rosae* on Resistant Rose Leaflets

J.A. MARGOITTA

Department of Biology, Stephen F. Austin State University, Nacogdoches, Texas, USA

Black spot disease of rose is caused by the fungus *Diplocarpon rosae*. Hybrid tea roses such as *Rosa hybrida* cultivar Garden Party are highly susceptible to this pathogen whereas species roses such as the chestnut rose (*Rosa roxburghii*) exhibit varying degrees of resistance. In this study, leaflets of *R. roxburghii* were artificially inoculated using a suspension of *D. rosae* conidia in order to monitor fungal development and host cell responses in an attempt to elucidate the mechanism by which resistance is conferred. Tissue samples were collected at five days post inoculation, fixed for transmission electron microscopy using glutaraldehyde and osmium tetroxide, then dehydrated and embedded in Spurr's resin. Subcuticular hyphae and haustoria were established in the resistant host and appeared highly vacuolate. The fungus did progress to the point of sporulation as conidiogenous cells and spores were evident beneath the cuticle at several infection sites. Cellular responses observed in resistant cells included deposition of wall material at penetration sites and premature necrosis. These events were effective in limiting fungal development to the point that visible symptoms were not evident.

An Ultrastructural Investigation of the Interaction Between Leaflet Tissue of *Rosa wichuraiana* and the Fungal Pathogen *Cercospora rosicola*

JOSEPHINE TAYLOR

Department of Biology, Stephen F. Austin State University, Nacogdoches, Texas, USA

During the summer of 1999, a prominent leaf spot was observed on leaflets of the species rose *Rosa wichuraiana* growing in a Nacogdoches County, Texas rose garden. Circular to angular necrotic areas, dark brown in color, formed and frequently merged so that infected leaves prematurely necrosed and abscised. Symptomatic tissue was collected and prepared for examination with scanning and transmission electron microscopy. Sporulation on the host surface involved the formation of clusters of conidiophores that ruptured the epidermis. Characteristics of the conidiophores and conidia were used to identify the pathogen as *Cercospora rosicola*. Conidia germinated apically and

laterally to form germ tubes that penetrated the host epidermis. Transmission electron microscopy (TEM) analysis revealed that the pathogen extensively colonized the epidermal layer and produced hyphae that extended through the mesophyll. Sporulation was initiated as sporogenous hyphae accumulated in the upper epidermis. Conidiophores on the lower leaf surface emerged through stomatal openings.

Scanning Electron Microscopy of the Male Phyllophaga Genitalia from Nacogdoches County Texas (*Coleoptera–Scarabaeidae*)

KIM OSBORNE AND WILLIAM W. GIBSON

Department of Biology, Stephen F. Austin State University, Nacogdoches, Texas, USA

In Nacogdoches County, Texas, there are over twenty species of *Phyllophaga*, scarab beetles commonly called Junebugs or May beetles. From late February to October, these beetles are found at night while feeding on vegetation or flying to light. The c- shaped larvae are called white grubs, and they feed on the roots of grasses and other plants. *Phyllophaga* are uniformly brown in color and adults of this genus range in size from 10mm to 23mm. Due to the overall external similarity of these various species, morphological aspects of the genitalia, observed with light microscopy at 10× and 20× magnifications, are frequently used as taxonomic characters for species level identification. This research uses scanning electron microscopy to examine and further characterize the male genitalia in species of *Phyllophaga* in Nacogdoches County.

Iridescence in the Arachnids *Salticidae phidippus*

TIMOTHY L. HENRY

The Department of Biology and The Center for Electron Microscopy, The University of Texas at Arlington, USA

Iridescence, the amplification of scattered light[1,2], is common in certain arthropods, principally members of the Classes Insecta and Malacostraca. Of the predominant forms of coloration, including pigmentation, bioluminescence and iridescence, the latter seems to be the most variable and the least understood. All of the varieties of descriptions of biological iridescence are structural in nature[3]. A few unusual physiological examples include the presence of crystalline viruses[4] and guanine crystals[5,6]. Iridescent coloration, though infrequent, is evident in certain arachnids as well. Salticid jumping spiders (Araneae, Salticidae) specifically those of the genus *Phidippus* are known for their radiant iridescent chelicerae. Functional explanations for iridescence include crypsis, conspecific signaling, and aposematic behaviors,[7] most of which have been reported in arachnids as well as other arthropods.

It was hypothesized that cheliceral iridescence in *Phidippus* was caused by the anatomical morphological stacking as observed in other arthropods[8,9] or by surface gratings[10]. Morphological features were investigated using several micrographic techniques. Gross morphology was captured using an Olympus dissecting microscope. Cryogenic sectioning was performed using an American Optics microtome. A Herbrugg Wild epilumination microscope and an Olympus Vanox microscope were used for additional light microscopy. Further analysis was done using a JEOL 33C scanning electron microscope. All SEM images were downloaded directly using Vitalscan software, while LM pictures were captured by a Spot Diagnostic digital camera system.

I found that *Phidippus* spiderlings exhibit certain general involutive iridescent qualities, due to surface gratings, that appear to be of cryptic value. These surface gratings are found as diffraction gratings on the epicuticle, and on

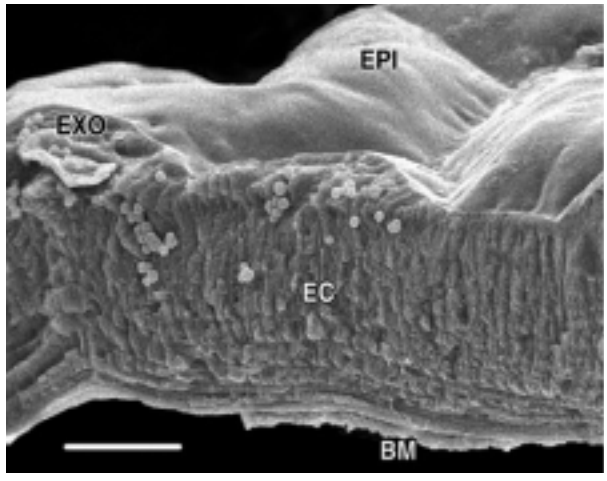

FIG. 1 Cross-section of the integument of *Phidippus audax* chelicerae at 750× showing the epicuticle (EPI), exocuticle (EXO), endocuticle (EC) and basement membrane (BM). Bar = 20 µm

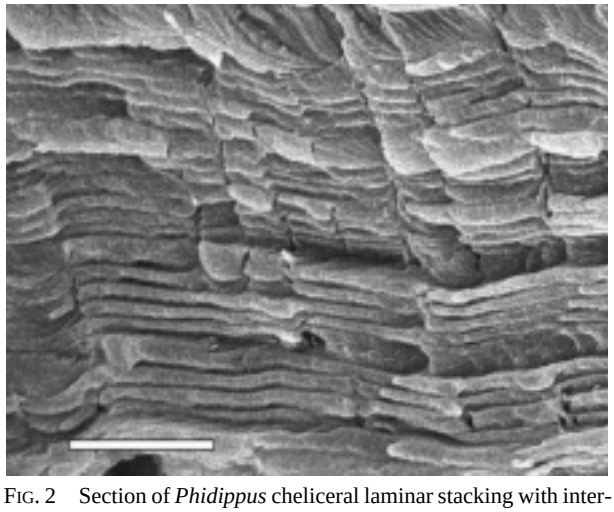

FIG. 2 Section of *Phidippus* cheliceral laminar stacking with intermittent chirping at 3300x. Bar = 5 µm

flattened seta as Bragg gratings[11]. Adult spiders of this genus exhibit cheliceral iridescence presented by common integumentary structural forms known as multilayer stacking. Of the two described stacking sequences established in arthropods, chirped and uniform[12], chelicerae of adult *Phidippus* appear to have an unusual combination of both phenomena. This anatomical amalgamation appears to be the foundation for the unusual brilliance observed in *Phidippus* chelicerae that act in conspecific and aposematic signaling functions.

References

1. Bohren, C. F., D. R. Huffman. 1983. Absorption and Scattering of Light by Small Particles. John Wiley and Sons, Inc., New York, 536 pp.
2. Bohren, C. F. 1985. Simple Experiments in Atmospheric Physics; a Serendipitous Iridescent Cloud. Weatherwise, 38: 268-274.
3. Hackman, R. H. 1971. The Integument of Arthropods. Pp. 1-62, *In* Florkin, M., and Scheer, B. T. (Eds.): Chemical Zoology, Vol. 6, pt. B. Academic Press, N.Y.
4. Willams, T. 1993. Covert Iridovirus Infection of Blackfly Larvae. Proceedings of the Royal Society of London — Series B: Biological Sciences 251 (1332):225-230
5. Bone, Q., N. B. Marshall. 1994. Biology of Fishes. 2nd ed. Chapman and Hall, New York, 253 pp.
6. Chae J. et al. 1996. Chemical composition of the integumental reflecting platelets in the iridescent copepods of the family Sapphirinidae (Poecilostomatoida). Journal of Crustacean Biology 16(1):20-23
7. Vulinec, K. 1997. Iridescent dung beetles: a different angle. Florida Entomologists 80(2):132-141.
8. Dalingwater, J.E. 1975. The Reality of Arthropod Cuticular Laminae. Cell. Tiss. Res. 163:411-413
9. Land, M.F., 1972, The physics and biology of animal reflectors. In Progress in Biophysics and Molecular Biology (Butler and Noble eds.) 24:77-105
10. Parker, A.R., D.R. McKenzie, & M.C. J. Large. 1998. Multilayer reflectors in animals using green and gold beetles as contrasting examples. The Journal of Experimental Biology. 201:1307-1313.
11. Parker, A.R. 1996. Perspective; the diversity and implications of animal structural colours. Journal of Experimental Biology. 201: 2343-2347.
12. Parker, A.R., D.R. McKenzie, & M.C. J. Large. 1998. Multilayer reflectors in animals using green and gold beetles as contrasting examples. The Journal of Experimental Biology. 201:1307-1313.

Biocompatibility of Aged Titanium-tantalum Alloys

CELINA R. ORTIZ, RUDY VILLA, ELIZABETH TRILLO, STEPHEN W. STAFFORD, AND LAWRENCE E. MURR

Department of Metallurgical and Materials Engineering, The University of Texas at El Paso, El Paso, TX, USA

Titanium alloys are an excellent choice for biomaterials because they are lightweight, have high strength, and form a natural oxide layer which makes them resistant to corrosion. Ti6Al4V is an aircraft alloy which is now being used successfully as a biomaterial. Recent studies, however, have shown an accumulation of metal ions in the tissue surrounding Ti6Al4V implants. Because metal ions can prove toxic, it has become desirable to find an alternative material for biomedical applications[1].

This project focuses on the analysis of titanium-tantalum alloys. One set of Ti40Ta and Ti50Ta samples was heat treated at 400°C for 10, 50, and 100 hours. A second set of Ti50Ta samples was aged at 500°C for 50 hours. Optical and transmission electron microscopy were utilized to determine the relevant microstructure of the material. Upon aging, both materials developed an elongated second phase (α) microstructure. However, longer aging times and higher aging temperatures reduce the length of the α-phase. Changes in mechanical properties were recorded by obtaining Vickers microhardness values and then converting these hardness readings to tensile strengths. Samples aged at 400°C and 500°C for 50 hours produced the highest hardness values (VHN 516 and 481, respectively).

Acknowledgments

We would like to thank the General Services Administration (GSA) Grant, Project #PF90-018 for providing the funding to make this research possible.

References

1. Bruneel, H., Helsen, J.A., "In Vitro Simulation of Biocompatibility of Ti-Al-V", *Journal of Biomedical Materials Research*, Vol. 22, pp.203-204, 1988.

Biocompatability Studies Using Cell Culture Testing of $Ti^{40}Ta$ and $Ti^{50}Ta$ Alloys for Implant Consideration

RUDY VILLA, CELINA R. ORTIZ, ELIZABETH TRILLO, STEPHEN W. STAFFORD, AND LAWRENCE E. MURR

Department of Metallurgical and Materials Engineering, The University of Texas at El Paso, El Paso, TX, USA

The TiTa series alloys have recently been of great interest for the use as orthopedic (surgical) implants. The popular current biomaterial used is Ti6Al4V. This aircraft alloy is used for its corrosion resistance and high strength characteristics. Yet recent studies have shown that over time metal ion discharge from these implants occurs onto the surrounding osseous and non-osseous tissue[1]. The collection of the ions can cause metallosis or irritation of the cells. In this research cell culture tests are being conducted to examine cell adhesion and cell morphology of epithelial cells *in vitro* on the polished Ti, Ta, Ti6Al4V, Ti40Ta, Ti50Ta specimens. Fixation and critical point drying was performed to prepare the cell culture samples for micro-

scopy[2]. Optical microscopy was employed to determine surface structure of metal surfaces. Pure Ti, Ta, and Ti6Al4V displayed a small fine grained homogeneous microstructure. The Ti40Ta and Ti50Ta samples contained an α phase in an $\alpha + \beta$ matrix. Fine bands of martensite were also observed in both alloys. Scanning electron microscopy (SEM) microscopy was utilized to visually examine the morphology and cell behavior on the alloys.

Acknowledgements

This project was funded by General Services Administration (GSA) Grant Project #PF90-018. We would like to thank Gladys Almodoba for cell culture instruction and Dr. J. Ellzey and Laura Dader for assisting with the critical point drying.

References

1. Prigent, H. *et al.*, 'Evaluation of the biocompatibility of titanium-tantalum alloy versus titanium," *Cell Proliferation on Titanium-Tantalum*, John Wiley & Sons, 1998.
2. Porter, Keith R., *et al.*, 'The Preparation of Cultured Cells and Soft Tissues for Scanning Electron Microscopy," *Cambridge Stereoscan Colloquium.*

Defects in Insulating Fiberglass Material Discovered and Analyzed by Scanning Electron Microscopy and X-Ray Microanalysis

J. GILLOTEAUX,* P. DAUBY,† AND D. ARNOLD*

*Department of Anatomy, Lake Erie College of Osteopathic Medicine, Erie, PA, U.S.A.; †LTV Steel Co., Cleveland, OH, USA

Man-made material for home insulation (named Rockwool® from a Dutch fiberglass company) have been used in a Belgian private home. Surprisingly, after 2 years, several of the panels, used or to be used as insulating material, have become spotted dark-grey. Each of the spots contained a dark brown and granular material. Several samples of each regions from this material were observed with light microscopy, with SEM and a Tracor X-ray energy dispersive microanalysis attachment. Under light microscopy examination, with immersion oil, the pale versus the dark areas contain the same components, i.e. fibrous and fine bulbous elements scattered throughout the material. However, in the pale samples, the round elements appear to be of the same size and appear grey to almost black over the fibrous, white to pale yellow background. Using this crude essay, one can easily understand that the presence of globular elements trap light entering into these globular components and reflected inside the wall of these spheroids before light is able to go out of the structure after scattering, i.e. creating a dark structure through light absorption and reflection. Scanning electron microscopy of the fiberglass material confirms the light microscopy observations and demonstrates that the pale material consists of a complex and intricate fibrous network of variable sized fibers ranging from 2.0 to 45 μm in diameter in which numerous bead-like or spheroidlike materials are enmeshed. These spheroids appear emptied and to originate from extremities of the cylindrical glassy fibers. It is clear that, in the case of the pale fiberglass-like regions, the material is overwhelmingly made of fibers. In the dark areas, one detects the same fiber variability and architecture as described in the pale regions but, there, abundant and extended nests of very large spheroids and ovoid bulbs appear within the matrix of fibers. Some of them can attain half a millimeter and can be detected with the naked eye. In many occasion, these fibro-nodular arrangements resemble golf clubs or Christmas ball ornaments. All of these observations strongly suggest that the fibrous material studied originates from a melted product which, in the dark areas, has retained some gaseous component which has expanded and leached out, leaving morphologically altered fibers through time and maturation. In addition, energy dispersive X-ray spectroscopic analysis does not appear to show significant differences between light and dark sample composition.

Microstructural Evaluation of Thick Copper Targets Impacted with High Velocity Tungsten Carbide Projectiles

DAVID A. ROBERSON, NATALIE E. MARTINEZ, LAWRENCE E. MURR, AND ELIZABETH TRILLO

Department of Metallurgical and Materials Engineering, The University of Texas at El Paso, El Paso, Texas, USA

The effect of high velocity impact on materials is of great concern in the area of low earth orbit space vehicles. However, much of the theory behind high velocity impact phenomena was developed in the late 50s and early 60s and ended there.

In the last decade this university, in conjunction with NASA–Johnson Space Center, has uncovered new aspects of high velocity impact phenomena. In previous works it has been noted that not only grain size, but also dislocation density influences the yield strength of a target and therefore, crater geometry. In fact, dislocation density dominates.[1,2]

This work entails the comparison of two copper targets, OFHC and columnar grained, containing drastically different microstructures and correspondingly different strengths. Impacted copper targets were characterized on the macro and micro scale. The effect of initial microstructure on the geometry and microstructure of the impact crater was analyzed and compared using optical microscopy, scanning electron microscopy, and transmission electron microscopy. Noted was a great difference in p/D_c

ratio between the two types of target material at different velocities. Differences in crater surface features were observed as well as microstructural phenomena such as microbands. Evidence of solid state flow, noted previously, was also observed. The dendritic region in the columnar grained Cu after impact was much less than in the OFHC counterpart. This material also exhibited a drastic difference in the dislocation density. The columnar grained Cu had a low initial dislocation density when compared to the OFHC, which contained dense dislocation cells.

Acknowledgement

The authors wish to acknowledge the NASA–Johnson Space Center which funds this project under Project # NAG 9-1171.

References

1. E. Ferreyra T., *et al.*, Effect of Initial Microstructure on High Velocity and Hypervelocity Impact Cratering and Crater-related Microstructures in Thick Copper Targets, Part 1 Soda-lime Glass projectiles, Journal of Materials Science, 32, pp. 2573-2585, (1997).
2. L. E. Murr, *et al.*, Effect of Initial Microstructure on High Velocity and Hypervelocity Impact Cratering and Crater-related Microstructures in Thick Copper Targets, Part 2 Stainless steel projectiles, Journal of Materials Science, 32, pp. 3143-3156, (1997).

Microscopy of the Caribbean Steel Drum

ELIZABETH TRILLO, EVERALDO FERREYRA TELLO, AND LAWRENCE E. MURR

Department of Metallurgical and Materials Engineering, The University of Texas at El Paso, El Paso, TX, USA

The Caribbean steel drum (or pan) is a musical instrument that was created a little over 50 years ago in the islands of Trinidad and Tobago. This instrument has evolved over the years mainly by trial and error methods and produces a multi-harmonic sound. Fabricating a steel drum involves deforming the lid of a 55-gallon steel drum, patterning notes on the surface, a short heat treatment procedure, and then a complex tuning process. It wasn't until recently that a few researchers[1–3] have performed any metallurgical analysis of this instrument, even though it has been in existence since the end of the Second World War. In this research, optical microscopy and transmission electron microscopy (TEM) were carried out on actual steel drum materials prior to and after deformation. The original drum lid and skirt reveal an equiaxed grain size with varying amounts of carbide precipitation. The skirt of the drum did show a smaller grain size than the drum lid. Dense tangles and poorly formed dislocation cells were observed for both sections of the original drum through TEM. Once the drum has been deformed in its first stage of processing (sinking) the grains will become flattened and distorted and the dislocation cell substructure becomes smaller and better defined. Further cold working produced by the patterning of the notes leads to a more distorted grain structure of the lid; however, the dislocation cell structure does not seem to be appreciably altered. The heat treatment of the drum is the crucial stage in producing a good tonal quality. The increase in hardness with heat treatment is attributed to strain aging and aging experiments show that higher temperatures will yield a harder material, but with currently unknown acoustical responses. In this high-temperature tempering regime a duplex grain structure is formed where new ferrite grains grow in lamellar fashion. This harder tempering regime may be a unique prospect for producing even higher quality steel drums.

Acknowledgements

This work is supported by a Mr. And Mrs. MacIntosh Murchison Endowment and a Shell Oil Company Departmental Grant at the University of Texas at El Paso. Samples were provided by Ellie Mannette at the Tuning Project at West Virginia University. We would also like to acknowledge the work and support of the Pandemonium Steel Drum Research Team: Sridhar Pappu, Christine Kennedy, Celina Ortiz, Natalie E. Martinez, and Andy Bujanda.

References

1. "Materials Science and Metallurgy of the Caribbean Steel Drum. Part I — Fabrication, Deformation, Phenomena and Acoustic Fundamentals", L.E. Murr, E. Ferreyra T., J.G. Maldonado, E.A. Trillo, S. Pappu, C. Kennedy, J. De Alba, M. Posada, D.P. Russell, and J.L. White, *J. of Mater. Sci.*, 34, pp. 967-979, 1999.
2. "Materials Science and Metallurgy of the Caribbean Steel Drum. Part II — Heat Treatment, Microstructures, Hardness Profiles, and Tuning Effects", E. Ferreyra T., J.G. Maldonado, L.E. Murr, S. Pappu, E.A. Trillo, C. Kennedy, M. Posada, J. De Alba, R. Chitre, and D.P. Russell, *J. of Mater. Sci*, 34, pp. 981-996, 1999.
3. "Connecting Materials Science and Music in Steel Drums", L.E. Murr and E. Ferreyra T., *American Scientist*, 88, Jan-Feb., pp. 38-45, 2000.

Color Cathodoluminescence of Curved-Face Diamonds

A.B. MAKEYEV, S.I. ISAENKO, S.K. OBYDEN,* G.V. SAPARIN*

Institute of Geology, Russian Academy of Science, Syktyvkar. *M.V. Lomonosov Moscow State University, Physics Department, Leninskie Gory, 119899 Moscow, Russia

Cathodoluminescence (CL) of diamonds is a traditional method to study their structural peculiarities. The electron beam initiates luminescence of the same nitrogen centres

that are excited under UV- or X-rays irradiation. The N3 defect accounts for blue luminescence and the H3, H4, S1 and S2 ones are associated with yellow-green CL-emission. The last four defects are known to be formed under the presence of radiation or as a result of plastic deformation. As the different types of defects can be identified by wavelength of CL-emission the best way to study their spatial distribution is color CL (CCL) testing in the SEM (Saparin and Obyden 1988).

Genesis of curved-face diamonds is one of the problems in diamond mineralogy that can be approached by studying their surface and sections by cathodoluminescence.

Two collections of diamonds from the Middle Timans and Urals were studied by CCL-method at the Physical Faculty of Moscow State University. The first collection comprised nine curved-face diamond crystals from the Ichet'yu occurrence (Middle Timans), where diamonds were extracted from Middle Devonian gravellites by ZAO Timangeologiya. We have generated fifty CCL-images under different magnification (from ×20 to ×1000) of seven tetrahexahedroids (065) and two split crystals of the same habit. The second collection included fourteen diamonds from the Urals: nine tetrahexahedroids (065) and five combined crystals (065+365) sawed at different orientations, that were mined from modern placers in the field of "Uralalmaz" Ltd. Seventy CCL-images were obtained for this collection.

Yellow-green luminescing spots ranging from 10 to 600 μm in size were observed on the surface of the Middle Timanian diamonds luminescing in blue spectral region. These spots partly coincide with position of green radiation pigment spots observed on the surface of the diamonds or dislocation bands. It can be inferred that these portions of the diamond were in contact with radioactive minerals: thorium-bearing monazite, thorium florencite. Concentric "agate" zonality was observed on two diamond splits. The inner blue stripes with different intensities repeated the curvature of the crystal shape. Discovered on one of the splits were a composition face and a yellow triangular core: a growing flat-faced nucleus.

The sawed surfaces of the Uralian diamonds show zonal and sectorial internal structure. In addition to blue CL, yellow-green CL was observed as concentres with regular square and triangular sectors of blue and yellow spots. In almost all curved-face crystals were found flat-faced octahedra nuclei, skeleton crystals and crystal fragments or aggregates. The last ones were geometrically selected to continue their growth and turn to regular flat-faced octahedra. Following that, the growth of the flat-faced octahedra gave way to that of curved-face tetrahexahedroids or combined crystals as the agate-type concentres. The last stage was tangential crystal growth distinguished by the absence of concentric lines, with occasionally observed fragments of crystal dissolution.

Thus, we have obtained several new facts in favour of the growth, not dissolution origin of curved-face diamond crystals:

1. Metal membranes of Au, Ag, Au_7Ag, Au_2Pd_3, Fe, Fe_7Cr, Fe_7Cr_2Ni, Ti, Pb, Sn, Bi, Cu_3Sn, Cu_3Zn_2, Ta and others (Makeyev and Phillippov, 1999) through which the growth and dissolution occur, are discovered on the surface of curved-face diamond crystals (tetrahexahedroids and cuboctahedroids) from Ichet'yu. There are other metal membranes Cu(CuS), Cu_2Zn, Sn-Cu-Pb(Au), Zn, Pb(PbS), Sn, Pb-Sn, Fe, Fe-Cr on the surface of Uralian diamonds. The similar in structure and, in some cases, in composition membranes (Cu-Zn, Fe-Mn-Ni) stay on the surface of synthetic flat-face cuboctahedra of diamonds grown in metal melt to a few mm in size during some seconds. Studying diamond crystals with fragments of metal, we have stated that membranes look like dark spots on the CCL picture because they shield both the penetrations of electrons into diamond crystal and CL-emission back.

2. The inner structure of curved-face diamond shown by cathodoluminescence (Makeyev *et al.* 2000) is characterized by concentric "agate" zonality. Moreover, the inner stripes repeat the curvature of the crystal shape. It's right evidence of the growth process.

3. Yellow-green color on CCL-images is observed on the surface of some curved-face diamonds. It can be explained by the close location of radioactive minerals: thorium monazite and thorium florencite in hypergene history of diamonds. According to another interpretation, metal membranes themselves (for example, leaden ones) contain enough uranium or thorium admixture to appear as a spot structure with radiation nitrogen centres.

It can be inferred that composition of metal membranes changed during diamond growth in the mantle. Having begun the growth in iron membrane, diamond could finish it in leaden one. This way, formation of zones with diverse concentration or various nitrogen centres can be explained, because various metals are different for penetration and solution of nitrogen. It is interesting that low-nitrogen diamonds will predominate when leaden membranes are present, because they are able to connect nitrogen.

References

Saparin GV, Obyden SK: Colour Display of Videoinformation in Scanning Electron Microscopy: Principles and Applications to Physics, Soil Science, Biology and Medicine. *Scanning* 10, pp. 87–106 (1988)

Makeyev AB, Phillippov VN: Metal membranes on the natural diamonds (Ichet'yu, Middle Timans), *Report of Russ. Acad. of Sci.*, V. 368, 6, pp. 808–812 (1999)

Makeyev AB, Obyden SK, Saparin GV: Cathodoluminescence of diamonds of Ichet'yu. *Vestnic of Institute of Geology of the Ural department*, 1, pp. 9–11 (2000)

Approximation of CL-spectra by Monochrome CL-Images Taken with the Aid of Narrow-band Optical Filter Set.

S.K. OBYDEN, M. PHILIPP,* P.V. IVANNIKOV, G.V. SAPARIN, S.V. DRONOV, S.Y. KIRUKHIN

M.V. Lomonosov Moscow State University, Physics Department, Leninskie Gory, Moscow, Russia; *Lehman College, Chemistry Department, City University of New York, USA

In the cathodoluminescence-equipped scanning electron microscope (CL-SEM), a sample is generally subjected to several minutes of irradiation under a fixed electron beam while the instrument collects localized cathodoluminescent (CL) spectrum measurements. Reversible or nonreversible changes in both quantum yield (Saparin *et al*., 1984) and spectral composition (Nazarov *et al*., 1990) of CL-emission may occur under these conditions. Organic materials and biological objects are the most sensitive to such changes under electron-beam irradiation. Shorter irradiation times may reduce such changes. There are two ways to shorten irradiation time in spectral measurements: one is to increase the monochromator wavelength scanning rate with widened input and output slits; another is to use an optical multichannel analyzer with parallel spectral acquisition. Both of these methods decrease the spectral resolution and irradiation. The use of either method must be compatible with the very low CL quantum efficiency of organic compounds.

In the first method, it is hard to make the wavelength scanning time less than several seconds. In the second method, the sensitivity of the diode array-based multichannel analyzer can be insufficient to capture any spectra. In both methods it is difficult to take a monochrome or color CL (CCL) image of the sample under low magnification for preliminary analysis. Such preliminary analysis is necessary to choose the points of interest.

In this work we describe a method to reconstruct CL-spectra taken on any single point of an object under investigation by using multiple monochrome CL-image data. These images have been taken with the aid of a three-channel registration system. This is a CCL-attachment to the SEM. The system can operate with a standard RGB-set of optical filters as well as with any other arbitrary set of filters. In addition to the RGB-filter set used for real CCL-image acquisition we have investigated the use of a set of filters that have overlapped spectral characteristics with the maximal transparencies at the following wavelengths: 420, 450, 480, 510, 540, 570, 600, 640, 680, 720 and 760 nm. As filters can readily be changed, one CCL-image and 11 monochrome CL-images can be taken after each of 5 SEM scans. Under these conditions, each point of the specimen's scanned area was subjected by e-irradiation for less than $5 \times 64\ \mu s = 0.32$ ms. Using data from 11 CL images, it has been possible to reconstruct CL-spectra for any of the $256 \times 320 = 81\ 920$ pixels of an object. This reconstruction gives a spectral resolution of about 30 nm in the 420–760 nm range. In other words, we obtain more than 80,000 low-resolution spectra after 4 scans of a specimen. In the cases when there was no need to reach the highest spatial resolution, area-based data averaging can be used to increase the signal-to-noise ratio. The 3 registration channels have been calibrated by taking into account the entire light path of each collection system; the light guide, light filter (LF), photomultiplier (PM) and the preamplifier.

Measurements included the following steps:

1. Restoration of real spectral sensitivity functions for all three PMs and the separation of PMs for measurements in red–R, green–G and blue -B regions of visible spectrum have been made on special spectral equipment. All LFs have been separated into three groups for working with RGB-channels of CCL-attachments in accordance with the spectral sensitivities of the PMs.

2. The measurements of spectral sensitivity functions $A_i(\lambda)$, where i = 1, 2, … 11 and λ–wavelength of light, were made for each LF with number i, thus forming an 11-dimensional vector function of spectral sensitivity.

3. Each function $A_i(\lambda)$ has been used for the calculation of the mean wavelength with number i–λ_i. This also serves as the abscissa for spectral amplitude values of number i. This value has been calculated as the amplitude of corresponding CL-signal normalized to the integral of function $A_i(\lambda)$ over the visible spectrum.

4. The calibration precision has been estimated by testing the light emission from standard sources with known spectra: these sources are the Hg-lamp–line spectrum, the continuous spectrum from a tungsten filament incandescent lamp, and band spectra from red, green and blue light emitted diodes (LEDs).

5. The use of special algorithms for evaluating spectral data processing has facilitated the localization of isolated narrow Hg-bands with 0.5% precision and, for LEDs, to increase the precision of spectral line parameter estimation, assuming these lines to be Gaussian.

This method of fast spectral testing of luminescent media has been applied to the study of semiconductor and organic materials in the SEM. Using heteroepitaxial GaN-layers with lateral overgrowth, we have observed two different recombination characters of CL-emission spectral bands. One, with blue lines, is associated with donor-acceptor pairs and one with a yellow line is associated with native defects of the structure. In polystyrene-based microspheres we found two types (monotonous and oscillating) of radiation-stimulated spectral band transformations.

References

Saparin GV, Obyden SK, Chukichev MV, Popov SI: Cathodoluminescent Contrast of Direct Writing Patterns in the Scanning Electron Microscope. *J. of Luminescence*, 31&32, pp. 684–686 (1984)

Nazarov MV, Nazarova TA, Saparin GV, Obyden SK, Viskov MV: A Study of Polyethyleneterephthalate (PETP) Films by Colour Cathodoluminescence in the SEM. *Scanning*, Vol. 12, pp. 315–318 (1990)

Friday, May 12

Electron/Instrument Interaction Modeling in the SEM

Simulation of Backscattering Images in the FE-SEM

RAYNALD GAUVIN

Département de génie mécanique, Université de Sherbrooke, Sherbrooke, Québec, Canada

Since the famous picture of Ogura[1], it is known that high resolution, at the nanometer level, backscattered electron (BSE) images can be obtained in a field emission scanning electron microscope (FE-SEM). Since then, there has been some new ideas about the contrast and resolution mechanisms of BSE images in the FE-SEM[2]. Even if thousans of high resolution BSE pictures have been taken in the FE-SEM since then, there is still a need of explaining the contrast and resolution of BSE images in the FE-SEM. In order to do so, a new Monte Carlo program has been developed to simulate BSE images in multilayered structures. A line scan was simulated for an AlAs layer of 1 nm thick embedded in GaAs for an 1 keV incident electron beam. For each run, 5000 electrons trajectories were simulated. The beam size was set to 2.5 nm. Such line scan is shown in Figure [1]. From this line scan, a contrast of 6 % is computed. Figure [2] shows a line scans simulated for the same condition as in Figure [1], but with energy filtration of the BSE. Only the BSE which have loss less than 2 % of their initial energy have been used in the computation of this line scan. A contrast of 6.5 % is computed. It is clear that there is no advantage to use energy filtration of BSE at 1 keV for such a small feature since the small gain in contrast is offset by the strong decrease in signal, which is about 30 times smaller.

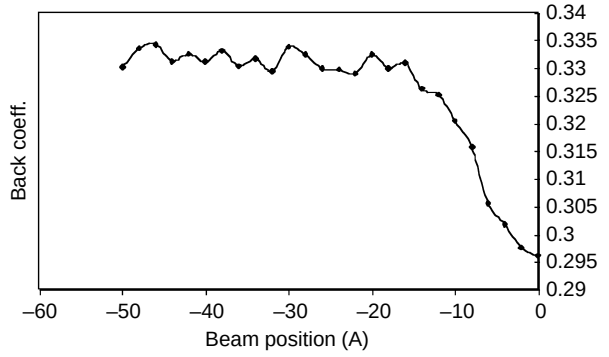

FIG. 1 Simulated backscattered coefficient as a function of beam position for a 1 nm AlAs vertical layer embedded in GaAs for a 1 keV electron beam. The scale is in A (1 A = 0,1 nm) and the AlAs layer is between –5 and 5 A.

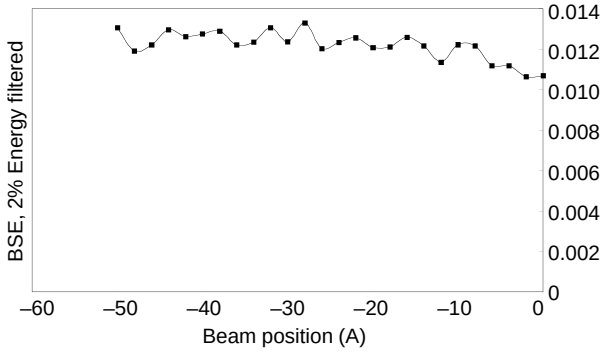

FIG. 2 Line scan simulated with the same condition of Figure [1], but with energy filtration of the BSE. Only the BSE which have loss less than 2% of their initial energy were used in the computation of this line scan.

References

1. K. Ogura, A. Ono, S. Franchi, P.G. Merli and A. Migliori (1990), Observation of GaAs/AlAs Superlattice Structures in both Secondary and Backscattered Electron Imaging Modes with an Ultrahigh Resolution Scanning Electron Microscope, Proc. of XII th Int. Cong. Elect. Microsc., Vol. 1, p. 404.
2. P.G. Merli, A. Migliori, M. Nacucchi, D. Govoni, G. Mattei (1995), Ultramicroscopy, 60, pp. 229–239.

Applications of SEM Monte Carlo Modeling to Geometry Determination in Single-Crystal Silicon Test Patterns

J. S. VILLARRUBIA, A. E. VLADÁR, J. R. LOWNEY, S. JONES, AND M. T. POSTEK

National Institute of Standards and Technology,* Gaithersburg, MD, USA

Width measurements pose a particularly problematic calibration problem. The measurement entails determining the distance between inherently dissimilar edges. Even in the simplest imaginable case, an ideal line of rectangular cross section, the left and right edges are not identical but are, rather, mirror images of one another. Any error, Δx, in the assignment of one edge is mirrored ($-\Delta x$) on the other edge, resulting in twice the error when the positions are subtracted to determine the width. In the scanning electron microscope (SEM), this makes modeling of the instrument response, for example by using Monte Carlo tracing of electron trajectories, critical to an accurate measurement.

As part of a project to test the accuracy of NIST's MONSEL[1] Monte Carlo model, we have performed measurements on the (110) face of single–crystal Si test structures fabricated in SIMOX and BESOI.[2–4] These are two technologies for producing a 200 nm to 1000 nm layer of crystalline Si on top of an insulating oxide of similar thickness. Structures containing lines in the $[\bar{1}12]$ and $[1\bar{1}2]$ directions were etched into this material. Along these directions the (110) top surface of the line is intersected at 90° by {111} sidewalls that are slow–etch planes for the KOH etchant.

Because of preferential etching, the structures are expected to have low edge and wall roughness and nearly vertical sidewalls.

We collected several series of SEM images of these structures and compared the profiles to the MONSEL result for Si lines of rectangular cross section. For SIMOX structures, the agreement was good. The SEM profiles on BESOI differed from those predicted in these significant respects: 1) The observed profiles were often asymmetrical, with one edge brighter than the other. 2) The extent of the asymmetry varied with position on the sample. 3) Even in locations where there was left–right symmetry, the observed edges were brighter than predicted. These differences necessitated revisiting the geometrical assumptions. By allowing the line to have a skewed trapezoidal cross section, with the extent of skew varying with position, we were better able to fit the observed intensities.

The extent of deviations from the expected 90° that produces the best fit to the observations is quite small, typically 0.2° of trapezoidal splay skewed to left or right by amounts ranging from –0.2° to 0.2°. Even though these are small angles, Monte Carlo results indicate very high sensitivity of the SEM profiles to angular changes of this magnitude. This high sensitivity is confirmed experimentally by tilting the sample by comparable amounts.

References

1. J. R. Lowney, A. E. Vladár, and M. T. Postek, "High-accuracy critical-dimension metrology using a scanning electron microscope," Proc. SPIE 2725, pp. 515-526, (1996); J. R. Lowney, "Application of Monte Carlo simulations to critical-dimension metrology in a scanning electron microscope," Scanning Microscopy 10, pp. 667-678, (1996).
2. M. W. Cresswell, J. J. Sniegowski, R. N. Ghoshtagore, R. A. Allen, L. W. Linholm, and J. S. Villarrubia, "Electrical Test Structures Replicated in Silicon-on-Insulator Material," Proc. SPIE 2725, p. 659, (1996).
3. J. S. Villarrubia, R. Dixson, S. Jones, J. R. Lowney, M. T. Postek, R. A. Allen, and M. W. Cresswell, "Intercomparison of SEM, AFM, and Electrical Linewidths," Proc. SPIE Vol. 3677, pp. 587-598 (1999).
4. J. S. Villarrubia, A. E. Vladár, J. R. Lowney, M. T. Postek, R. A. Allen, M. W. Cresswell, and R. N. Ghoshtagore, "Linewidth Measurement Intercomparison on a BESOI Sample," Proc. SPIE Vol. 3998 (2000) in press.

Regularization Methods for Beam Broadening Corrections

BERT W. RUST

National Institute of Standards and Technology, Gaithersburg, MD, USA

SEM scans suffer a loss of resolution because the incident beam is broadened around the focal point. This broadening is modelled by a convolution of the signal with a Gaussian kernel. Discretizing the integral equations for the convolution gives an underdetermined linear regression model. Additional assumptions about the signal must be imposed in order to specify a unique least squares solution, but even then that solution is pathologically sensitive to measurement errors in the observed signal.

At *Scanning* 97, Rust and Lowney presented a method for stabilizing the problem by truncating the singular value decomposition in a way which discards signal components that are dominated by the measurement errors, when those errors are uncorrelated (Rust and Lowney, 1997). At *Scanning* 98 they extended the method to the more difficult case, which sometimes occurs at high scan rates, where errors in adjacent pixels are correlated (Rust and Lowney, 1998).

The methods described in the present paper use a different approach, called regularization, which incorporates additional information about the desired solution in order to stabilize the problem. This is done by appending a system of linear constraints to the regression model and weighting them with a free parameter whose magnitude determines the relative importance assigned to the measurements and to the a priori constraints. The paper addresses three important concerns in using such methods: (1) choosing the proper a priori constraints, (2) picking the optimal value of the regularization parameter, and (3) using the residuals as diagnostics for assessing the quality of the resulting estimate.

References

Rust, B.W. and Lowney, J.R., "Correcting for the Effect of Electron Beam Broadening in Critical Dimension Metrology in Scanning Electron Microscopy", *Scanning*, vol. 19, 1997, pp. 222-223

Rust, B.W. and Lowney, J.R., "Correcting for Beam Broadening in Critical Dimension Metrology", *Scanning*, vol. 20, 1998, p. 220

Application of 3D Monte Carlo Simulation of Auger Line-Scanning in Analyzing Field Emission Device

HUAN YAN* AND LI CHEN†

*IKON Image Systems Solutions, Inc., Toronto, Ontario, CANADA; †Ceravision Ltd., Rutherford Appleton Laboratory, Chilton, Didcot, Oxon, UK

3D Monte Carlo simulation[1] is applied into Auger line-scanning and imaging contrast of various field emission devices[2,3] (FED). The current reported device is silicon-based Si-SiO_2-Cr sandwich-like structure, the spindle silicon tip has either diamond-like carbon coated layer or SiO_2 layer. Following phenomena have been observed in the simulation:

1. Clear O[KLL] signal from insulator layer of SiO_2 is recorded from detectors with relative large polar angle. The SiO_2 is distributed underneath the gate.

2. Recognizable Cr[LMM] Auger signal is recorded at scanning positions of the emission tip apex. It is observed regardless of the detector angle configuration, while its shape is sensitive to the angles.

Possible mechanism for the phenomena has been investigated. In which, the tip introduces the primary electron and back-scattered electron into the hidden part of cave of the FED. These energetic electrons within that part of the cave have higher probabilities to hit the cave-wall. The component of the wall includes not only surface of the substrate (*i.e.*, Si) but also that of insulator layer (SiO_2) and internal-facets of gate although they are not in radiation region of primary electron beam when it scans at the apex area of the tip. This eventually leads to detectable Auger signal from these hidden facets. Such effect may be called *Cave-Probing*.

The first phenomenon has an agreement with reported experimental work.[2] The second one is waiting to be examined by experimental observations and further studies.

References

1. Yan H, El-Gomati MM, Prutton M, Wilkinson DK, Chu DP, Dowsett MG: Mc3D: A three-dimensional Monte Carlo system simulating image contrast in surface analytical scanning electron microscopy I—Object-oriented software design and tests. *Scanning* 20, 465–484 (1998)
2. Wei Y, Chalamala BR, Smith BG, Penn CW: Surface chemical changes on field emitter arrays due to device aging. *J. Vac. Sci. Techno. B* 17(1), 233–236 (1999).
3. Chen L, El-Gomati MM: Fabrication of Tungsten-Coated Silicon-based gated emitters. *J. Vac. Sci. Techno. B* 17(2), 638–641 (1999).

Studies of Samples Having Shallow Surface Topography by the Low-loss Electron (LLE) Method in the Scanning Electron Microscope (SEM)

OLIVER C. WELLS,* MAURICE MCGLASHEN-POWELL,* MICHAEL T. POSTEK† AND ANDRAS E. VLADAR†

*IBM Research Division, Yorktown Heights, NY; †NIST, Gaithersburg, MD

The low-loss electron (LLE) image in the scanning electron microscope (SEM) is being applied to samples that are at right angles to the beam with a view to applications in the semiconductor metrology, inspection and review areas.

The LLE image is obtained by collecting electrons from a (usually tilted) specimen in the forward direction with 100 to 500 eV energy loss. This has been done in two ways. First, with a retarding-field energy filter and an external-focus magnetic lens. Second, by magnetic energy filtering with an immersion lens.

Advantages of the LLE method include the following:

1. It is insensitive to charge potentials on a poorly conducting specimen.
2. It gives strong topographic contrasts from a nearly flat surface.
3. The information depth can be as shallow as tens of nanometers even when the beam energy is as high as 10 or 20 keV.
4. Penetration effects at sharp edges are greatly reduced.
5. Morin *et al.* (1979) have demonstrated the direct imaging of crystal defects by the high voltage LLE method.
6. However, the sample must not be too rough.

As a result of this technique, imaging of shallow topography is improved, and penetration fringes at sharp edges are reduced.

References

Morin,P., Pitaval,M., Vicario,E., and Fontaine,G., (1979). Scanning electron microscope observation of single defects in solid crystalline materials, Scanning, vol.2, 217–224

SMART—Routines to Measure SEM Resolution and Performance

DAVID C. JOY

EM Facility, University of Tennessee, Knoxville, TN

The imaging resolution of a scanning electron microscope (SEM) is usually the parameter of most interest to a user of the instrument. It is, however, a quantity that has been found difficult to measure reliably and as a result most users have to take the specifications and quoted performance of current instruments on trust because they are incapable of testing and verifying the values for themselves.

The basis of an objective and reliable method for the measurement of resolution is the power spectrum (2-dimensional Fourier transform) of the image[1]. This displays the intensity distribution of different spatial frequencies in the image, with the frequency increasing along the radius from the center of the transform. At some frequency the signal becomes submerged in the random noise of the system. This frequency then defines the information limit of the SEM and hence the achieved spatial resolution. An elegant commercial system which can perform this measurement in real time is now available[2]. Unfortunately this approach also has two fundamental problems: first, the technique assumes that the sample being examined contains information at spatial frequencies beyond the resolution limit of the microscope. Samples which satisfy this condition for present high resolution machines are notably rare although

recent work by Postek *et al.*[3] may provide a suitable test specimen. Second, it is impossible to distinguish signal from noise on a pixel by pixel basis, so the boundary between signal and noise cannot be accurately determined and hence the resolution figure remains elusive. It is that difficulty which is considered here.

Two approaches which can alleviate this problem are available. The first uses the procedure of cross-correlation[4] which compares two overlapping regions of the same micrograph and plots the cross-correlation function (CCF) between them. The width of the CCF is a direct measure of the resolution, and the peak to background ratio of the CCF is an estimate of the signal-to-noise ratio of the image. By sampling the image twice and looking for correlated features this method avoids the problem of distinguishing signal from noise since noise is always uncorrelated. For successful application, however, the image needs to be homogeneous and free from extremes in signal level. An interesting application of this approach is a rapid technique for the measurement of SEM spot size. Using a simple STEM adapter, the bright field image of a thin carbon film is obtained and the CCF method used to deduce the resolution. Since beam broadening is negligible under these conditions, the resolution is equivalent to the probe size.

A second approach[4] uses two micrographs of the same area, the images being recorded sequentially. These images are superimposed, but with a small linear offset, and the power spectrum is obtained as before. Intensity from correlated detail in the images is now modulated by parallel fringes while random noise remains unmodulated. The boundary representing the resolution cut-off is now clearly identified as the extremity of the fringe pattern permitting an accurate measurement to be obtained.

Code implementing each of these procedures has been written in the form of a macro for use with the NIH Image, or SCION Image, image processing programs. This code, called SMART (Scanning Microscope Analysis and Resolution Testing) works identically in either program, carries out the analysis without operator intervention on any of the digital image formats recognized by the programs, and produces a result within a second or two. SMART can be downloaded from http://web.utk.edu/~srcutk

References

1. TA Dodson and DC Joy (1990), Fast Fourier transform technique for measuring SEM resolution, Proc. 12th ICEM, 406–407.
2. Micrologia from SPECTEL Research. See AE Vladar, MT Postek and MP Davidson (1998), Image sharpness measurement in scanning electron microscopy—Part II, SCANNING 20, 24–34.
3. Youn HK and Egerton RF, (1997), Resolution measurement of SEM using CCF, Proc. Micros.Soc. Canada 24, 62–63.
4. Erasmus S J and Smith KCA (1980), On-line computations of diffractograms for the analysis of SEM images, Inst. Phys. Conf. Ser. 52, 73–77.

LISPIX: Image Processing and Data Visualization Tool for the PC and Macintosh*

DAVID S. BRIGHT

Surface and Microanalysis Science Div., National Inst. of Standards and Technology, Gaithersburg, MD

Lispix is a public domain scientific image processing and analysis program maintained by the Microanalysis Group at NIST. It is a general purpose program with additional special purpose tools with enough utility to be of general interest. Lispix is an update of MacLispix,[1] a public domain image processing system for the Macintosh,* with tools for a variety of image processing problems such as: analysis of diffraction spots,[2] uniform display of x-ray maps,[3] determination of fractal dimension of particle outlines,[4] and analysis of image stacks or data cubes.[5] Due to interest from the PC community, the software now also runs on both Windows* and the Mac*, is public domain, and available along with source, instructions, and sample images.[6]

Lispix accommodates TIFF files and raw image files (no header), both with pixel types of signed and unsigned 8, 16 and 32 bit integers, 4 and 8 byte IEEE standard floating point numbers, and 3x8 bit RGB color. Lispix has a variety of standard image processing operations, such as thresholding, edge finding (gradient), filtering, Linear Hough Transform, and particle measurement. Lispix also reads JPEG files, and a few other image formats.

Lispix has a variety of scaling and enhancement features. For example, clipped scaling (trimming outliers) is especially useful for display of x-ray maps, and images with noise or very bright or very dark artifacts. Scaling enhances visibility of features, and is done using a copy of the image, so that the original is available for measurements, such as intensity mean, min, max, variance, etc. Once an image is scaled, manipulation of the palette, or color look up table can further enhance visibility, or mark intensity ranges of interest. Lispix has these adjustable color scales: gray level, thermal, thresholding, color bars, and gamma correction. There is also a logarithmic banded color scale[3] that, without adjustment, is useful for visualization of images with up to three decades of dynamic range.

Lispix now accommodates large images by means of a navigator window, similar to Photoshop*. Lispix also accommodates groups; i.e., images in the group can be zoomed and scrolled, arranged on the screen and processed all together.

Lispix has a periodic table designed for selecting elements for various analyses, but is useful by itself. Clicking on an element displays a list of its properties and isotopes. The table can be colored according to any of the numerical properties in the list.

To facilitate examination of groups of registered images displaying different signals such as chemical composition or spectrum interval, Lispix can make RGB color overlays and XY or XYZ scatter diagrams. For more than three

images, the data cube facility is useful, and includes Principal Component Analysis. A selection of the component images often represents the original data. Visually checking the component images and examining a reconstruction of the original data out of the components, both indicate whether or not the data is well represented.

* Certain commercial equipment or software are identified in this report. Such identification does not imply recommendation or endorsement by the National Institute of Standards and Technology, nor does it imply that the equipment or software identified are necessarily the best available for the purpose.

References:

1. D.S. Bright, "MacLispix: A Special Purpose Public Domain Image Analysis Program for the Macintosh.", Microbeam Analysis 4 (1995) 151-163.
2. D.S. Bright et al., " Spot Measurement Tool for Diffraction Pattern Analysis", Microscopy and Microanalysis 4 (Proc., suppl. 2)(1998) 60-61.
3. D. E. Newbury, and D. D. Bright, "Logarithmic 3-Band Color Encoding: Robust Method for Display and Comparison of Compositional Maps in Electron Probe X-ray Microanalysis", Microscopy and Microanalysis 5 (1999) 333-343.
4. D.S. Bright, "Richardson Plots for Fractal Dimension Characterization of Boundaries of Digitized Grains and Particles", Microscopy and Microanalysis 3(Proc., suppl. 2) (1997) 897-898.
5. Bright, D.S. " PC/MAC* Image Processing Freeware For Examining Spectral Images.", Microscopy and Microanalysis 00 (Proceedings of Annual Conference, July 31-August 3, 2000, in print).
6. Available from http://www.nist.gov/lispix/

Reduction of Charging Effects Using Pseudo-random Scanning In The Scanning Electron Microscope

K.W. LEE, J.T.L. THONG, W.K. WONG*

Centre for Integrated Circuit Failure Analysis and Reliability (CICFAR), Faculty of Engineering, National University of Singapore, Singapore; * Institute of Materials Research and Engineering (IMRE), Singapore

In a typical scanning electron microscope (SEM), the electron probe is deflected in a raster fashion across the specimen. The primary disadvantage of the conventional raster scan pattern is the immediate proximity of consecutive sampling pixels in the x-y plane. The next point to be scanned is immediately adjacent to the previous point except for the last point at the end of the scan line. This proximity means that each point suffers from electric field effects generated by charges on the previous scan point[1]. On an insulating sample this problem can be severe, as charges do not have sufficient time to dissipate. The cumulative interaction of adjacent sampling points may manifest itself as charging artifacts. Charging artifacts are common problems encountered by many SEM users, especially when imaging non-conductors in a slow scan mode for image acquisition.

To reduce the proximity charging effect due to neighbouring pixels, the ideal scan pattern should deflect the beam in a manner such that each scan point is located as far away as possible from the next sampled pixel in both space and time. Reduction of negative charging effects is particularly effective with this scheme. Even if the localized charges do not discharge completely due to inhomogeneities in the specimen, the dispersion of charge on the sample will at least alleviate specific topographic contrast observed in some insulators.

A pseudo-random number generator algorithm is adopted to generate a two-dimensional scan table. The algorithm that was chosen makes use of the equation:

$$I_{J+1} = IF + I_J$$

where IF is the Interlace Factor
I_{J+1} is the location of the next pixel
I_J is the location of current pixel

In this algorithm, the two-dimensional image matrix is mapped to a one-dimensional image strip. The first point of the image strip is the origin (0,0) of the image plane. A specified value of the IF is then used to calculate the location of the next point. Hence, IF is also defined as the number of pixels to skip from the present point to the next point. After the first parse of the one-dimensional array, the algorithm loops back to the beginning of the array and runs iteratively until all the pixels have been scanned once. The resultant one-dimensional scan sequence is then remapped back to the two dimensional plane to form the final scan pattern that is used for the pseudo-random scan.

A digital signal processor (DSP) card plugged in a Pentium personal computer is used to control the pre-generated raster or pseudo-random scanning vectors, through two 16-bit digital-to-analogue converters. The analogue video signal from the detector is then digitized by the DSP with a 16-bit analogue-to-digital converter, which is scaled to 256 gray levels before it is displayed as a real-time image in Windows 98.

Experiments are carried out to investigate and compare the quality of SEM images obtained using the conventional raster scan and the proposed pseudo-random scan. SEM images of gold-coated passivated IC are used to demonstrate the potential of random scan. Sub-surface charging of the IC specimen results in a deterioration of image quality as evident in Figure 1. The charging artifact manifested itself as a defocused image and charging streaks using the conventional raster scan. The charging artifacts mentioned earlier are eliminated when the SEM image is acquired using pseudo-random scan, as shown in Figure 2.

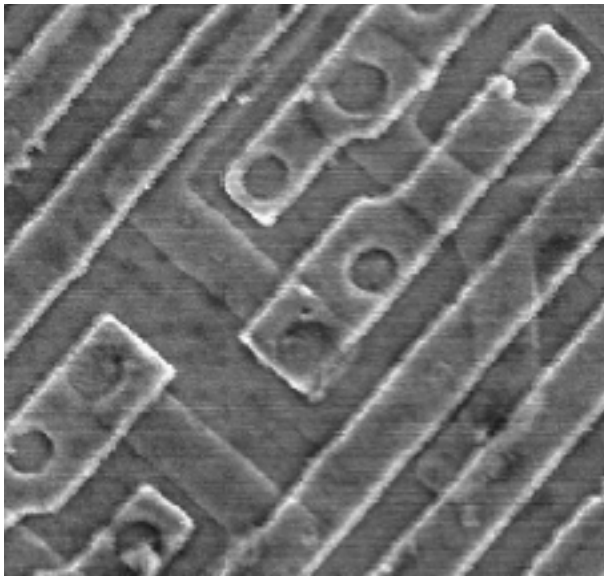

FIG. 1 SEM image acquired with conventional raster scan.

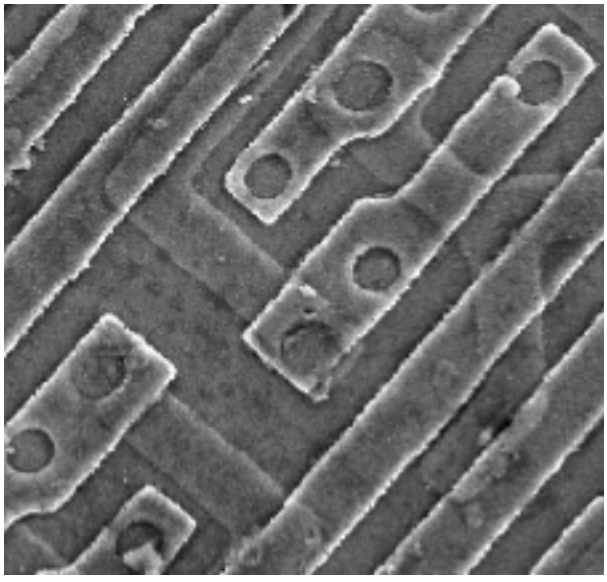

FIG. 2 SEM image acquired with proposed pseudo-random scan.

Reference

1. M. T. Postek: Low Acceleration Voltage Inspection And Linewidth Measurement In The Scanning Electron Microscope. Scanning Electron Microsc, 1065–1074 (1984).

A High Resolution Lens Attachment for SEMs

A. KHURSHEED, N. KARUPPIAH* AND S.H. KOH

National University of Singapore, Singapore; *Institute of Materials Research and Engineering, Singapore

At present, scanning electron microscopes (SEMs) need to be specially designed to operate in the high-resolution in-lens mode, where the specimen is immersed in a strong magnetic field. These SEMs are not widely used, since they are expensive dedicated high resolution instruments, and only allow for the use of thin specimens (less than 3 mm high). A new compact add-on objective lens for the scanning electron microscope (SEM) has been designed and tested. The add-on unit is based upon a permanent magnet in-lens design. Fig. 1 shows simulated flux lines for the add-on lens. These results were obtained by the use of KEOS[1]. The lens is less than 35 mm high and can be fitted on to the specimen stage as an easy to use attachment. Hall probe measurements of the lens axial field were made and agree well with simulation predictions. The KEOS programs predict that a 1 keV beam focuses 1.24 mm below the lens top plate and that the spherical and chromatic aberration coefficients are 0.537 and 0.788 mm, respectively. The focal length for these conditions is predicted to be 1.14 mm. These parameters are around an order of magnitude better than that for conventional SEMs. The lens is typically expected to improve the spatial resolution of the SEM by a factor of three. Apart from the extra attachment to the specimen stage, the SEM with the add-on lens functions as normal. The in-lens unit can comfortably accommodate specimen heights up to 10 mm. The new add-on in-lens unit opens up the possibility of operating all existing conventional SEMs in the high resolution in-lens mode.

To confirm the above predictions, a prototype add-on lens was constructed and placed on the specimen stage of a JEOL 5600 tungsten gun SEM. Fig. 2 shows images of a tin-on-carbon specimen, with and without the add-on lens. A 5 keV beam was used in both cases. A working distance of 5 mm and a magnification of 70,000 was used for the image obtained without the add-on lens. All other operating conditions were identical. A comparison of these images demonstrates that the add-on lens improves the spatial resolution performance by approximately a factor of three: the minimum feature separation is approximately 20 nm without the lens, and around 7 nm with the lens.

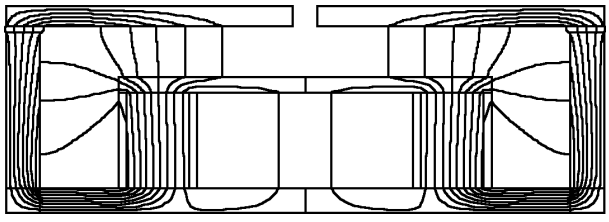

FIG. 1 Simulated flux lines for the new add-on objective lens

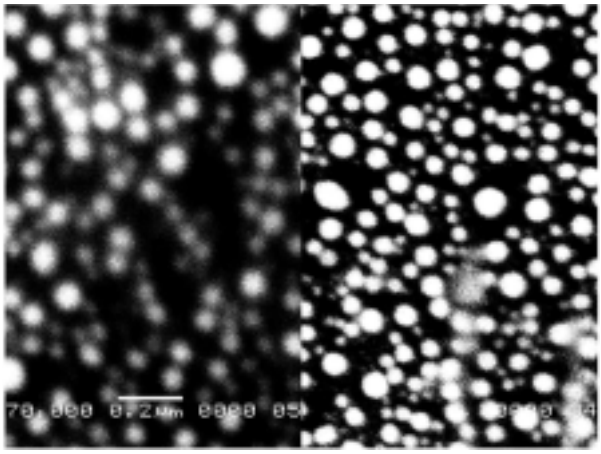

FIG. 2 SEM images of a tin-on-carbon specimen at a primary beam voltage of 5 kV.

These results provide initial confirmation that the high resolution add-on objective lens is in principle feasible.

References

1. A. Khursheed, "KEOS, The Khursheed Electron Optics Software", (1995), Electrical Engineering Department, The National University of Singapore, 10 Kent Ridge Crescent, Singapore 119260.

Food Structure and Functionality Symposium

Microrheology: New Tools to Study the Local Properties of Soft Condensed Matter

A.R. BAUSCH

Division of Engineering and Applied Sciences, Harvard University, Cambridge, MA

The origin of many of the unique features of soft materials are the larger scale structures that make up the material; these structures are typically larger than molecular in scale, yet are still much smaller than the size of the sample itself. The dynamics and interactions of these larger scale structures are often responsible for the rheological properties of the material. Even more importantly, soft materials are often highly inhomogeneous and are comprised of many different components, and the bulk elasticity of the material does not at all reflect the properties of the constituents. However, it is the properties of these constituents that are crucial in understanding the behavior and function of the material.

In order to understand the relation between the microscopic structure, the local rheological properties and the bulk properties new techniques have been developed. One very promising technique is magnetic tweezers, which allows the application of local forces up to 10 nN on paramagnetic beads with a diameter of 4.5 μm. This technique allows the measurement of local viscoelastic properties of the membrane of living cells and the observation of the effect of drugs in real time. The technique also allows the determination of the local viscoelastic properties of the cytoplasm of single cells. By observing the deformation field the heterogeneity of the cytoplasm was demonstrated.

Another very promising approach is the observation of the thermal motion of colloidal probe beads, which are embedded in a polymer network. By applying the generalized Stokes-Einstein relation, the local properties can be determined. In the case of homogeneous networks the comparison of bulk measurements and microrheological data show an excellent agreement. However, in inhomogeneous samples large discrepancies can be observed.

Microrheology, a New Approach in the Study of Structure-/Function-relationships in Food Systems

M. PÂQUES*†, R.H. TROMP*‡, G.A. VAN AKEN*‡

*Wageningen Centre for Food Sciences, Ede, The Netherlands; †Unilever Research Laboratorium Vlaardingen, Vlaardingen, The Netherlands; ‡NIZO Food Research, Ede, The Netherlands

In order to gain insight into the texture perception of foods, we need to study microstructure heterogeneity. Many of the techniques used to characterise food microstructure properties average out local differences. Due to this they only provide insight in the (rheological) bulk properties. This is considered to be a major limitation. A new concept was developed which combines a microscope, and physical characterisation and manipulation techniques in a hybrid configuration. This new approach ("micro-rheology") will allow the characterisation of (mechanical properties of) microstructure heterogeneity on a micrometer length scale. It will open new perspectives for the study of "structure–function relationships" of food systems, and will overcome existing limitations of instrumental approaches that are generally excepted.

Food products and food model systems consist of a limited number of main components: fat, protein, carbohydrates, water and air. In addition, one can identify ingredients that have their functionality in health promoting effects. The properties of the products and model systems are the result of careful selection of ingredients based on their chemical, physical and nutritional properties in combination with the application of well defined processing conditions. The resulting structure determines, among other things, appearance, mouthfeel, rheology and, shelf life. It forms the physical 'bridge' between the molecular

properties of the individual components with the functional properties of the product or food model system. In-depth knowledge of the structure/functionality relationship is crucial for the improvement of functional properties of existing products and the design of new ones. Microstructural characterisation is indispensable for any research in this area.

Aspects of the microstructure related to the connectivity of sub-structures can be studied by analysis of the 3D spatial arrangement. Only a limited variety of techniques allows the 3D visualisation of the microstructure. Examples are CSLM, TEM and SEM tomography, specialised LM, NMR-imaging and X-ray tomography. Each of these techniques allows the visualisation of only certain aspects of the microstructure, and the 3D spatial arrangement is visualised qualitatively by reconstruction of sequential 2D cross-sections. To derive quantitative information image analysis is needed, preferentially in 3D. This is also an area of great importance in which, however, only very limited tools are available. Further development is needed.

FIG.1 Based on our experience we recognise the structural elements (cups) shown, and arrive at an interpretation of the organisation of the composite structure. But we need additional information to confirm (Fig.2) this interpretation.

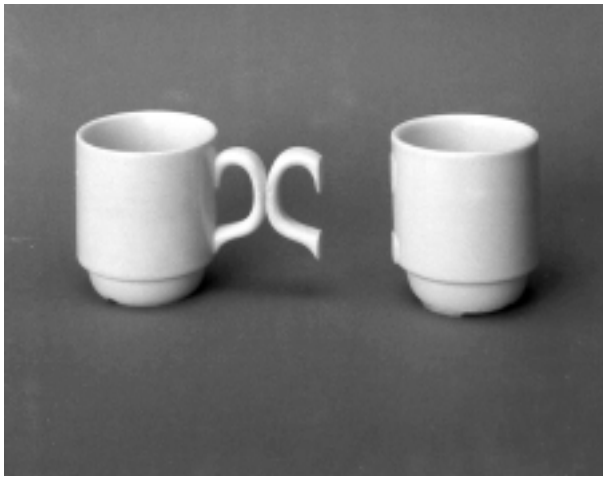

FIG.2 Only by displacement of the cups relative to each other the unexpected organisation was revealed, and provides insight in the interactions at work.

The real-time observation by microscopy of dynamic processes will significantly contribute to the growing insight in the microstructural bases for important attributes; e.g., the melting behaviour and progression of structure breakdown, and how these relate to oral perception. The instrumentation used for this type of work demands suitable temporal resolution for image acquisition and signal sensitivity.

All these techniques gain insight in the structure, but not in the interactions that exist between the structural elements in the structure. When a 3D arrangement of structural elements is visualised no information is obtained on the strength and character of their interactions. To illustrate this the spatial arrangement of two known objects (Fig. 1) is shown.

Suitable analytical tools to obtain direct information about local interactions between relevant structural elements and the related rheological properties are still missing. This is considered to be the main impediment to progress in the study on the relation between structural properties and functional properties, crucial for a full interpretation of structure-function relationships. A hybrid configuration of a microscope with a physical characterisation technique and a physical manipulation technique is a possible approach to overcome this limitation.

Comparison of Scanning Electron and Atomic Force Microscopy of Surface Finishes on Stainless Steel That Reduce Bacterial Attachment

J.W. ARNOLD AND G.W. BAILEY*

USDA-ARS, Russell Research Center, Athens, GA, USA; *Ecosystems Research Division, NERL, EPA, Athens, GA, USA

Bacteria adhere to food products and processing surfaces that can cross-contaminate other products and work surfaces (Arnold, 1998). Using materials for food processing surfaces that are resistant to bacterial contamination could enhance food safety. Stainless steel, although susceptible to bacterial attachment, is the most frequently used material for construction of equipment used for food processing. Treatments of stainless steel were evaluated for effectiveness in improving the resistance of the surface finish to bacterial attachment. Two methods of microscopy were partnered to correlate form and function of surface finishes. Relative differences in the topography and morphology of surface finishes were measured by atomic force microscopy (AFM) and compared with changes in bacterial attachment and early biofilm formation as shown by scanning electron microscopy (SEM).

Natural bacterial populations collected from the food processing environment were assessed for their affinity to attach to surfaces. Aliquots (1- ml) of meat rinses were incubated in trypticase soy broth 18 hr, 37°C. Then the culture was diluted in broth to absorbance (410nm) of .3 as measured by spectrophotometry. Stainless steel disks (1-cm diameter) were added, and the cultures were grown to an absorbance of .6, 37°C. The disks were removed from the bacterial suspensions, rinsed in 0.1 M sodium cacodylate buffer, and fixed for 2 h in 2% glutaraldehyde, 2% paraformaldehyde in buffer. After rinsing in buffer, the samples were dehydrated in 50 to100% ethanol and critical point dried. The disks were mounted on aluminum stubs, sputter-coated with gold-palladium, and examined in a JEOL 6400V SEM at an accelerating voltage of 5 kV. Triplicate counts of bacterial cells on micrographs were taken from each of two trials covering 10 random fields of view. Beginning biofilm was measured as clumps of cells that showed extensive intercellular fibrils at high magnification SEM (Arnold and Shimkets, 1988a).

After the finishing treatments the surfaces could be distinguished visually. For example, the untreated surface of the 304 stainless steel was smooth and light gray, the sandblasted surface was a darker gray and uniformly pitted, and the electropolished surface was mirror-like and very smooth and shiny. The differences in the surface finishes were confirmed by SEM. Bacteria readily attach to the untreated surface (Fig. 1a). As bacteria accumulated on the untreated stainless steel, they exhibited typical phenotypic properties of biofilm formation. The sandblasting pitted the surface, and with SEM the pit-marks seen by visual observation appeared as "craters" to which bacteria attached even more frequently (Fig. 1b). The steel-ball burnished surface was much smoother, but was not the least resistant to bacteria (Fig. 1c). Stainless steel that had been electropolished showed significantly fewer bacterial cells and beginning biofilm formations than the other treated surfaces. The electropolished surface was difficult to image with SEM because the surface was so smooth and featureless (Fig. 1d).

Surface morphological characteristics are determinants for the attachment of bacteria (Arnold and Shimkets, 1988b). Measurements of the surface topography by AFM confirmed and extended the SEM data. The disks for each finishing treatment analyzed by AFM were stamped from the same sheets used for SEM. Disks were removed from the bacterial suspensions described above and examined

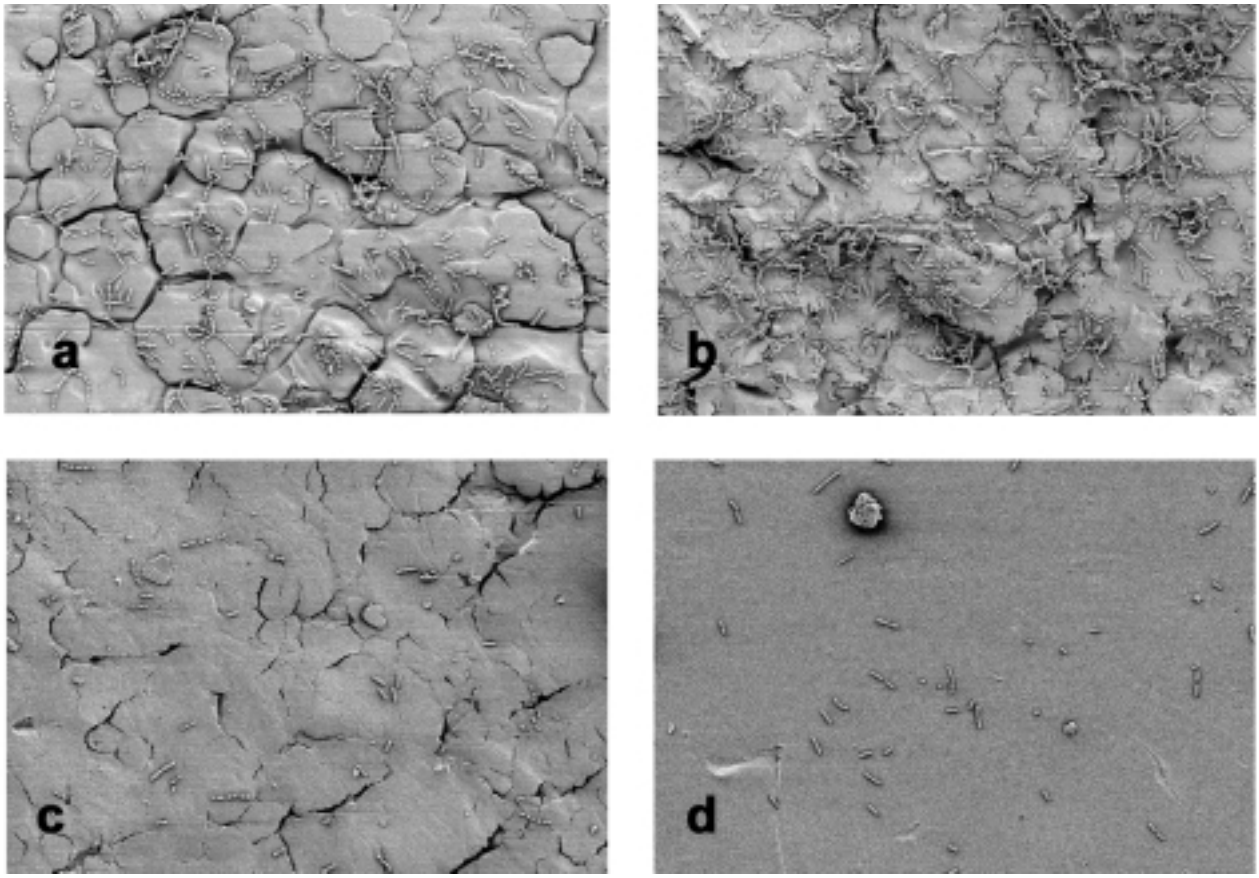

FIG. 1 Bacteria readily attach to an untreated stainless steel surface (Fig. 1a). The sandblasting pitted the surface, and with SEM the pit-marks seen by visual observation appeared as "craters" to which bacteria attached even more frequently (Fig. 1b). The steel-ball burnished surface was much smoother, but was not the least resistant to bacteria (Fig. 1c). Stainless steel that had been electropolished showed significantly fewer bacterial cells than the other treated surfaces (Fig. 1d).

directly. Changes in AFM surface measurements had the same relative differences as the data from the bacterial counts for the SEM studies, with the electropolished finish showing the most reduced roughness parameters. These data demonstrate that AFM can predict the potential for bacteria to attach and form biofilms on surfaces, without the time-consuming preparations and tedious counting required for SEM.

Appropriate finishing treatments on stainless steel surfaces can improve the resistance to bacterial contamination and thereby enhance food safety during processing. Of course, final selection of surface finishes would be influenced by function and economy. This research has shown that AFM is a rapid method to predict the potential resistance of a surface to bacterial contamination. Further analysis with AFM could enable a manufacturer to develop specifications for production with maximum and minimum tolerances for components at particular locations. In future work, the AFM might be used to determine the importance of bacterial morphology and chemistry for the pathogens associated with surface biofilms. To understand these processes will enable us to develop interventions that enhance plant sanitation and pathogen control.

References

Arnold JW: Development of bacterial biofilms during poultry processing. *Poult Avian Biol Rev* 9,1-9 (1998)

Arnold JW, Shimkets LJ: Cell surface properties correlated with cohesion in *Myxococcus xanthus*. *J Bacteriol* 170,5771-5777 (1988a)

Arnold JW, Shimkets LJ: Inhibition of cell-cell interactions in *Myxococcus xanthus* by Congo red. *J Bacteriol* 170,5765-5770 (1988b)

Medical Applications of SEM

Endothelial Toxicity of 5-Fluorouracil - Review

MAGDALENA CWIKIEL

Department of Oncology, University Hospital, Lund, Sweden

Introduction

Cardiotoxicity is a serious side effect of 5-Fluorouracil (5-FU) treatment of malignant diseases.[1] Its underlying pathophysiological mechanism remains unclear. One of the most common clinical manifestations of 5-FU induced cardiotoxicity is myocardial ischemia in different guises, which suggests that endothelium of coronary arteries could be involved in the pathophysiology of the syndrome.[2]

Due to the role of vascular endothelium in the regulation of vascular tone and regulatory mechanism of thrombogenicity, studies of this organ under the influence of 5-FU were performed. We continued with studies evaluating the possible protective effects of low molecular weight heparin dalteparin and antioxidant substance probucol in prevention of 5-FU effects on endothelium.

Methods

Three studies were performed. Totally, 45 rabbits were injected intra-arterially, using the central artery of one ear, with 5-FU (25 mg/kg). Fifteen of them were treated with dalteparin 100E/kg subcutanously one hour before the treatment and daily until they were sacrified just before perfusion fixation. Fifteen were treated with probucol 60mg/kg intraperitoneally (i.p.) 3 times per week under 2 weeks before start of 5-FU. Animals were sacrified just before perfusion fixation 1, 3, 7, 14 and 30 days after treatment with 5-FU. Fifty animals totally received no 5-FU treatment and served as controls. Local and systemic effects of 5-FU and 5-FU- dalteparin respective 5-FU-probucol were evaluated with scanning electron microscopy. The damage to the endothelium was evaluated using the score system described previously.[3]

Results

In an experimental study in rabbits, evaluating the immediate effect of 5-FU on vascular endothelium, severe damage to the intima, occasionally followed by thrombus formation was seen.[4] In further studies assessing the late effects of 5-FU on this structure 1, 3, 7, 14 and 30 days after treatment, more severe endothelial injury with an increased expression of thrombus formations was found. The effect of 5-FU was most pronounced about 3 days after commencing treatment, which corresponds well with the timing of clinical signs of cardiotoxicity. The endothelial injury was furthermore reversible with gradual normalisation within 30 days.[5]

The finding of a systemic toxic effect of 5-FU on vascular endothelium was also supported by the results from an in-vitro experiment where cultured endothelial cells were studied under the influence of 5-FU (6). The study showed a decrease in DNA synthesis and an increased release of prostacycline by endothelial cells during incubation with 5-FU, indicating the special susceptibility of benign endothelial cells to 5-FU.

The results from experimental studies taken together could be interpreted to mean that the primary reaction on endothelial injury by 5-FU is an increased release and leakage of vasodilatory anticoagulant substances. Only when this mechanism becomes exhausted does the procoagulant effect take over, expressing itself as thrombus formation.

Thrombogenic effect of 5-FU was protected by antithrombotic treatment with low dose heparin-dalteparin, although dalteparin *per se* seemed to have a toxic effect on endothelium, different from that of 5-FU (7).

In probucol treated animals, neither severe damage to the endothelium nor thrombus formation was seen.

Conclusions

These results support the hypothesis that 5-FU may cause non-lethal injury to benign endothelium, an unspecific toxicity that seems to be different from the anti-tumor effect of 5-FU. Such injury with the possible accompaniment of thrombogenicity could be one of the pathophysiological mechanisms behind vascular toxicity of 5-FU.

The study indicates the protective effect of dalteparin and probucol in prevention of 5-FU induced endothelial injury. The findings suggest also that free radical mediated mechanisms could be involved in 5-FU's toxic effect on the vascular endothelium.

References

1. Becker K, Erckenbrecht F, Häusing D, Frieling T. Cardiotoxicity of the antiproliferative compound fluorouracil. *Drugs* 1999; 57(4): 475–84.
2. Robben N, Pippas A, Moore J. The syndrome of 5-Fluorouracil Cardiotoxicity. *Cancer* 1993;71,493–509.
3. Wieslander JB, Stjernquist U. The influence of non-ionic contrast media on the endothelium of small arteries. Acta Radiologica Suppl 1987;370:73–77.
4. Cwikiel M, Zhang B, Eskilsson J, Wieslander JB, Albertsson M. The influence of 5-fluorouracil on the endothelium in small arteries. A scanning and transmission electron microscopic study in rabbits. *Scanning Microscopy* 1995;9:2:561–76.
5. Cwikiel M**,** Albertsson M, Eskilsson J, Stjernqvist U, Wieslander JB. The appearance of endothelium in small arteries after the treatment with 5-fluorouracil. An electron microscopic study of its late effects in rabbits. *Scanning Microscopy* 1996;10;3; 805–20.
6. Cwikiel M, Albertsson M, Eskilsson J, Stavenow L. The influence of 5-fluorouracil and methotrexate on vascular endothelium. An experimental study using endothelial cells in culture. *Annals of Oncology* 1996;7:731–7.
7. Kinhult S, Albertsson M, Cwikiel M, Eskilsson J. Pathophysiology of 5-fluorouracil induced cardiotoxicity. The role of antithrombotic treatment in protection of thrombogenic effects of 5-fluorouracil on vascular endothelium. *J Scanning Microscopy* 1999;21:105 (abstract)

Pathophysiology of 5-Fluorouracil-Induced Cardiotoxicity. The Role of Probucol Treatment in Protection of Toxic Effects of 5-Fluorouracil on Vascular Endothelium

SARA KINHULT,* MARIA ALBERTSSON,* JAN ESKILSSON,† MAGDALENA CWIKIEL*

*Department of Oncology, †Department of Cardiology, University Hospital, Lund, Sweden

Introduction

Cardiotoxicity is a serious side effect of 5-fluorouracil (5-FU) treatment of malignant diseases[1]. Its underlying pathophysiological mechanism remains unclear. Clinical data suggest that endothelium of coronary arteries could be involved in the pathophysiology of the syndrome[2].

The results from experimental studies indicate special susceptibility of the endothelium to 5-FU and support the hypothesis about a thrombogenic effect of 5-FU, secondary to its direct toxic effect on the endothelium, as one of the pathophysiological mechanisms behind 5-FU induced cardiotoxicity[3,4].

Probucol, a lipid-lowering drug with strong antioxidant properties has previously shown to provide complete protection against doxorubicin (a potent antitumour antibiotic) cardiomyopathy without interfering with its antitumour effect[5].

Free radical generation, during the treatment with 5-FU, leading to lipid peroxidation and cell membrane damage, could be one of the mechanisms behind 5-FU's toxic effect to the endothelium. In the present study we evaluated the possible role of probucol treatment in protection of toxic and thrombogenic effects of 5-FU on vascular endothelium in animal model in rabbits.

Methods

Thirty rabbits (fifteen in each group) were treated with probucol 60 mg/kg intraperitoneally (i.p.) 3 times per week under 2 weeks before start of 5-FU (25 mg/kg injected intra-arterially in a single dose) in half of the animals. The other fifteen animals received NaCl in the same way and served as controls. Animals were sacrified just before perfusion fixation 1, 3, 7, 14 and 30 days after treatment with 5-FU or NaCl. Local and systemic effects of 5-FU on the vascular endothelium after pre-treatment with probucol were evaluated with scanning electron microscopy. The damage to the endothelium was evaluated using the score system described previously[6] and compared to the damage caused by 5-FU alone[3].

Results

The study showed relatively mild damage to the endothelium in the probucol-treated groups. No intima disruption or denudation of underlying structures was present. Neither platelet accumulation or fibrin formation was seen. The serious damage seen in samples treated only with 5-FU, mostly pronounced on Days 3 and 7, was totally absent. Instead, the scores for both probucol groups were comparable in a group receiving only saline.

Conclusions

The study indicates protective effect of probucol in prevention of 5-FU induced endothelial injury. The findings suggest that free radical mediated mechanisms could be involved in the toxic effect of 5-FU on vascular endothelium.

References:

1.Robben FR, Pippas A, Moore J. The syndrome of 5-fluorouracil cardiotoxicity. Cancer 1993;71:493-509
2. Labianca R, Berreta G, Clerici M, Fraschini P, Luporini G. Cardiac toxicity of 5-fluoro-uracil: a study on 1083 patients. Tumori 1982;68:505-510
3. Cwikiel M, Eskilsson J, Wieslander JB, Stjernqvist U, Albertsson M. The appearance of endothelium in small arteries after the treatment with 5-fluorouracil. An electron microscopic study of its late effects in rabbits. Scanning Microscopy 1996;10(3):805-820
4. Cwikiel M, Albertsson M, Stavenow L. The influence of 5-fluorouracil and methotrexate on vascular endothelium. An experimental study using endothelial cells in culture. Annals of Oncology 1996;7:731-737
5.Siveski-Iliscovic N, Hill M, Chow DA, Singal PK. Probucol protects against adriamycin cardiomyopathy without interfering with its antitumour effect. Circulation 1995;91(1):10-15
6. Wieslander JB, Stjernqvist U. The influence of non-ionic contrast media on the endothelium of small arteries. Acta Radiologica Suppl 1987;370:73-77

Cell Death by Autoschizis for Bladder (T24) and Ovarian Carcinoma (MDAH) Cells: LM and SEM Aspects of Morphologic Changes Induced by the Synergistic Antitumor Activity of Vitamin C: Vitamin K_3 Combinations

J. GILLOTEAUX,* J.M. JAMISON,† D. ARNOLD,* V. VON GREUNIGEN,‡ R. HOWER,* H.S. TAPER¶, AND J.L. SUMMERS†

*Dept. Anatomy, Lake Erie College of Osteopathic Medicine, Erie, PA; †Dept. Urology, Summa Health System/NEOUCOM, Akron, OH; ‡Dept. Obstetrics and Gynecology, Akron General Hospital, Akron, OH; and ¶Dept. Biochemical Toxicology and Cancerology, Universite Catholique de Louvain, Brussels, Belgium.

Taper and collaborators[1] found that co-administration of vitamin C (VC) and vitamin K_3 (VK3) combination (in a VC/VK3 ratio of 100:1) to a variety of carcinoma cell lines resulted in equivalent antineoplastic activity at concentrations that were 10–50 times lower than when either vitamin was administered alone. Generation of peroxides followed by membrane lipid alteration[2], DNAs activation and RNA destruction[3] by the VC and VK_3 combination in the catalase-deficient cancer cells, were some of the cell responses resulting from the potentiation and specificity of the antitumor activity of these combined vitamins. The purpose of this report is to pursue the evaluation of VC, VK3, and the VC/VK3 combinations for their antitumor activity against human bladder (T24) and ovarian carcinoma (MDAH) cell lines, to document overall morphological changes, to compare these observations with LM and SEM, and to observe whether changes at the subcellular level correspond to previous findings. Following exposure of both tumor cell lines to each vitamin as well as the vitamin combination for 2h and 4h periods, samples were then processed for transmitted and fluorescence LM and SEM.

This study reports changes in nuclear and other intracellular changes, especially those related to actin patterns stained with fluorescein-phalloidin, and cell death, and to complement our previous descriptions of autoschizis. LM and SEM micrographs compare adherent T24 and detached MDAH cells with Sham T24 and MDAH. The Sham cells are strongly attached to their support and sometime overlap each other. The pleiomorphic cells appear squamous to spherical and ovoid in shape during mitotic activity. Their perikarya bulge from the flat cell surfaces during mitosis. Cells possess long and short lamellipodia and filopodia contacting neighboring cells. Following VC treatment, T24 and MDAH cells appear somewhat flattened and exhibit filopodia out of large distorted, droplet-like peripheral cytoplasms. The perikarya display elevated rings and surround nuclear areas. VK3-treated cells are flattened and show small areas of metachromatic cytoplasm cuts. The nucleoplasm is no longer euchromatic with an overall higher density. Chromatin becomes marginated, isolating a large segregated nucleolus. This damage is accompanied by the apparent collapse of some of the cell cytoskeleton and loss of DNA.

Combined vitamin treatment results in cells that maintain apparently intact nuclei, while extruding substantial pieces of organelle-free cytoplasm surrounded by actin networks. The treated cells still appear alive but are small and display broken nucleolus. A dispersed DNA is viewed by a weak Feulgen stain, while extranuclear DNA is detected. The remaining perikarya are surrounded by a narrow rim of cytoplasm containing only damaged organelles before karyorrhexis, final nuclear fragmentation, and cell death. Since this type of cell death does not agree with the morphologic characteristics of apoptosis or necrosis/oncosis, these findings confirm previous reports[4–5] and, at the same time, strongly suggest that this type of cell death, induced by oxidative stress, be called “autoschizis”; i.e., a cell death induced by loss of cytoplasm due to self morcellation[4–5].

Acknowledgement

This study was supported by Hess-Roth Kaminski and Maxon Urology Foundation of Erie, PA; Summa Health System Foundation, Akron, OH, and the American Institute for Cancer Research, Washington, D.C.

References

1. Noto V., Taper H.S., Yi-Hua J., Janssens J., Bonte J., Loecker W.D. Effects of sodium ascorbate (VitC) and methyl-1,4-naphtoquinone (Vit K_3) treatment on human tumor cell growth in vitro.Cancer 63: 901–906 (1989)
2. Venugopal M., Jamison, J.M., Gilloteaux, J., Koch, J.A., Summers, M., Giammar, D., Sowick, C. and Summers, J.L. Synergistic antitumor activity of vitamin C and K_3 on human urologic

tumor cell lines. Life Sci 59: 1389-1400.
3. Taper, H.S., J. M. Jamison, J. Gilloteaux, M. Venugopal, R. Hower and J.L Summers. Reactivation of DNases and RNase in trasnplanted human prostate carcinoma in nude mice as a result of a single injection of combined vitamin C and K_3 treatement . J. Histochem. Cytochem., submitted.
4. Gilloteaux, J., Jamison, J.M., Arnold, D., Ervin E., Eckroat L., Docherty J.-J., Neal, D., Summers, J.L. Cancer cell necrosis by autoschizis: Synergism of antitumor activity of vitaminC;:vitamin K_3 on human bladder carcinoma T24 cells. Scanning 20: 564–575 (1998)
5. Ervin E, Jamison J.M., Gilloteaux J, Docherty J.J., Jasso J. And Summers J.L. Characterization of the early events in vitamin C and K_3-induced death of human bladder tumor cells. Scanning, 20: 210–211 (1998).

Teaching Microscopic Anatomy and Histology with the Aid of SEM

UWE HILLER

Westfaelische Wilhelms-Universitaet, Institut für Anatomie, Muenster, Germany

As a part of preclinical studies our students have to pass an histology and microscopic anatomy course. The samples for light microscopy are obtained from a collection of mainly human tissue. This collection was established around 1960. As fixative a 10% formaldehyde, and as a storage liquid a 4% formaldehyde solution were used. The excision of human probes was performed in the clinical department shortly after the death of a patient.

We investigated the applicability of these probes for SEM-pictures in order to set up a series of SEM pictures corresponding to the light microscopic slide collection, which will help to improve the understanding of the subject matter by the students.

Samples of the collection were excised under a binocular microscope, and macerated where needed to demonstrate the various types of collagen fibres (Ohtani, 1992). After postfixation with 4% formaldehyde (one week) the samples were rinsed with water and dehydrated through a graded series of ethanols up to 100%. The duration of the steps depended on the shape of samples. In most cases, a post-preparation (micro-dissection and/or freeze fracture by liquid nitrogen) was performed after critical point drying with carbon dioxide to optimise the samples for teaching. Finally, the specimens were glued with conductive glue (Goecke, Muenster) using a Au/Pd-target. SEM-pictures were digitised and processed using various PC-programs.

As a general result we can demonstrate the applicability of the probes, at least within the same range of magnification achieved by the microscopes used by the students. However, for many samples such as the epithelial tissue of the respiratory, digestive or female reproductive system, the state of conservation was surprisingly good and allowed the use of even higher magnifications. This enabled the demonstration of kinocilia and striated muscle tissue on lower electron microscopic levels.

Poorly preserved tissues were observed in samples with low permeability for fixatives, such as testis, or samples with a high *post mortem* degradation rate such as stomach tissue. In these cases fixation by perfusion or directly fixed fresh animal tissue is preferred.

Acknowledgments

The author is very indebted to Mrs. Seidel for skilful technical assistance.

References

Ohtani O: The maceration technique in scanning electron microscopy of collagen fiber frameworks: First application in the study of human livers. Arch Histol 55(Suppl), 225-232 (1992)

Viper Venom Damage to Cell Surfaces Visualized by Scanning Electron Microscopy

J.F. GENNARO, JR., D.M. HUGHES-ELEK*

Department of Anatomy & Cell Biology, University of Florida Medical Center, Gainesville, Florida; *Laboratory of Cellular Biology New York University, New York, NY, USA

Viper venoms are extremely tissue damaging. They produce an effect, which is distinctive and exclusive to the venom of this type of snake. It may be that the ability these venoms have to disassociate cells within tissues from their extracellular matrices is primarily due to component arginine-glycine-aspartic acid (RGD) peptides called disintegrins.

Here scanning electron micrographs are presented to demonstrate the progressive action of venom from the cottonmouth moccasin (*Agkistrodon p. piscivorus)* on muscle and nerve tissue taken from the frog *(Rana pipiens*). Images show the complete removal of the extracellular matrix components (Collagens I & III) to, but not including, the plasma membranes of the muscle and nerve tissue.

The tissue employed in this study was the *M. cutaneous pectoris* from the frog (*R. pipiens*). This small muscle was dissected with the nerve intact from anesthetized frogs and pinned out in a small chamber on a silicone substrate. The muscle consists of a double thickness of small striated muscle fibers with the neuromuscular junctions, as is characteristic of the frog, situated on them longitudinally. Lyophilized venom from the cottonmouth moccasin was obtained from laboratory snakes milked into liquid nitrogen and then lyophilized. The incubation medium used was 112.4mM Na+, 2.5mM K+, 1.mM Ca2+, 117.1mM Cl–, and 3mM PIPES buffer (Piperizine-N,N′-bis-(2-ethane-

sulfonic acid). Venom treatment was in the same medium. Incubation was carried out at 24°C in a small glass chamber so the tissue could be observed through a light microscope. In most preparations concentrations of 10–50 µgs/ml. were used. After sufficient incubation in buffered venom, the tissue was washed by flooding with buffer. Fixation was carried out for 1 hour in 0.1M PIPES (ph6.7) and 3% glutaraldehyde because of the ability of this buffer to stabilize membranes. After fixation the tissue was washed briefly with the 0.1M PIPES buffer and 10% sucrose and prepared for scanning electron microscopy by dehydration and critical point drying. The dried tissue was mounted on aluminum specimen holders, covered with an evaporated gold film (10 nm) and observed in a JEOL SEM at 5kv.

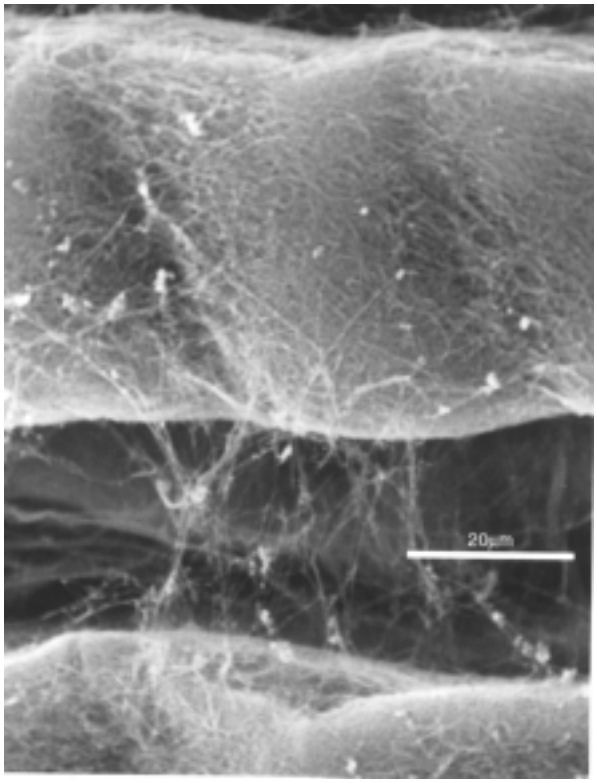

FIG. 1 A scanning electron micrograph of the frog muscle tissue after a preliminary incubation in dilute venom solution (8 minutes in 15µgs/ml.

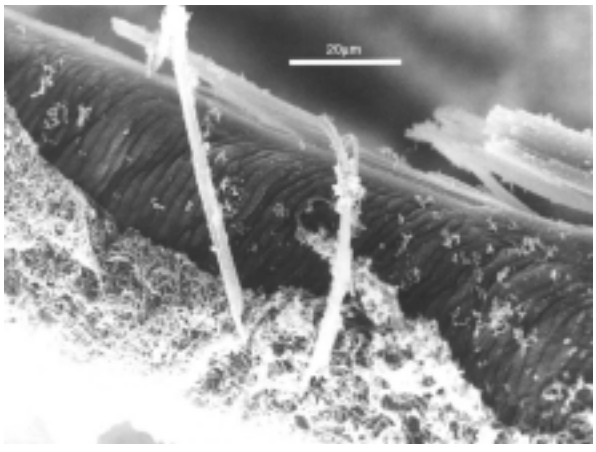

FIG. 2 Incubation for 13 minutes in a venom concentration of 15µgs/ml. removes all of the connective tissue coverings, not only of the muscle fiber, but also of the accompanying nerve.

Figure 1 shows a portion of the upper one of the two layers of striated musculature, which comprise M. cutaneous pectoris. The image is of a portion of two striated muscle cells with epimysium removed by action of the venom after 8 minutes of incubation at a concentration of 15 µg/ml. The fibrous nature of the peri- and endomysial connective tissue is visible. The fibrous shreds that extend between the muscle fibers are the remnants of the perimysium. These connective tissue fibers are composed primarily of Type I and Type III collagen. The dense mat of connective tissue seen beneath the fibers is the basement layer comprised of reticular and amorphous components in intimate contact with the plasma membrane of the muscle cells.

Incubation in the buffered dilute venom solution (15µgs/ml.) for 13 minutes (Figure 2) removes the long collagen fibers that comprise the three fascial sheaths and shears the surface of the cell cleanly. The extracellular material can be seen turned back as an intact blanket of short curly fibrous connective tissue material, probably a mixture of endomysial fibers and material from the reticular and amorphous basement membrane. Beneath them can be seen the bare sarcolemma, the plasma membrane of the muscle fiber, drawn up into ridges which define the limits of individual sarcomeres. In some preparations, openings, possibly the orifices of T-tubules, can be seen on the surface of the fiber. Nerve elements from the dissection can also be seen with the individual axons exposed. Bits and pieces of amorphous material can be seen adhering to the surfaces of the muscle and nerve cells. As in the case of the muscle tissue, the outer two connective tissue layers, epineurium and perineurium, have been removed although the association between the muscle and nerve elements does not seem to have been disturbed by the action of the venom. Individual nerve fibers, either unmyelinated or wrapped within a thin myelin sheath can be seen looping around the muscle cell.

Microscopy and Surface Science Applications For Electronic Semiconductor and Structural Materials

Microstructure of Gel-Grown, Impurity Stabilized Aragonite Spherulites

YOLANDE BERTA, DONOVAN HARRIS,* JAMES W. MCCAULEY*

School of Materials Science and Engineering, Georgia Institute of Technology, Atlanta, GA; *U.S. Army Research Lab, Weapons & Materials Research Directorate, APG, MD

Aragonite is a polymorph of $CaCO_3$, usually formed at high pressures. It adopts an orthorhombic symmetry and a higher density than (hexagonal) calcite, the stable phase at ambient temperature and pressure. Aragonite has biomedical applications, as a bone replacement material compatible with living tissue, and as biodegradable filler for paper and polymers. Thus, its formation and microstructure is of great interest.

In previous work[1], aragonite was formed under ambient conditions using a silica gel method in the presence of Sr and Mg impurity cations. The crystals formed were confirmed to be aragonite by examination, and characterized by light microscopy, which implied the presence of nuclei in the centers of the spherulites. Recently, fractured and whole spherulites formed by this method were evaluated using ESEM and dot-map EDS imaging. At the center of fractographically prepared spherulites were clearly imaged prismatic-shaped precipitates rich in Sr and Mg. In contrast to Wang *et al.*,[2] it is concluded that these regions act as the heterogeneous nucleation sites for spherulitic growth of aragonite needles, affecting their shape and formation.

References

1. J.W. McCauley and R. Roy, "Controlled Nucleation and Crystal Growth of Various CaCO3 Phases by the Silica Gel Technique," American Mineralogist, 59, 947–963, 1974.
2. L. Wang, I. Sondi, and E. Matijevic, "Preparation of Uniform Needle-Like Aragonite Particles by Homogeneous Precipitation," J. of Colloid and Interface Science, 218, 545–553, 1999.

The Microstructural, Microchemical, Dielectric, and Insulating Properties of Electroceramic Thin Films for Tunable Device Applications

M.W. COLE, P.C. JOSHI, M. ERVIN, M. WOOD

Army Research Laboratory, Aberdeen Proving Ground, MD

$Ba_{1-x}Sr_xTiO_3$ (BST) is a promising material for tunable microwave device applications such as electronically tunable mixers, delay lines, filters and phase shifters. The tunability of this material arises because it is possible to change its dielectric constant with application of an electric field. Bulk ceramic BST phase shifters, in a microstrip geometry, have been demonstrated at 5–10 GHz[1]. However, the relatively high loss tangent of these materials, especially at microwave frequencies, has precluded their use in phase shifter applications. Recently, the dielectric properties of these bulk materials have been improved; i.e., loss tangents were reduced to less than 0.006 at 10 GHz[2]. This reduction in loss tangent was achieved by the addition of MgO to form BST/MgO bulk ceramic composites. Utilization of these BST/MgO materials as phase shifting elements this bulk ceramic form (thickness >50 μm) is still quite limited due to the large voltages, on the order of 1000 V, needed to bias these bulk materials in a microstrip geometry[3]. However, fabrication of this BST/MgO based material in the thin film form reduces the needed bias voltages to less than 10 V, which is compatible with the voltage requirements of present semiconductor based systems. Additionally, the thin film material regime allows high frequency device operation, thereby enhancing the S/N ratio.

In this work we investigated the structural, compositional, insulating, and dielectric properties of $Ba_{1-x}Sr_xTiO_3$ thin films Mg doped 0 to 20 mol%. Films were fabricated via metalorganic decomposition (MOD) technique using barium acetate, strontium acetate, and titanium isopropoxide as precursors to form BST. Acetic acid and 2-methoxyethanol were used as solvents and magnesium methoxyethoxide was employed as the dopant. The precursor films were spin coated onto Pt-coated silicon substrates. Subsequent to coating, the films were pyrolized on a hot plate at 350˚C in order to evaporate solvents and organic addenda and form an inorganic film. The spin coat-pyrolization process was repeated until a film thickness of 500 nm was achieved. Post-deposition annealing was performed in an oxygen ambient at 750˚C. X-ray diffraction (XRD) was used to assess film crystallinity, phase formation and film orientation. Atomic force microscopy (AFM) and scanning electron microscopy (SEM) and were employed to access surface morphology and plan view grain formation. Cross-sectional transmission electron microscopy (X-TEM), combined with energy dispersive spectroscopy (EDS) analysis, was used to detail the film microstructure, film-substrate interfacial properties, and elemental diffusion. Rutherford backscattering spectrometry (RBS) was employed to access film stoichimetry. The electrical measurements were conducted in the metal-insulator-metal (MIM) capacitor configuration. Capacitance (Cp), dissipation factor (tan δ), and dielectric constant (ε_r) were measured with an HP 4192A impedance analyzer. The films insulating properties, leakage current (I_L), were evaluated via I-V measurements.

Our results demonstrated that the dielectric and insulating properties of BST based thin films were strongly dependent on film composition and microstructure. The dissipation factor, dielectric constant, tunability, leakage current, and grain size decreased with increasing Mg concentration.

The 0% and 5mol% Mg doped BST films were single phase solid solutions with a uniform dense granular microstructure, while the 20 mol% Mg doped BST films were multi-phased and compositionally non-uniform. Results of this investigation demonstrated that the dielectric properties of $Ba_{1-x}Sr_xTiO_3$ + 5 mol% Mg thin films showed an improved performance with respect to the 0 and 20 mol% doped BST films. Specifically, the 5% Mg doped BST films possessed low dielectric loss ($\tan\delta = 0.007$) with a dielectric constant of 386 and good tunability (12.7%) with an applied field of 100kV/cm.

References

1. W. Drach, T. Koscica, R.W. Babbitt, L. Sengupta, E. Ngo, S. Stowell and R. Lancto, Proc. of the 9th IEEE Symp. on Ferroelectrics, 79, 27–32, (1994).
2. L.C Sengupta, E. Ngo and J. Synowczynski, Integrated Ferroelectrics, 17, 287–293 (1997).
3. V.K. Varadan, D.K. Ghodgaonkar, V.V. Varadan, J.F. Kelly and P. Glikerdas, Microwave J., 35, 116–212 (1992).

Microscopic Characterization of Semiconductors

The Uniformity and Chemical Composition of CoSi Thin Film Characterized by Scanning Micro Raman Spectroscopy and Scanning Secondary Ion Imaging

EDUARDO DOZAL, TED NEIL, JIN ZHAO, LYNETTE BALLAST, CLIVE JONES AND TIM HOSSAIN

Process Characterization and Analysis Laboratory, Advanced Micro Devices, Austin, TX

Silicides are widely used on polycrystalline Si as low resistance gate electrodes and local interconnects. Among all silicides, $CoSi_2$ attracts a special interest, not only because of its low resistance and its technical advantages in processing, but also its excellent match with Si. In our laboratory, the phase formation sequence of the cobalt silicide system was characterized by X-ray photoelectron spectroscopy, where the formation of intermediate cobalt silicide phase — CoSi, in the conversion sequence of Co, to CoSi, to $CoSi_2$ was reported[1]. In another report[2], we have demonstrated that micro Raman spectroscopy can be used to determine the film thickness of CoSi. In the present work, we report the characterization of the CoSi thin film uniformity across a certain area using scanning micro Raman spectroscopy. The chemical composition information (major elements and doping elements) across the same area was obtained by scanning secondary ion imaging.

Micro Raman spectroscopy has been used for the non-destructive measurement of the absorption coefficient or the uniformity of thin silicide films on Si.[3, 4] The first-order Raman spectrum of crystalline Si is characterized by the presence of one peak corresponding to the Raman active phonon allowed by the Si crystal symmetry at 520.6 cm^{-1}. The Raman spectrum of CoSi thin film shows features around 204 and 220 cm^{-1}. The intensity of the Raman line due to the Si substrate covered by CoSi thin film is expressed as:[3]

$$I = I_o e^{-2\alpha d}, \quad (1)$$

$$\alpha d = -(1/2)\log(I/I_o), \quad (2)$$

where I_0 is the intensity of the Raman line measured in a reference bare Si film, α is the absorption coefficient of CoSi thin film, and d is the film thickness. The application of the Raman measurement for determining film thickness requires prior knowledge of the absorption coefficient α, which requires extensive experimental work. Nevertheless, the product αd alone gives information about the thickness and uniformity of the thin film. This is an efficient way to monitor film uniformity, although its value may be affected by reflection and dispersion effects in the thin film.

The Raman microprobe used in this work is a Renishaw System 2000. The spectrometer is coupled to a Leica INM200 microscope with 2.5, 20, 50, and 100× objectives. For these experiments, the 50× objective was used. The source is a Coherent Innova 70 argon ion laser tuned to 488 nm. With this configuration, the spot size is about 1μm and the sampling depth in bare silicon is on the order of 1000-2000 Å. The laser power at the sample was 6.0 mW and the acquisition time was 30 s. In the present work, the laser beam rastered cross the $150 \times 150\mu m$ analytical area, and a spectrum was collected at each point with a step width of 1μm. The resulting Raman spectra were then converted to the map of αd across the thin film.

Dynamic secondary ion mass spectrometry (DSIMS) offers extremely high sensitive quantitative elemental analysis with detection limits in the ppm-ppb range. Not only is this technique element specific, covering all elements from H to U, but it is also isotope specific. Lateral resolution of less than 1μm and depth profiling capability through a thick or thin film can easily be achieved. DSIMS can also be used to study the spatial variation of the secondary ion generated across a surface as well as with depth into the surface. In this means, ion imaging of DSIMS is an analogue of the scanning electron microscope. The primary ion beam is focussed to a fine spot and rastered over the surface of the specimen. The mass spectrometer output at a specific mass peak is then displayed in synchronism with the primary beam position to produce a map of secondary ion intensity across the surface with chemical composition information. The DSIMS analysis was carried out in a Cameca IMS-6f magnetic sector instrument. An $O2^+$ primary ion beam was used with beam current of 50nA and impact energy of 8 keV. The primary beam was rastered over the same square area analyzed by the scanning micro Raman spectroscopy. The beam diameter was 1~2μm. The

elemental specific maps of Co^+, Si^+, doping elemental signals with depth were recorded.

References

1. "Characterization of $CoSi_2$ formation by X-ray photoelectron spectroscopy", J. Zhao, C.M. Jones, and D.M. Poirier, J. Vac. Sci. Technol. B 17, 2570-2574 (1999).
2. "Effect of rapid thermal annealing temperature on the formation of CoSi studied by X-ray photoelectron spectroscopy and micro Raman spectroscopy", J. Zhao, L.K. Ballast, T.Z. Hossain, R.E. Trostel, and W.C. Bridgman, J. Vac. Sci. Technol. A, Proceeding issue of the 46th International Symposium of American Vacuum Society, in press.
3. "The use of TEM and Raman spectroscopy to determine the absorption coefficient and silicidation sequence of cobalt silicide", L. Weaver, M. Simard-Normandin, A. Naem, and A. Clark, *Mat. Res. Soc. Symp*., 260, 287-291 (1992).
4. "Non-destructive characterization of the uniformity of thin cobalt disilicide films by Raman microprobe measurements", A. Perez-Rodriguez, E. Roca, T. Jawhari, J.R. Morante, and R.J. Schreutelkamp, *Thin Solid Films*, 251, 45-50 (1994).

Effects of Substrate Orientation on Polytype Transformation in SIC: CCL-SEM Studying

E.N. MOKHOV, G.V. SAPARIN,* S.K. OBYDEN*

A.F. Ioffe Physical-Technical Institute, Russian Academy of Sciences, St. Petersburg, Russia; *Department of Physics, Moscow State University, Moscow, Russia

Silicon carbide is a wide band-gap semiconductor with very stable chemical bonding using for production of high-temperature, high frequency and high power diodes. SiC is known as a semiconductor belonging to a family of polytype materials having a different arrangement of atoms along one direction. Among them the polytypes 3C, 4H, 6H, 15R, 27R are very attractive. But reproducible growing of desirable SiC polytypes as single crystals and epilayers meets serious difficulties, as the mechanisms of polytype transformations are not clarified.

Nucleation probability and posterior growth of that or other polytypes depends on the nucleation conditions (growth temperature, stoichiometric deviations, impurity components and axial temperature gradient) as well as crystallographic orientation of substrate[1, 2]

In this report the compared growth of several important SiC polytypes (3C, 4H, 6H, 8H, 15R, 21R, 27R) on the substrates oriented by (0001)C and (0001)Si surfaces were investigated. Usually the substrates had the vicinal type surface with deflection angle no more than 30″ from (0001). The profiled surfaces with singular type fragments (artificial local surface singularization method) were also used.[3]

SiC layers were grown by the sublimation "sandwich method"[4] at the temperature 1750–2400°C in argon atmosphere or in vacuum.

The polytype structures have been studied by real color cathodoluminescence (CCL) mode in the scanning electron microscope (SEM). Electron beam energy varied[3,5] from 2 to 20 keV. The maximum penetration depth of electrons under 20 keV was 2,6 μm. Samples were doped by N and Ga during growth for effective luminescence. As the SiC polytypes have a different band gap than the luminescence spectrum, this informs us in some cases about polytype structure. For chosen activators, this CL-color varied from red (for 3C-SiC) to violet (for 4H-SiC).

Experimental data demonstrate that the polytype transformation probability as well as polytype structure can differ in overgrowth on polar {0001} surfaces. At that, the type of growth surface as well as a crystallization mode must be taken into account.

The highest stability of substrate polytype observed at the growth during molecular-kinetic mode at the vicinal surfaces close to (0001) surface. Such mode was realized at vacuum condensation at temperature $T_g < 2200$°C without impurities. In this case even rare polytypes (such as 4H and 21R) on surfaces (0001)C and (0001)Si were repeatedly grown with success.

At the growth of SiC-epilayers on the similar substrates in the diffusion mode (under pressure closed to the normal atmospheric one) the probability of stable polytype reproducing in general decreased. For most polytypes the transformation probability was higher on (0001)Si-substrates. A similar conclusion was drawn earlier[6]. That was associated with higher surface energy on (0001)C than on (0001)Si. Study of the growing surface morphology has shown that the growing steps density is higher on (0001)Si-faces, than on (0001)C surfaces. So, in accordance with theoretical analysis, occurrence of new nuclei for polytype transformation is preferable on (0001)C.

But in the diffusion growing mode on the (0001)Si-4H-SiC-substrate, 4H-polytype transformed into other polytypes, mainly into 6H-SiC. Under the same conditions on (0001)C-substrate 4H-polytype was grown stably. 4H-polytype changes were also observed on the surfaces. In this case, the transformation of 4H-polytype was not immediate. At first, the initial polytype 4H was kept with simultaneous occurrence of a terrace-like growing surface profile with macrosteps of growth. Then nuclei of other polytypes were formed onto terraces' steps and grew up. That was followed by the transformation of the substrate 4H-polytype into the others.

On the profiled substrates, formed of the separated outstanding platforms with a singular type of growing surface, the growing process differed from the one described above. The probability of polytype transformation on these surfaces in contrast to usual vicinal ones increased sharply. In case of the molecular-kinetic mode at growing temperature, $T_g < 1900$°C the cubic SiC-layers (3C-polytype) prevailed on both surfaces (0001)Si and (0001)C, except for the platforms with threading dislocations, which support keeping initial substrate polytype.

In the diffusion growing mode (T_g = 2000–2400°C) simultaneous growth of multiple polytype modifications

was observed on the singular platforms. Different polytypes grew in thin layers with thickness in the range from parts of microns to several microns. The same character of growth was observed in a case of minimum supersaturation in the growing zone (under temperature difference between the source and substrate less than 1°C). However, the polytype structure differed on the polar faces. Thus, on the singular surface (0001)Si 4H-polytype was practically absent. Moreover, 4H-polytype did not appear even after introduction of dopants furthering formation of 4H-polytype (i.e., isovalency dopants Sn or Ge).

On the singular (0001)Si face, even at $T_g > 2200$°C, the growing probability of cubic β-SiC appearance was high. This is a low-temperature polytype usually observed at $T_g < 1850$°C. More cubic polytypes (3C, 21R, 15R) prevailed on this surface in comparison with the (0001)C face. At the same time, more hexagonal polytypes (4H, 27R, 6H) grew on the singular (0001)C faces.

The model associates the probability of SiC-polytype nucleation with stoichiometric deviation. It is evident that (0001)Si face is concentrated by silicon, but (0001)C face has surplus carbon.

References

1. V.M.Tairov, V.F.Tsvetkov. Progress in controlling the growth of polytypic crystals. Progress in crystal growth and characterization. 1983, V.7, 111–162
2. R.A.Stein, P.Lanig, S.Leibenzeder. Influence of surface energy on the growth of 6H-SiC and 4H -SiC polytypes by sublimation. Mat.Sci.Eng.1992, B11, 1-4, 69–71.
3. E. N.Mokhov, A.D.Roenkov, G.V.Saparin, S.K.Obyden. Color cathodoluminescence - scanning electron microscopy study of the 4H-SiC heteroepitaxial layers grown by sublimation sandwich method - Scanning, 1996, v.18,N 3, p. 67–71
4. Yu.A.Vodakov, E.N.Mokhov, G.Ramm, A.D.Roenkov, Epitaxial Growth of SiC Layers by Sublimation Sandwich Method. 1. Growth Kinetic. Krist und Techn. 1979, v.14, N 6, p.729–740
5. G.V.Saparin, E.N.Mokhov, S.K.Obyden, A.D.Roenkov. Real color cathodoluminescence scanning electron microscopy—A new effective method for study of SiC materials and devices. Scanning, 1996, v.18,N 3, p. 25–34
6. Yu.A.Vodakov, E.N.Mokhov, A.D.Roenkov, A.D.Saidbekov Effect of Crystallographic Orientation on the Polytype Stabilization and Transformation of the Silicon Carbide. Phys.St.Sol.1979, v.51a, N 1 p.209–215

Surface Investigations on Al-free Laser Semiconductor Structure by Confocal Scanning Microscopy

G. A. STANCIU AND D. BOTEZ*

Department of Physics, University Politehnica of Bucharest; *Reed Center for Photonics, University of Wisconsin-Madison, USA

The broad-stripe, InGaAs-active diode lasers (λ= 0.89–1.06 μm) are used for pumping solid-state fiber lasers, frequency doubling, and for numerous medical applications. Al-free devices (i.e., In GaAs/InGaP/GaAs structures) have superior “wallplug” efficiency compared to conventional Al-containing devices due to their low differential series resistance[1].

Reported in the last years have been continuous-wave output powers, more than 10 W from 0.98-μm emitting In GaAs/InGaP/GaAs lasers.

One of the most important problems of the laser diodes is connected with the surface damage due to surrounding environment influence. For this reason, a good protection of the surface is necessary. The material that covers the surface devices may be a semiconductor having a band gap quite large in order to permit the laser beam exit the minimum loss.

The laser structure was previously presented.[2] The structure consists of two 70Å-thick $In_{0.2}Ga_{0.8}As$ quantum wells, a 1.3 μm–thick InGaAsP waveguide region, 1.0 μm-thick $In_{0.51}Ga_{0.49}P$ cladding layers, and a 0.2 μm-thick p^+_GaAs cap layer.

The device’s surface has been covered with ZnSe having a large band gap (2,6 eV). This band gap offered the possibility of device surface investigations using a confocal scanning laser microscope having an Ar laser (λ= 488 nm and 514 nm).

The technique used for investigation was the same as reported in a previous paper in connection with the characterization of a new semiconductor material with large band gap.[3]

By using reflection and photoluminescence techniques, we obtained images of the ZnSe-devices surface. Photoluminescence obtained with Ar laser beam having wavelength 488 nm is shown to be a better technique for this kind of study.

The laser beam induced current (LBIC) technique has been used to establish functionality of the laser diodes, as well as junction position before packaging.

Results of the present study indicate the influence of the ZnSe layer on the device’s surface and offer the opportunity to analyze it before covering with ZnSe.

References

1. Botez D, Mawst L, Bhattacharya A, Lopez J, Li J, Kuech TF, Iakovlev VP, Suruceanu GI, Caliman A and Syrbu, AV 66% CW wallplug efficiency from Al-free 980 μm- emitting diode lasers, Electron Lett. 32, 2012-2014 (1996)
2. Al-Muhana A, Mawst LJ, and Botez D, Garbuzov DZ, Martinelli RU, Connolly JC, High-power (>10 W) continuous-wave operation from 100-μm-aperture 0.97-μm-emitting Al-free diode lasers, Appl. Phys, Lett., 73, 1182-1184(1998)
3. Stanciu GA, Oprica MH, Oud JL, Daviti M, Paraskevopoulos KM, Polychroniadis EK,Growth and characterisation of $HgBr_2$ crystals using confocal laser scanning microscopy, optical spectroscopy and DC conductivity measurements, Journal of Physics D: Applied Physics, 32, 1928-1933 (1999)

Application of Composite Contrast SEM-Mode to the Study of Defects in InGaN/AlGaN/GaN-Heterostructures

S.K. OBYDEN, G.V. SAPARIN, P.V. IVANNIKOV, A.E. YUNOVICH, M. LEROUX,* S. DALMASSO,* G. BEAMONT,* M.V. LOMONOSOV

Moscow State University, Department of Physics, Leninskie Gory, Moscow, Russia; *Centre de Reshershe sur l'Heteroepitaxie et ses Applications, Sophia Antipolis, Rue Bernard Gregory, Vallbonne, France

GaN epitaxial films and InGaN/AlGaN/GaN-heterostructures grown by metal-organic chemical vapor deposition (MOCVD) technique were studied by real color cathodoluminescence method (CCL) in the scanning electron microscope (SEM). Luminescent properties of heterostructures critically depend on various growth steps of MOCVD-process. That is why it is necessary to use various methods to characterize grown structures from different points of view. One of the effective methods of structure characterization is the use of the SEM in the CCL-mode of operation (Saparin and Obyden 1988). Recently this method was applied to study defects in InGaN/AlGaN/GaN structures grown by MOCVD-technique with lateral overgrowth steps (Freitas *et al.* 1998).

The acquisition and storage of additional SEM-signals, such as secondary electrons (SE), backscattered electrons (BSE) and induced current (IC) give additional possibilities for sample analysis. Combination of different SEM-modes data into one color image of composite contrast (Obyden *et al.* 1997) allows one to reveal the spatial correlation between the specimen topography, location of electrical potential barriers and CL-centers distribution.

Variation of the accelerating voltage gives the possibility to estimate the thickness of the layers and recognize the peculiarities of the structures located under the surface.

We have compared two samples differing by the thickness of $Al_{1-x}Ga_xN$ (x=0.05-0.1) layers (100 and 200 nm in our case) and by Si-doping of InGaN-layer in the second structure. Grain boundaries (dislocation walls or cracks) and pin-hole defects are revealed by CCL-technique as dark lines and dots with a much greater contrast than that in SE-mode. But images of composite contrast taken as combination of color CCL-signal and achromatic SE-signal reveal both the defects distribution and the topography of an object. These dark lines are formed either during the growth (due to dislocation walls formation caused by lattice mismatch between the layers of heterostructures) or during cooling of the structures from growth to room temperature (due to cracks of the layers). Density of grain boundaries (cracks) critically depends on the thickness of AlGaN-layers and can be substantially decreased by adjusting time and temperature of epitaxial growth. Nonuniformities of the blue emission of n-GaN:Si-base layer have dimensions of 2–4 μm. Widths of dark lines in CCL-views (of 5–10 μm) are determined by defect areas as impurity-defect atmosphere around dislocations.

There are circular dark regions of 40–50 μm in diameter around pin-hole defects, which also may be described due to defect areas. Both types of defects influence quantum efficiency of LEDs produced on these structures. It is to be noted that there are more pin-holes in the region where dark lines concentration is lower. These defects were compared with similar pin-holes on the GaN-film grown by EMCORE laboratories. There were no dark lines on the picture, but the density of pin-hole defects and the size of dark circles around them is higher. We may conclude that there are some microscopic defects in GaN-lattice, which have a tendency to be adsorbed on macroscopic defects: grain boundaries, pin-holes or dislocations.

The comparative SEM-images of LED-structures taken in CCL, IC as well as in CCL+IC composite contrast modes have shown strong correlation between the variation of CL-intensity and the fluctuation of IC-signal. The dark lines in IC-view indicate that the defect region around grain boundary acts as a shunting path through the p-n-junction. We may conclude that high leakage current (tunnel mechanism) and low quantum efficiency at low voltages may be caused by such defect regions in some LEDs produced on these or similar structures. These regions have a small area and should be saturated at high currents and voltages. So, we may understand why such defect regions do not very much lower the quantum efficiency at higher voltages, while the current is injected over the whole p-n junction area.

We have measured over IC-image the mean statistical value of the relative IC-fluctuations $\Delta J/J \sim (3–3.5)10^{-2}$. These measurements can be used for evaluation of potential fluctuations in the InGaN/AlGaN/GaN p-n heterojuction. If a value of contact potential φ_c is of the order of InGaN energy gap (E_g = 2.4 eV) and $\Delta\varphi/\varphi_c \leq \Delta J/J$ then $\Delta\varphi$ < 70 meV. This evaluation may be compared with the parameter E_0 describing the long-wave exponent tail in the electroluminescence spectra of InGaN/AlGaN/GaN-based LEDs (Yunovich *et al.* 1999). A physical meaning of this parameter is interpreted as a measure of potential fluctuations in the active region of the heterostructure: $E_0 = 55 \div 60$ meV. It may be concluded that SEM study of luminescence and induced current gives evidence of such an interpretation of E_0.

In all samples we observed two spectral bands: blue CL-emission corresponded to the base GaN:Si-layers and wide yellow band were associated with recombination of donor-acceptor pairs on the dopants and native defects of GaN-layers. Varying diameter of the electron beam, we could see the changes of colors on CCL-images from yellow (for low excitation level) to blue (for high excitation level). This is indicated on the saturation of yellow band under high injection.

References

Saparin GV, Obyden SK: Colour Display of Videoinformation in Scanning Electron Microscopy: Principles and Applications to Physics, Soil Science, Biology and Medicine. *Scanning* 10, pp. 87–106 (1988)

Obyden SK, Ivannikov PV, Saparin GV: Color Cathodoluminescence Display in the Scanning Electron Microscope of Deep Relief Surfaces. *Scanning* 19, pp. 533–540 (1997)

Freitas JA Jr., Ok-Hyun Nam, Davis RF, Saparin GV, Obyden SK: Optical characterization of lateral epitaxial overgrown GaN layers. *Appl. Phys. Lett.* 72, 23, pp. 2990–2992 (1998)

Yunovich AE, Kudryashov VE, Mamakin SS, Turkin AN, Kovalev AN, Manyakhin FI: Spectra and quantum efficiency of light emitting diodes based on GaN heterostructures with quantum wells. *Phys. Stat. Sol. (a)*, v. 176, N 1, pp. 125-131 (1999).

Posters

Measurement Technique for Incident Secondary Electron Current in Secondary Electron Detectors

TOSHIHIDE AGEMURA, SATORU FUKUHARA, HIDEO TODOKORO

Beam Technology Center, Instruments, Hitachi, Ltd., Hitachinaka, Ibaraki, Japan

Introduction

The signal to noise ratio (SNR) is a key parameter to evaluate images from scanning electron microscopes (SEMs). A measurement method for SNR values determined by the ratio of a mean value to a standard deviation of the intensity distribution (or histogram) for a digital SEM image was proposed by Joy *et al.*[1] The SNR values of the SEM images depend strongly on both performance of the secondary electron (SE) detector and geometric SE collection efficiency.

The present report proposes a measurement technique for incident SE current in SE detectors based on SNR values.

Experimental Details

The SEM system is a Hitachi S-4500 SEM, with a specially adopted Schottky emission gun. The S-4500 SEM consists of two SE detectors, i.e., the through-the-lens Everhart-Thornly detector (upper detector) and the Everhart-Thornly detector (lower detector) set on the specimen chamber wall. The experimental procedures are as follows.

1. The accelerating voltage is set at –10 kV and the probe current is measured using a picoammeter.

2. A polished aluminum plate 100 mm in diameter is set on the sample holder and inclined at 45 degrees so as to reflect the primary electrons (PEs) to the lower detector.

3. The retarding voltage corresponding to the accelerating voltage is applied to the plate.

4. The magnification is adjusted so as to restrict the PE scanning area within the top surface of the lower detector; i.e. a scintillator. Since PEs are directly incident on the SE detector, the post voltage (normally +10 kV) for extracting SEs does not need to be applied.

5. One SEM image (512×512 pixels) integrated over 16 frames is acquired at a TV scan rate (0.03 s per frame). In order to measure the SNR value accurately, care is required with two points: the zero-DC offset adjustment (brightness) of the analogue-digital converter (ADC) input when PEs are cut off, and the optimum gain control of the photomultiplier (contrast) so as not to saturate pulses at the ADC input when PEs are irradiated.

6. The same procedures are repeated for the various probe currents.

7. The SNR values are calculated using mean signal intensities and standard deviations of the digital images recorded at each probe current.

Results and Discussion

Figure 1 shows the log-log plot and the approximate curve of SNR vs. PE current in the SE detector. The curve tangent of 0.50 satisfies the well-known relation that the SNR values are proportional to the square root of the PE currents. The coefficient of 5.30 depends on both bandwidth of the SE detection system[2] and the dwell time per pixel, which are related to each other. This means that the detection system consisting of the detectors and signal processing circuits has noise components which affect the SNR. Then the performance of the SE detection systems is evaluated using the SNR values.

Next, the geometric SE collection efficiency is considered. It is defined by the ratio of the SE current coming into the SE detector to the SE current emitted from the sample. With respect to the former current, the SNR value of the SE image obtained from a featureless sample (e.g., silicon wafer) is converted into a corresponding incident current in the SE detector using the curve shown in Fig.1. It is, therefore, not necessary to use electron counting instruments at all. The ratio of incident SE current to probe current is a product of the collection efficiency and the SE yield depending on the incident electron energy and sample and vacuum conditions. If the SE yield is known from the literature or measurements, the collection efficiency can be calculated. Or if, the collection efficiency is well known by means of the simulation of SE trajectories, the SE yield can be obtained. The relation shown in Fig.1 is very useful for evaluating these factors.

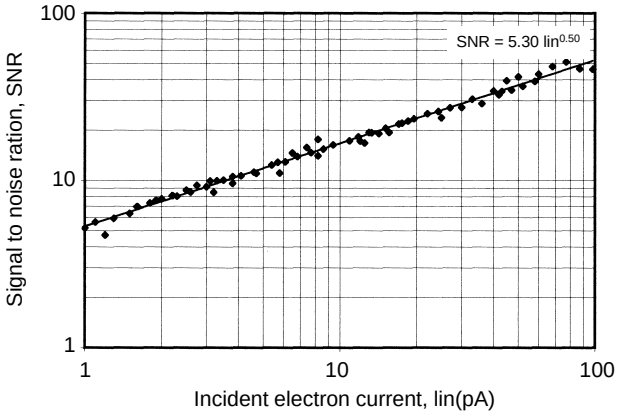

FIG.1 The log-log plot and the approximate curve of SNR vs. incident electron current. Digital images were recorded under the conditions of a TV scan rate (0.03 s per 512×512 pixel frame) and 16-frame integration.

Conclusions

The curve of SNR vs. incident electron current allows the performance of SE detectors to be evaluated and the absolute geometric SE efficiency and SE yield to be measured.

References

1. D. C. Joy, C. S. Joy, R. D. Bunn: Measuring the performance of scanning electron microscope detectors. *Scanning* 18, 1–18 (1996)
2. W. Shockley, J. R. Pierce: A theory of noise for electron multipliers. *Proc. Inst. Radio Eng.* 26, 321–332 (1938)

Determination of the Root Cause of Structural Changes in Sputtered Aluminum Films by AFM: A Case History

D.R. BRYAN, C.M. VICROY, J.H. LINN

Intersil Corporation, Palm Bay, FL

During routine monitoring of aluminum reflectivity prior to photoresist processing, a gradual increase in reflectivity was noted from aluminum films deposited in a particular deposition tool. Films of identical composition deposited in other metal deposition tools did not show the same change. Thickness measurements derived from historical resistivity values showed the high reflectivity films to be thin. However, scanning electron microscopy (SEM) cross sections of these films showed the actual film thickness had not changed. Therefore, the resistivity of these high reflectivity films had also changed.

Maintaining consistent microstructure is imperative for photoresist processing and metal electromigration performance. SEM and atomic force microscopy (AFM) were used to examine both the normal and high reflectivity films. A distinct change in grain size and surface texture was noted. The high reflectivity films had a much smaller grain size. The overall surface roughness (R_q) was also noticeably less on the high reflectivity films.

These structural changes in the aluminum films could be attributed to many deposition tool issues. These include vacuum leaks, contaminants incorporated in the film, changes in the oxide under the aluminum, target composition, and film deposition parameters. The target composition was confirmed to be correct. Residual gas analysis of the deposition tool showed no vacuum leaks. Secondary ion mass spectroscopy showed no significant differences in the oxygen and carbon levels between the normal and high reflectivity films. The tool deposition parameters, including pressure and power, were confirmed to be correct. The wafer temperature designated in the deposition recipe was also checked. Further investigation of the deposition tool found that the argon gas pressure valve, which is used to supply argon to transfer heat to the wafer from the heating block, was not opening completely due to a bad solenoid. A faulty valve could cause the argon pressure at the heater block to be much lower than normal. This suggested that the wafer temperature during the aluminum deposition was lower than expected. The analytical data supported this hypothesis, as films deposited at lower temperatures generally have smaller grain sizes and smoother microstructure.

In order to prove the root cause of the changes in the films and to ascertain the actual deposition temperature of the high reflectivity films, a designed experiment (DOE) was run after the valve was replaced. Aluminum films were deposited in the repaired tool and in one of the tools producing films with nominal reflectivity and microstructure. The argon flow factors were normal flow and no flow. Three different wafer deposition temperature recipes, 250°C, 350°C and 420°C were used. AFM was used to compare the grain size, microstructure and overall surface roughness of these films.

The films deposited with normal argon flow from both the repaired tool and the control tool exhibited nominal reflectivity, thickness, grain size and texture for a given deposition temperature. The AFM data did indicate that the grain size and texture were slightly greater on films from the control deposition tool. This suggested that these films were deposited at slightly higher temperatures compared to the repaired tool. Films deposited with no argon flow exhibited reflectivity values more analogous to films deposited at substantially lower temperatures with normal argon flow. The AFM data confirmed this observation: Films deposited at a recipe setting of 420°C, no argon flow had grain size and microstructure similar to films deposited at 350°C, normal argon flow. The 350°C, no argon flow films were similar in structure to the 250°C, normal argon flow films. The AFM data from the original films deposited during the timeframe with the argon valve problem had reflectivity and microstructure similar to films deposited at a temperature of about 100°C lower than expected.

The AFM data confirmed that the reduced argon flow was the root cause for the increased reflectivity, smaller grain size and increased resistivity. When the valve was repaired and the argon flow set to normal, the films returned to their nominal reflectivity, microstructure, and resistivity for a given deposition temperature. The AFM data from the DOE wafers allowed for the unambiguous determination of the root cause of the film structure changes and the corresponding corrective action.

Investigation of Foreign Substances in Food

JAMES E. CHARBONNEAU, PH.D.

National Food Processors Association, Washington, DC

Foreign substances in food can present problems for the food industry. At the very least they cause consumer complaints which can harm a company's reputation and brand name, and if foreign objects product tampering leads to a product recall an entire business can be ruined and this can affect the credibility of the entire food industry.

A foreign substance can be any material allegedly found in food that is not part of the product formulation, and may take the form of mold, bone, fruit pits, herbaceous stems, rocks, insects, and other animals, wood, paper, oil and grease, dirt and soil, drugs, plastics, metal and glass.

The objective of a foreign substance exam is to identify the object, the probable sources and, if possible, whether the foreign object was in the product when it was processed.

An Amray 1600 T Scanning Electron Microscope (SEM) together with a Kevex Sigma 2 Energy Dispersive Spectrometer System and/or a Nicolet Magna 560 Fourier Transform Infrared(FTIR) spectrometer/ Nicplan microscope was used to investigate foreign substances from 7 categories of foreign substances in food.

Naturally Occurring Foreign Substances. These are substances that are part of the unprocessed food that may have inadvertently gotten through the system. They may include fruit pits, animal skin and fur, or other objects closely associated with the food product prior to processing. Using FTIR, a foreign substance was identified as a natural resin probably from the product.

Foreign Substances Introduced During Food Processing. Occasionally materials such as grease, metals, paint or other objects associated with the packing process inadvertently enter the product. Using SEM-EDS, foreign material found on surf clams was identified as calcium phosphate from a product/ingredient interaction. Using SEM-EDS, a crystalline material in a meat product thought to be bone was identified as calcium salts of chloride and phosphate. Using FTIR, foreign material that clogged an aerosol valve was identified as chipboard. Using SEM-EDS, the metal in the heel of a glass bottle was identified as copper sulfide-containing metal inclusion.

Insects, Reptiles and Rodents. Using SEM-EDS, a mouse found in food was determined to be unprocessed based on the presence of collagen fibers on the surface of the mouse foreleg tissue.

Glass Fragments. Using SEM-EDS, glass from various sources can be distinguished from one another either by the level of the major elements in glass or by the presence of elements in one glass, but not in another.

Glass-like Particles. Using SEM-EDS, glass-like particles found on beets were determined to be a fatty acid similar to myristic acid.

Metal Foreign Objects. Using SEM-EDS, metals from a variety of sources can be easily distinguished. For example, a tin soldered container can be distinguished from a lead soldered can. Using SEM-EDS, the source of a metal fiber found on the bottom of a 2-piece can was determined to be from the container coating operation.

Drug Capsule Identification. Using FTIR, a pill found in food was identified as ibuprofen.

Many types of technology are available to the food processor to prevent foreign objects from entering the food product. These include magnets, sieves, screens, gravity separators, and metal x-ray detectors. In the event that foreign substance contamination is suspected, x-ray based systems are available to screen the food product. Analytical methodologies such as SEM-EDS and FTIR are excellent techniques to identify and to help track the source of foreign materials in food.

Is There a Chemical Interaction Between Calcium Phosphates and Organic Compounds in the Inorganic-organic Composites?

ELENA I. DOROZHKINA, SERGEY V. DOROZHKIN*

*Research Institute of Fertilizers, Kudrinskaya sq. 1 – 155, 123242 Moscow D-242, Russia

Introduction

Composites of calcium phosphates with organic and/or biological compounds are promising materials for artificial bone substitutes. In such composites calcium phosphates simulate an inorganic part of bones, while organic and biological compounds are added to improve mechanical properties and biocompatibility. In spite of the many paper published in this field, the question whether there is a chemical interaction between calcium phosphates and organic/biological compounds in such composites currently remains unclear.

Materials and Methods

Dicalcium phosphate dihydrate, calcium deficient apatite, hydroxyapatite, and tricalcium phosphate were studied. Powders of these calcium phosphates were mixed

with powders of water-soluble cellulose ethers (1 : 1 by weight), put into bottles contained some amount of water. The bottles were sealed and kept heated at temperatures of 130 °C during 48 hours. After that the bottles were opened and kept heated at 90 °C during 24 hours for water evaporation. Chemical and structural analyses of the dry composites obtained were studied with SEM, FTIR and XRD.

Results

In SEM observations (secondary electrons mode) the composites looked like crystals of calcium phosphates embedded into a matrix of the cellulose ethers. Neither dissolution/precipitation nor recrystallization phenomena were found. Results on FTIR investigations of the dry composites revealed a superposition of the bands of cellulose ethers with those of calcium phosphates. No new absorption bands were found in spectra of the composites, if compared with those of initial compounds. Similarly, XRD diffraction revealed no new peaks in diffraction patterns of the composites if compared with those of pure calcium phosphates.

Discussion and Conclusions

Absence of any new diffraction peaks and absorption bands on XRD patterns and FTIR spectra respectively points out the absence of a chemical interaction between inorganic and organic compounds in the composites studied. Results on SEM investigations appear to be in support of this conclusion, because no newly formed crystals were found in the dry composites. Careful analysis of references has confirmed the above conclusion: no chemical interaction between calcium phosphates and organic or biological compounds has ever been found unless special preparations of organic phase (e.g., cellulose phosphorylation) were made.

Localization and Quantification of Z-RNA in Eye Lens Central Zone Epithelium

C.E. GAGNA,*†‡ H.-R. KUO,† J.A.E. REGA,‡ J. HEINZE,* W.C. LAMBERT†

*Department of Life Sciences, New York Institute of Technology, Old Westbury, NY; †Department of Pathology and Laboratory Medicine, University of Medicine and Dentistry of New Jersey-Medical School, Newark, NJ; ‡Department of Biology, Fairleigh Dickinson University, Teaneck-Hackensack Campus, Teaneck, NJ, USA

Our group has characterized the distribution of left-handed Z-RNA sequences within the area of lens epithelium known as the central zone (CZ). Right-handed B-DNA conformation has the ability to convert into the left-handed Z-DNA configuration *in vitro* under high salt (4M NaCl).[1] Right-handed A-RNA can be converted into left-handed Z-RNA under specific chemical conditions,[2] and Z-RNA has been identified in human cells.[3] Very strong evidence supports the existence of left-handed Z-DNA *in vivo*.[4] Removal of proteins by fixatives can induce supercoiling which stabilizes Z-DNA and Z-RNA sequences.[3,4]

Anti-Z-RNA polyclonal IgG antibodies were produced in rabbits immunized with multiple injections of purified Z-RNA: brominated-poly[ribosomal(G-C)]. The anti-Z-RNA polyclonal antibodies were purified and characterized as described by Zarling *et al.*[3] All normal (noncataractous) dog lenses were isolated from male and female coonhounds 1.5 years old. For immunohistochemistry (light microscopy), lens tissues were fixed in Carnoy's solution, embedded in paraffin and sectioned 2.0μm thick. Carnoy's solution is an alcohol fixative which removes non-chromosomal proteins and DNA binding proteins allowing for the formation of Z-helical type nucleic acids.[4,5] Quantification of the Z-RNA antigenic tissue binding sites were accomplished by the use of the avidin-biotin-peroxidase (ABP) immunohistochemical staining system.[5] The staining intensities of ABP reaction products were measured by analyzing serial tissue cross sections (Fig. 1). The arrangement of ocular lens fiber cells in successive lamellae dictates that in the cross-sections examined, the long axis of the fiber cell is parallel to the plane of each tissue section. Therefore, the orientation of each cell nucleus was parallel to the plane of the section. Computerized image analysis of CZ nuclear morphology and CZ immunohistochemistry was accomplished using a Leitz DM-RB microscope and Leica Quantimet 500+ image analyzing system (200x mag.)

For electron microscopy (EM) studies, pieces of CZ epithelium were fixed with 5% glutaraldehyde and post-fixed with 1% osmium tetroxide.[6] This was followed by dehydration with a series of ethanol solutions, and embedding of the epithelium in Epon 812. Remaining techniques were conventional procedures employed in immunoelectron microscopy (immunogold).[6] The Jeol 1200 EX electron microscope was employed for all studies.[6]

Light microscopy (immunohistochemical) studies revealed ABP staining patterns within the CZ (Fig. 1) epithelium (Fig. 2). Higher immunohistochemical staining intensity was quantified in the CZ epithelium nearest the preequatorial zone (PZ) (Fig. 1), and much lower immunostaining intensity was measured in the centermost (apical) region of the CZ epithelium. We believe that the CZ epithelium nearest the PZ is more active in ocular lens protein synthesis.[7] Our group speculates that the CZ epithelium nearest the PZ epithelium is in the process of re-entering the cell cycle, hence our observation of increased Z-RNA antibody binding. Conversely, Z-RNA immunohistochemistry within the central most part of the CZ epithelial cells reveals very low Z-RNA antibody binding. EM results demonstrate that the ribosomal (r-)Z-RNA binding sites are located within the nucleolus and cytoplasm of CZ epithe-

lium. Therefore, we speculate that r-Z-RNA within the CZ epithelial cells is either not present in large amounts, unaccessible due to condensation of nucleic acids, or covered by proteins.

CZ epithelial cells have withdrawn from the cell cycle and exist in a G_0 state (G_1 period). The epithelial cells in the germinative zone (GZ) synthesize DNA, divide, line up in meridional rows (MR) and produce differentiating cells (DC) which transform into secondary nucleated ocular lens fiber cells (Fig. 1). The secondary fiber cells (SF, MF and DF: Fig. 1) undergo a specialized form of cell death, terminal differentiation (denucleation), as they are displaced from the lens' outer cortical area to its nucleus region. Consequently, the CZ epithelial cells may contain Z-RNA sequences which are not active in protein synthesis (translation).

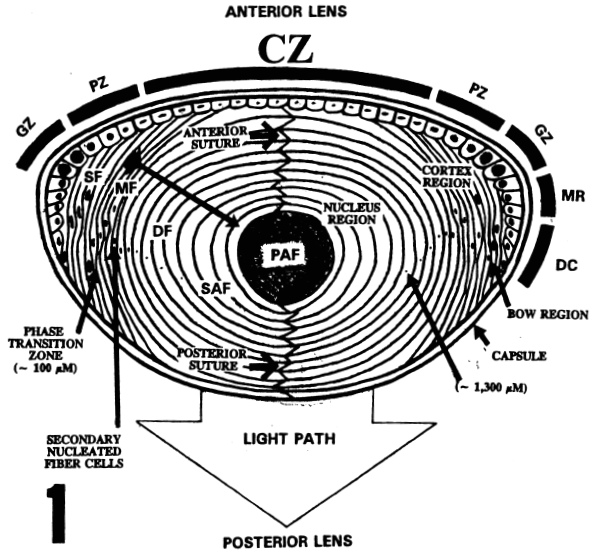

FIG.1 Cross section (schematic diagram) of the normal (noncataractous) adult ocular lens defining histology, molecular biology and supramolecular order:epithelial cells [central zone(CZ), preequatorial zone(PZ), germinative zone(GZ), meridional rows(MR), and differentiating cells(DC)], bow region (equator), the superficial fibers(SF), phase transition zone(PTZ), middle fibers (MF), deep fibers(DF), secondary anucleated fiber cells(SAF), primary anucleated fiber cells(PAF) and the last denucleating fiber cell at a depth of about 1,300µm. Arrow going from the cortex region to the nucleus region indicates direction of the displacement of lens fiber cells.

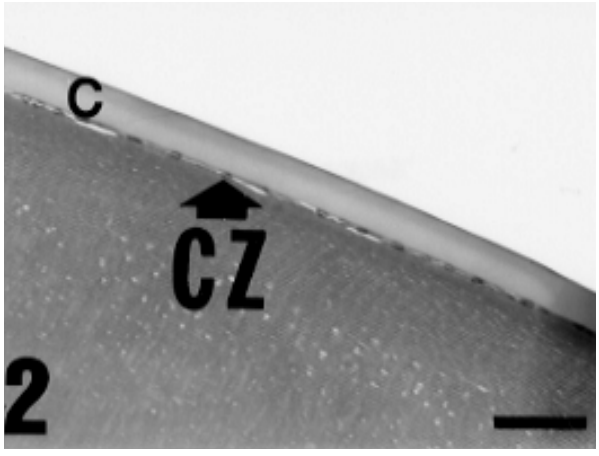

FIG.2 Photograph of the Z-RNA immunohistochemistry of the normal dog lens revealing the central zone(CZ) epithelium. This particular photo reveals 18 stained cells. Capsule = C,H&E counterstained (Bar = 50 µm).

Understanding the physiology, biochemistry and molecular biology of the normal adult ocular lens is critical in order for us to better comprehend the supramolecular order and metabolism of cataractogenesis. Presently, the exact mechanisms which initiate cataract formation in the human lens are poorly understood.

Z-DNA has been identified in the dog lens,[5] and Z-RNA has been localized in the lens' superficial fibers (SF)[8] and epithelium [GZ[9], DC[10] and PZ[11]]. Taken together with the data presented here, this suggests that Z-DNA and Z-RNA may play a role in controlling the molecular biology of the normal adult lens. Based on our present and past data, and the literature on Z-RNA,[3,8,9,10,11] we speculate that the *in vivo* lens r-RNA may be covered by Z-RNA binding proteins, mainly in the A-RNA configuration or highly condensed as part of the G_o states exit from the cell cycle.

References

1. Rich A: Speculation on the biological roles of left-handed Z-DNA. *Ann NY Acad Sc* 726, 1-16(1994)
2. Hall K, Cruz P, Tinoco I, Jovin TM, Vande Sande JH:Z-RNA-A left-handed RNA double helix. *Nature* 311, 584-586(1984)
3. Zarling DA, Calhoun CJ, Feurerstein BG, Sena EP:Cytoplasmic microinjection of immunoglobulin Gs recognizing RNA helices inhibits human cell growth. *J Mol Biol* 211, 147-160(1990)
4. Sinden R(Ed.):Left-handed Z-DNA. In *DNA Structure & Function*. Academic Press, New York (1994)179-216
5. Gagna CE, Lambert WC, Kuo H-R, Farnsworth PN:Localization of B-DNA and Z-DNA in terminally differentiating fiber cells in the adult lens. *J Histochem Cytochem* 45, 1511-1521(1997)
6. Hyatt AD:Immunogold labeling techniques. In *Electron Microscopyin Biology:A Practical Approach* (Ed. Harris JR). IRL Press, Oxford (1991)59-81
7. Papaconstantinou J:Molecular aspects of lens cell differentiation. *Science* 156, 338-346(1967)
8. Gagna CE, Chen JH, Kuo H-R, Lambert WC:Localization of left-handed Z-RNA in the outer cortical secondary fiber cells of the adult dog crystalline lens. *Scanning* 20, 255-256(1998)
9. Gagna CE, Chen JH, Kuo H-R, Lambert WC:Demonstration of Z-RNA in the dog eye lens epithelium (germinative zone). *Microsc Microanal* 4, 1108-1109(1998)
10. Gagna CE, Kuo H-R, Lambert WC:Z-RNA in eye lens differentiating cell epithelium. *Scanning* 21, 152-154(1999)
11. Gagna CE, Kuo H-R, Lambert WC:Left-handed Z-RNA in lens epithelium: preequatorial zone. *Microsc Microanal* 5, 1290-1291(1999)

Use of Scanning Electron Microscopy to Study the Seed Morphology and Anatomy of Twenty-Six Trees of Leguminosae

NABARUN GHOSH*, A. CHATTERJEE† AND DON W. SMITH‡

*Baylor College of Medicine, Houston, TX, USA; †CAS, Department of Botany, University of Calcutta, India; ‡Department of Biology, University of North Texas, Denton, TX, USA

Application of SEM data to the angiosperm classification dates back to the late fifties of our century but until more recently has remained without influence upon the shaping the angiosperm systems. This disregard of the ultrastructural potential was due to the few comparative data available. Recently in 1999 ultrastructural features obtained from SEM study have been used for delimitation of 45 taxa of the family Solanaceae (Watanabe *et al.* 1999).

We used a light microscope and SEM in this micromorphological study on 26 leguminous tree species. We cut transverse and longitudinal sections of the seeds of different species of *Acacia, Albizia cassia* and *Dalbergia.* We observed sections from different regions of seeds: midseed, near the hilum and two distal ends. The anatomical study with SEM on the seed sections revealed the size, shape, and number of tiers and cellular organization of the epidermis, hypodermis, endosperm and internal structural details.

We scanned the seed sections with SEM and observed the distinctive anatomical features of each species by which they could be differentiated from the other species (Ghosh *et al.* 1997). We observed the epidermal cells that were round, columnar, cuboidal or sometimes elliptical. The characteristic presence of "hour glass cells" was noted in the hypodermis of some species of Caesalpinoidae. Two species of *Cassia* (*siamia* and *spectabilis*) contained hourglass cells although the number and orientation of those cells varied from each other. In *A. falcataria* a green storage tissue that possessed stoma everywhere they were visible with higher magnification with SEM (×800). In all three species of *Dalbergia* the epidermal layer was uniseriate but the hypodermal layer was broad having a pattern characteristic to each species. In *D. sissoo* we found distinct stomata evenly distributed in the storage tissue. In this study, we observed the presence of multiseriate epidermis with double palisade layer in three species of *Cassia* (*glauca*, *siamia* and *spectabilis*). In *siamia* and *spectabilis* the characteristic presence of hourglass cells was noted. Corner (1951), in describing the structure of legume seeds, stated that the outer columnar epidermal cells (palisade cells) characteristically occurred in a single row.

Bragg *et al*. (1984) reported the presence of double palisade layers first in *Cassia fasciculata*. Bragg examined the seed coats of *C. alata* and *C. romeriana* seeds and found the presence of double palisade layers as well and suggested further sampling be taken to determine whether double palisade layers are a generic character for *Cassia*. We also noted stomata in the storage tissue of seeds of *A. falcataria* and *D. sissoo*. Cross sections of these seeds appeared green under a dissecting scope. Rugenstein and Lersen (1981) observed stomata on the surfaces of eight different species of *Bauhinia* including *B. varigata*. They also reported that the size of the stomata varied widely and the stomata were absent near the hilum. We found stomata in storage tissue that was not reported earlier. The function of these stomata is unclear, but the transections of the testa obtained by Bragg *et al.* (1984) clearly showed the presence of large areas for gaseous exchange. In this study the association of green tissue with the stomata may indicate occurrence of active photosynthesis during the early period seed germination in these species having stomata in the storage tissue. The endosperm pattern was different in the different species of the same genera. The endosperm pattern was different in *Albizia falcataria* and *lebbeck. Dalbergia assamica, latifolia*. Again, in the two species of *Cassia*, viz., *siamia, spectabilis* the endosperm pattern was very species specific and therefore useful in distinguishing one from the others.

This investigation on seed surface and seed anatomy of the leguminous species revealed useful diagnostic features for distinct identification and taxonomic interpretation.

Reference

Bragg, L. H. and Bridges, T. L. (1984). Testa characterization of selected Caesalpinioideae (Leguminosae) genera. Scanning Electron Microsc. 1984, pp. 1751-1758.

Corner, E. J. H. (1951). In: The leguminous seeds. Phytomorphology. 1 (1951), pp. 117-150.

Ghosh, N. and Chatterjee, A. and Smith, D. W. (1997) Observation on the epidermal layer of the seed sections of twelve leguminous trees. Texas Journal of Microscopy. Vol. 28 No. 2, 1997. p. 45.

Rugenstein, S. R. and Lersten, N. R. (1981). Stomata on seeds and fruits of Bauhinia. Amer. J. Bot. 68 (1981), pp. 873-876.

Watanabe, Hitoshi, T. Ando, Eshio N. *et al.* (1999) Three groups of species in Petunia sensu Jussieu (Solanaceae) inferred from intact seed morphology. Amer. J. Bot. 86(2): 302-305. 1999.

Elemental Analysis of the Components of *Plectonema boryanum* Using Regular and Overplus Cells in Conjunction with a Scanning Electron Microsope and Energy Dispersive X-ray Spectroscopy

J.J. GOLDBERG,* MICHAEL J. BAXTER,* AND T.E. JENSEN*

Department of Biological Sciences, Lehman College & CUNY Grad. Center, Bronx, NY, USA

The elemental composition of polyphosphate bodies (PPB's) and other components of the cell have previously been determined by T.E.Jensen *et al.*, and others, using energy dispersive X-ray spectrometers(EDX)[1]. In this present study we perform a quantitative analysis of normally grown cells and cells that were grown in the overplus phenomenon.

Cells of *Plectonema boryanum* were grown in modified Fitzgerald's media and harvested after a logarithmic growth phase of 14 days. The overplus cells were grown as has been previously described by Baxter *et al.*[2] The cells were exposed to 100ppm of lead, as well as other metals separately, for one hour. The cells were then air dried on a Ni grid or on a mount and gold coated.

For X-ray analysis cells were first located using the TEM mode, and then the microscope was switched to the SEM mode. Analysis of cell components was carried out using the spot mode (75Kv). The objective lens current was adjusted to receive a total X-ray count of 600–1000cps. Spectra were collected on a PGT IMIX (EDX). The data was analyzed using a bulk sample analysis program (ZAF) in standardless mode (w/w), based on the Hall continuum theory[3].

Approximately forty of the normally grown cells and forty of the overplus cells were analyzed, and their average percentages were calculated. The sheath, the wall and the PPB's were analyzed in each cell.

The cells grown in the normal manner and exposed to lead contained the following averages: the sheath O (72.71%), C (27.29%), Pb (0%), P(0%), Ca (0%), K (0%), Fe (0%), S(0%), Cl (0%), Al (0%), Mg (0%). The wall contained O (38.60%), C (0%), P (0%), Pb (14.92%), Ca (1.09%), K (0%), Fe (0%), S (.99%), Cl (29.5%), Al (14.9%), Mg (0%). The polyphosphate bodies contained O (57.5%), C (13.79%), P (14.9%), Pb (9.4%), Ca (0%), K (0.3%), Fe (0%), S (1.9%), Cl (0.81%), Al (1.67%).

The overplus cells were exposed to lead under the same conditions, the results were: sheath O (72.71%), C (27.29%), Pb (0%). The wall contained O (47.38%), C (0%), P (0%), Pb (5%), Ca (1.12%), K (0%), Fe (0%), S (3%), Cl (29.5%), Al (14%), Mg (0%), and the polyphosphate bodies contained O (61.73%), C (12.43%), P (14.10%), Pb (9.49%),Ca (0%), K (0%), Fe (0%), S (2%), Cl (0%), Al (.25%).

The volume of the cell was then determined by using the formula for calculating the volume of a cylinder, *viz.* $V = \pi r^2 h$, and the volume was obtained using $V = 4/3\pi r^3$ for a spherical body. All calculations were done at the same magnification of 40,000×[2]. The volumes of the various components were calculated. This brought us to the conclusion that even though the cell on a whole has more volume than the polyphosphate bodies the polyphosphate bodies will bio concentrate more of the metal than the rest of the cell.[2] The analysis of the overplus cells further supports this; since the PPBs are larger and more numerous they occupy a greater volume of the cell.

References

1. T.E. Jensen *et al.*, Uptake of heavy metals by *Plectonema boryanum (Cyanophyceae)* into cellular components, especially polyphosphate bodies: An X-ray energy disspersive study. Environ Pollut Ser A 27(1982), 119–127
2. M. Baxter and T.E. Jensen, Cell volume occupied by polyphosphate bodies during the "polyphosphate overplus" phenomenon in *Plectonema boryanum*. Cytobios 45 (1986) 147–159
3. T.A. Hall, Quantitative electron probe X-ray microanalysis in biology. Scanning Microscopy 3, 461–466

Tracking Moisture Migration in a Model Bilayered Food using LSCM

LINNEA M. HALLBERG AND IRWIN A. TAUB

Soldier and Biological Chemical Command, U.S. Army, Natick, MA

A model bilayered whey gel system containing the dye fluorescein was constructed to represent a two-component food (i.e., a simple sandwich of bread and homogeneous filling). It was then sealed, optically scanned for the fluorescent intensity, stored, and rescanned periodically to track the migration of the fluorescent dye as an indicator of the migration of moisture. The scanning was performed with a real-time, slit-scanning, upright confocal microscope using an air-cooled Argon laser to excite the fluorescein (0.01%) at 488 nm, and a CCD and a 530/30 nm band pass filter to detect the emission. A series of optical sections (25μ apart) were auto-collected by a computer controlled z-drive. Comparison of topographical representations of the fluorescence data showed the time-dependent changes in the location of the fluorochrome. These changes reflected the migration of the water from the high moisture gel (80%), through a nylon filter membrane, to the lower moisture (60%) gel within 7 days. This technique, where applicable, is capable of providing a dynamic 3-D rendering of moisture migration that can be used to validate the modeling of such migration.

Distribution of Laminin, Fibronectin, Collagen I, II, IV and X in the Human Adolescent Growth Plate

M. HELMREICH, G. HÄUSLER,* M. EGERBACHER

Institute of Histology and Embryology, University of Veterinary Medicine, Vienna; *University of Vienna, Pediatric Department, Vienna, Austria

Collagens represent the major proteins in bone and cartilage matrices and play an important role in determining the size, shape and strength of tissues. Collagen II is the principal protein of cartilage, collagen X is the major protein found in hypertrophic cartilage, and collagen I is the most abundant protein in bone. Whereas expression of these collagen types has been well characterized, data on the presence and local distribution of other proteins which might contribute to the architecture of the growth plate are sparse. In this respect, the interaction of chondrocytes with its extracellular matrix is considered an essential factor for

stabilizing the chondrogenic phenotype which is mediated, at least in part, by integrin receptors which bind to collagen II, fibronectin and laminin. So far, data have been derived from either different species or prenatal or neonatal human specimen.[1]

In this study, we investigated the local distribution of these matrix proteins in childhood and adolescent growth plates, which has to our knowledge not been done before due to the poor availability of tissue.

Material was obtained during surgical correction for congenital or traumatic leg length difference (epiphysiodesis) from 4 children (2 male, 2 female) aged 7 to 15 years. Tissue samples were fixed in 4% buffered formalin, decalcified in EDTA 8%, and embedded in paraffin.

Immunohistochemistry of collagen types I, II, IV and X, laminin and fibronectin was performed on paraffin sections after enzymatic pretreatment. For collagen type II and X digestion with 0.01% hyaluronidase (Sigma, Austria) in PBS pH 6.7 for 4 hours at 37°C and subsequently with pepsin (Sigma, 1mg/ml 0.1N HCl) for 30 min at 37°C was performed. Immunostaining for collagen type I needed digestion of sections with 0.1% pepsin in 0.5M acetic acid for 2 h at 37°C. Collagen IV, laminin and fibronectin required protease digestion (Sigma, 0.1% protease in 0.05M Tris HCl buffer, pH 7.2) for 2 min at 37° C.

Antibodies were obtained from Quartett, Berlin, D (collagen II, dilution 1:100, collagen IV, dilution 1:100, collagen X, dilution 1:50) and from Southern Biotechnologies Inc., AL, USA (collagen I, dilution 1:100), from Dako, DK (laminin, dilution 1:1000) and Sigma, A (fibronectin, 1:1000). Incubation with primary antibodies at 4°C lasted overnight. Bound primary antibodies were detected with anti-mouse, anti-rabbit, or anti-goat biotinylated secondary antibodies (Vector Lab., 1:200) following FITC-labeled streptavidin (Vector Lab.,1:50). Nuclei were counterstained with propidium iodide. Staining results were evaluated with a confocal laser scanning microscope (Leica TCS-NT, Germany).

The cartilage typical collagen type II was present throughout the whole width of the epiphyseal cartilage, providing the fibrous network of functional hyaline cartilage. Collagen I is expressed by osteoblasts and was therefore restricted to the bone deposits on the remains of calcified cartilage trabeculae. The calcified center was positive for collagen II.

Collagen type X proved to be characteristic for the hypertrophic zone. Staining of collagen X was seen as a fine fibrillar network reaching from the hypertrophic zone deep into the zone of ossification being co-localized with collagen II in the center of the trabecules. Fibronectin was detected in the interterritorial matrix of all zones. Additionally, it was expressed in the matrix between hypertrophic chondrocytes and in trabecules of the zone of ossification, matching with collagen II and X staining. Laminin was specifically located in the pericellular halo of chondrocytes in the resting zone. Only sparse immunoreactivity was seen in the proliferation zone which disappeared completely in the hypertrophic zone. Collagen IV could not be detected in the epiphyseal cartilage at all, whereas collagen IV together with laminin was detected surrounding the capillary loops in the resorption zone.

On the rare occasion of human childhood and adolescent growth plate specimens, we were able to localize collagens I, II and X to the regions characteristic for the respective cell type known from animal experiments. Collagen II, X and fibronectin were co-localized deep in the trabeculae of the ossified regions. Rather unexpectedly, laminin, the most relevant ligand of integrin ß1 was present in reserve cell cartilage, with fading immunoreactivity in the proliferating zone.

References

1. Dürr J, Lammi P, Goodman SL, Aigner T, von der Mark K: Identification and Immunolocalization of Laminin in Cartilage. Exp Cell Res 222, 225-233 (1996)

Recent Investigations of Food Container-Product Interactions Using Scanning Electron Microscopy and X-ray Microanalysis

DAN HOWELL, JAMES E. CHARBONNEAU, PH.D.

National Food Processors Association, Washington, DC, USA

Corrosion occasionally occurs either inside or outside the metal food container. The canned product may develop a condition that is objectionable to the consumer or results in early failure. An expert in the field of corrosion must be able to identify not only the type of corrosion but the cause of the problem in order to prevent it from happening again. The National Food Processors Association (NFPA) is often called on to provide an independent third-party evaluation of corrosion problems. This technical assistance to industry is done as part of NFPA's ongoing package integrity program. In 1999, NFPA investigated 30 incidences of container corrosion. In this report, three representative case histories are discussed. They were investigated using an Amray 1600 T Scanning Electron Microscope (SEM) and a Kevex Sigma 2 Xray Microanalysis equipment.

Case History #1: Perforations in Apple Juice Cans

Container: Three-piece welded with a gold epoxy phenolic inside enamel coating.

Problem: Pitting and perforations in less than 1 year storage time.

Thirty cans from various codes were submitted for testing. Representative cans from each code were chosen to investigate the spoilage problem. In one of the problem cans, a crack was found in the coating along the cut edge of the side seam weld. Using SEM in the backscattered

electron mode, exposed metal was found in the crack. Using EDS, the metal was determined to be iron from the can. A corrosion pit 60% through the can wall was found adjacent to the cut edge of the weld of a can with no evidence of spoilage. This finding is significant for the food producer when it comes to the distribution of product from this lot. The lot should be destroyed. This problem was caused by jagged welds. It is industry experience that welds with sharp cut edges are difficult to adequately protect with a liquid side seam stripe.

Case History #2: Internal Rusting in Canned Chicken Broth

Container: Two-piece draw and ironed with an epoxy or phenoxy-pigmented I/S coating.

Problem: Rust developed in the head-space area at microcracks in the internal coating.

The samples were submitted to determine whether the stain was rust or carmelized product and to determine the source of the stain. Using EDS, the stain was shown to be composed mainly of iron and oxygen; i.e., rust (Fe2O3). An SEM-EDS examination of the underside of the coating material removed from a rusted area using tape showed that the coating material was titanium-based and that tin and iron had detached from the tinplate surface of the can. This inside rust condition was initiated by cracks in the coating material that likely developed during container fabrication.

Case History #3: External Rusting on Tomato Cans

Container: # 10 Three-piece welded.

Problem: Heavy rusting on sporadic, non-contiguous areas on the outsides of the cans.

Using EDS, chloride and sulfur were found in the rusted areas. The presence of these elements suggests that hygroscopic salts were present in the rust. The cans had been shipped from California to Texas, and only some cans rusted. The cans were bright-stacked and wrapped in shrink-wrap. Only the cans that came in contact with the shrink-wrap were affected. Hygroscopic salts, moisture and oxygen inside the shrink-wrap packaging reacted with the exposed iron and caused this problem. The use of desiccants and oxygen scavengers inside the shrink-wrap packaging will prevent this problem from recurring.

Conclusion

NFPA has over 15 years experience in investigations of corrosion problems using the SEM together with EDS. This technology provides an excellent technique to help diagnose the many causes of corrosion on either the exterior or interior of a metal food container.

Study of the Effects of Spherical Aberrations Near Focus by Semi-wave theory

GUO LI, SAMN SHERWOOD,* AND SAMUEL COHEN

Electrical Engineering Department, University of Texas San Antonio, San Antonio, Texas; *Air Force Research Laboratory, Brooks Air Force Base, Texas; †US Army Natick RD&E Center

This paper studies the intensity distribution of light near focus for an optical system in the presence of large primary, secondary and tertiary spherical aberrations. The different effects of three kinds of spherical aberrations on the maximum intensity distribution of light, focal length shift, and half width of a focal spot in meridional plane are analyzed. In addition, this paper studies the effect of apodization function on the intensity distribution of light near focus. The study evaluates the resolution of a confocal optical system and provides significant information for improving scanning optical microscopy.

Confocal Laser Scanning Microscopic Observation in the 3-D Reconstruction Technique of Reflection Mode of Cytochrome Oxidase Activity in the Hamster Submandibular Gland

KEIICHI MORIGUCHI*‡, MICHIYA UTSUMI,* HATSUHIKO MAEDA†‡, YOICHIRO KAMEYAMA†‡, NORIKAZU OHNO*‡

Depts. of *Anatomy and †Pathology, School of Dentistry, and ‡Research Institute of Advanced Oral Science, Aichi-Gakuin University, Aichi, Japan

Cytochemical demonstration of the cytochrome oxidase activities in the mitochondria of granular duct cells of the hamster submandibular gland was compared in different fixative conditions. The mitochondrial formation and accumulation of cytochrome oxidase activities were determined by laser confocal microscopy in the 3-D reconstruction of reflection mode.

Materials and Methods

Submandibular glands of the hamster were removed under deep anesthesia with pentobarbital. These tissues were fixed with 0.5 or 2% glutaraldehyde(GA)-2% paraformaldehyde(pFA) in phosphate buffer, pH 7.4 (PBS) and irradiated by a microwave processor at 10 °C. We then used the microwave processor M1-17, 150W of Azumaya Co., Ltd., Tokyo, Japan. This processor easily kept fixatives in the low temperature using a chilled water bath[1]. We demonstrated cytochrome oxidase activity using the cytochemical methods with 1mg/ml 3,3'-diaminobenzidine (DAB), 1mg/ml crystallized cytochrome *c*, 0.4 mg/ml crystallized catalase and 7% sucrose and PBS.[3,4] To demonstrate

cytochrome oxidase activities the temperature and time were routinely kept at 37 °C for 60 min. All reacted specimens were postfixed for 60 min in 1 % phosphate-buffered osmium tetroxide at 4 °C and dehydrated in graded ethanol, and embedded in Quetol 653 resins. A 3-4 µm section was placed on glass slides. Specimens were examined with a Carl Zeiss laser confocal scanning microscopic system (LSM410 Co., Ltd., Germany) in reflection mode. Moreover, ultrathin sections were cut with an LKB ultramicrotome and examined by a JEM1210 electron microscope (JEOL Co., Ltd., Tokyo Japan) without uranyl and lead staining.

Results and Discussion

Extreme cytochrome oxidase activity was observed in the mitochondrial intermembrane-intracristal space when the tissues were fixed with 0.5% GA-2% pFA. As a result of the 3-D reconstruction, duct cells exhibit diversity in the form in their mitochondria (Fig. 1). An intense cytochrome oxidase activity was seen in the mitochondrial intermembrane-intracristal space (Fig. 2; the 2% GA-2%pFA fixed cells). For 3-D reconstruction study, duct cells showed spherical mitochondria. These results indicated that the 0.5% GA-2% pFA fixative method may be effective for the preservation of the mitochondrial structure and cytochrome oxidase activities.

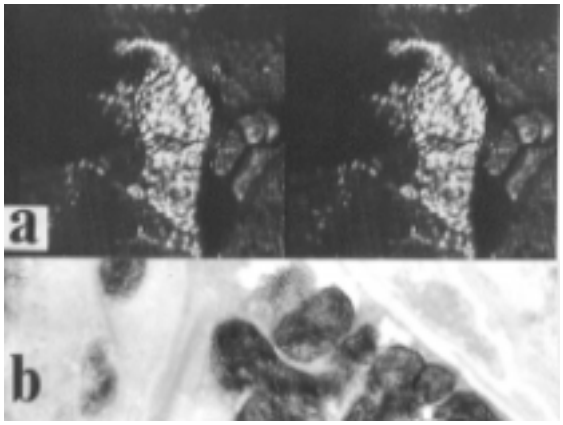

FIG. 1 Intramitochondrial accumulation of DAB deposits and mitochondrial morphology in duct cells fixed with 0.5% GA-2% pFA. Stereo pair (a) and TEM (b) photographs.

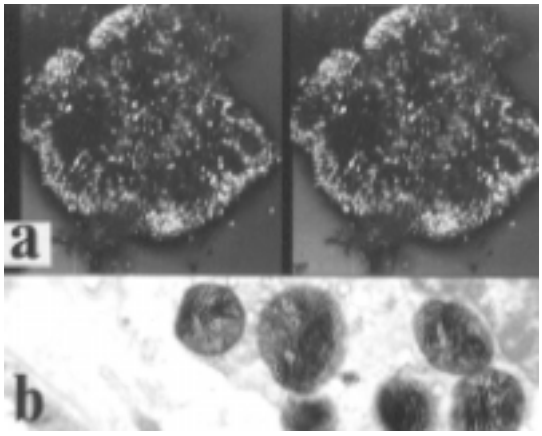

FIG. 2 Intracellular formation of mitochondrial DAB deposits in duct cells fixed with 2% GA-2% pFA. Stereo pair (a) and TEM (b) photographs.

References

1. Moriguchi K, Utsumi M, Maeda H, Kameyama Y, Ohno N: Confocal laser scanning microscopic observation and cytochrome oxidase activity in the hamster submandibular gland using microwave irradiated fixation. J Electron Microsc 21, 161–162 (1999)
2. Moriguchi K, Utsumi M, Ohno N: Mitochondrial fixation for the detection of cytochrome oxidase activity using microwave irradiation. Okajimas Folia Anat Jpn 74, 207-216 (1998)
3. Moriguchi K, Utsumi M, Ohno N: Mitochondrial membrane structure and cytochrome oxidase activity after fixation of the hamster submandibular gland duct cells by various concentrations of glutaraldehyde and paraformaldehyde. Aichi-Gakuin Dent Sci 12, 39-44 (1999)

A Scanning Electron Microscopic Study of Cold-Stored Small Bowel: Comparison of Euro-Collins and Lactated Ringer Solutions

SUSANNE ÖNER,* FERIHA ERCAN,* SERAP ARBAK,* AYMELEK YALIN**

Departments of *Histology-Embryology and **Anatomy, School of Medicine, Marmara University, Haydarpaşa, Istanbul, Turkey

The increasing use of the small bowel for transplantation necessitates the development of optimum preservation techniques.[1–6] The aim of our study was to investigate time-related morphological changes of the rat small bowel during preservation of the organ in hypothermic Euro-Collins and Lactated Ringer solutions. Small bowels were perfused via the ascending aorta with either Euro-Collins or Lactated Ringer solution. After flushing of the intestinal lumen with cold saline solution, perfused grafts were placed in respective preservation solutions at 4°C for 0, 3, 6 and 12 hours. Perfusion and storage in saline solution at 4°C was performed for controls. Biopsy samples were prepared for examination at the light and scanning electron microscopic levels. Routine light microscopy revealed good preservation of the small bowel mucosa after 6 hours of preservation in Lactated Ringer solution and moderate preservation in Euro-Collins solution. Severe damage of the mucosa, especially of the crypts, occurred after 12 hours of preservation in both solutions. Scanning electron microscopy revealed preservation injury such as changes of the villi shape, epithelial rupture with or without denudation of the lamina propria and complete loss of intestinal villi. Preservation in Euro-Collins solution showed good preser-

vation of the small bowel tissue after 3 hours, moderate preservation after 6 hours and severe tissue damage after 12 hours of preservation. Small bowel preserved in Lactated Ringer solution showed good preservation at 3 and 6 hours of cold ischemia and severe tissue damage at 12 hours of preservation. According to these results we conclude that, even though Lactated Ringer solution showed better tissue preservation than Euro-Collins solution, both preservation solutions are suitable for short term preservation of the small bowel and that further ameliorations of the preservation solutions and/or techniques are required for long term preservation.

References

1. Galvao FHF, Waitzberg D, Logulo A, Soares S, Goncalvales EL: Histological and permeability alterations in cold-stored small bowel: a comparison of University of Wisconsin and Euro-Collins solutions. Transplant Proc, 26, p: 1496–1499, 1994
2. Kokudo Y, Furuya T, Takeyoshi K, Nakamura S, Zhang S, Murase N, Todo S: Comparison of Euro- Collins solution, University of Wisconsin and Ringer's Lactate solutions in rat small bowel preservation for orthotopic small bowel transplantation. Transplant Proc, 26, p: 1492–1493, 1994
3. Rodriguez FJ, Toledo-Pereyra LH, Suzuki S: Twenty four hour total small bowel hypothermic storage preservation and transplantation in the rat: a study of various preservation solutions. J Invest Surg, 7, p: 439–451, 1994
4. Schraut WH: Current status of small bowel transplantation. Gastroenterology, 94, p: 525–538,1988
5. Schweizer E, Gassel A, Deltz E, Schroeder P: Morphologic and histologic alterations after small bowel transplantation-A comparison of different perfusion solutions. Transplant Proc, 24, p: 1087–1090, 1992
6. Toledo-Pereyra LH: Small bowel transplantation: Evaluation of methods and ideas and current concepts. Transplant Proc, 24, p:1083–1084, 1992

Heating of B-Lactoglobulin A Solution in a Closed System at High Temperatures

SONGSIN PHOTCHANACHAI AND NAOFUMI KITABATAKE

Research Institute for Food Science, Kyoto University, Japan

B-lactoglobulin A solution at pH 6.4 and 7.5 was heated to 180°C at the rate of 6C/min. In both pHs two independent endothermic peaks were observed by differential scanning calorimetry. The first peak appeared below 100°C and corresponded to the thermal denaturation of protein, which led to the aggregation and polymerization of molecules through disulfide linkage, and the second peak appeared around 150°C and corresponded to the decomposition of molecules as judged from electrophoresis. The B-lactoglobulin A solution heated at higher temperatures showed an increase in viscosity up to 100°C. The viscosity decreased when the solution was heated to above this temperature. The reduction of viscosity was remarkable at pH 6.4, due to change in the size of the aggregates and decomposition of B-lactoglobulin A. The cleavage sites of B-lactoglobulin A and the mechanism of cleavage have been determined.

Diffusion of Curing Salts in Meat: Effect of Sodium Chloride on Tissue Microstructure

A. PINOTTI, A. CALIFANO, AND N. ZARITZKY*

Centro de Investigación y Desarrollo en Criotecnología de Alimentos (CIDCA). CONICET. Fac. Cs. Exactas. *Depto Ing. Qca. Fac. de Ingeniería. UNLP. 47 y 116 (1900) La Plata, Argentina

Introduction

Curing process utilizes sodium chloride, nitrite and nitrate. One of the methods used by the industry is the immersion of the meat cut in brines. In this case salt penetration is related to the equilibrium between the salt concentration in the interior of the meat piece and the external solution. The diffusion of NaCl in meat tissues was studied by Wood[1] and Fox[2]. The objectives of the work were: a) to determine the diffusion coefficient of sodium nitrite and potassium nitrate in pork tissue (*Longissimus dorsi*) using brine solutions at 4°C and 20°C; b) to establish the effect of sodium chloride on the diffusion coefficients.

Materials and Methods

A radial (unidirectional) diffusion system was adopted using long cylinders of *Longissimus dorsi* pork tissue that were immersed in brines of different composition ($NaNO_2$, KNO_3 and NaCl). The solutions were stirred to assure constant solute concentration at the solid-fluid interface. At different times two cylinders were taken out from the brine; only the central zone of each cylinder was kept to avoid border effects. The mass of nitrite and nitrate present in the samples was determined; experiments were performed at 4°C and at 20°C and the water content of the tissue was measured. Equilibrium concentrations were obtained by immersion of tissue samples in the different brines during 48 hours. A spectrophotometric method (Hach 371) was used to determine nitrite. Nitrate was determined using the Hach kit Nitraver 6; the nitrate was reduced to nitrite using cadmium and then nitrite was measured as was explained previously. Meat tissue samples were observed by scanning electron microscopy (SEM 505, Philips).

Meat tissue can be considered as an insoluble matrix and an aqueous phase through which the solute diffuses with an effective diffusivity in the matrix (Dm). The microscopic mass balance was considered for an infinite cylinder with radial diffusion.When the solid material, initially containing an initial concentration of the solute, is brought into contact with a well-stirred solution of constant concentration, the concentration at the solid-fluid interface corresponds to the equilibrium concentration. The total

uptake at a given time t, M(t) is calculated by integrating between 0 and R, the analytical solution of Eq. 1[3]:

$$M(t) = M(\infty)\left(1 - \sum_{n=1}^{\infty} 4\frac{\exp(-Dm\,\alpha_n^2\,t)}{R^2\alpha_n^2}\right) \quad (1)$$

where M(t) is the mass of solute that enters in the tissue during time t expressed as g solute / g meat tissue; M(∞) is the maximum amount of solute that could enter at infinite time and corresponds to the concentration of salt in equilibrium with the external solution; R .α_n are the n-roots of equation J_o (R α_n) = 0 being J_o the zero order Bessel's function.

A computer program was used to calculate diffusion coefficients of nitrite and nitrate. The mass that entered the tissue at a given time, M(t), and the maximum amount of solute that would be entered at infinite time, M(∞) were used to determine the experimental values of the dimensionless total uptake M*, which is given by the ratio between M(t) and M(∞). Diffusion coefficients were proposed and theoretical values of M* were calculated. The value of diffusivity that lead to the minimum differences between experimental and theorical values was selected by an iterative procedure.

Results and Discussion

Table I shows the obtained diffusion coefficients for the assayed conditions. Diffusion coefficients increased with increasing temperature and with the presence of high NaCl concentrations.

The mean water content in the tissue ranged between 72 and 74 %. The Maxwell-Stefan's theory could not explain,

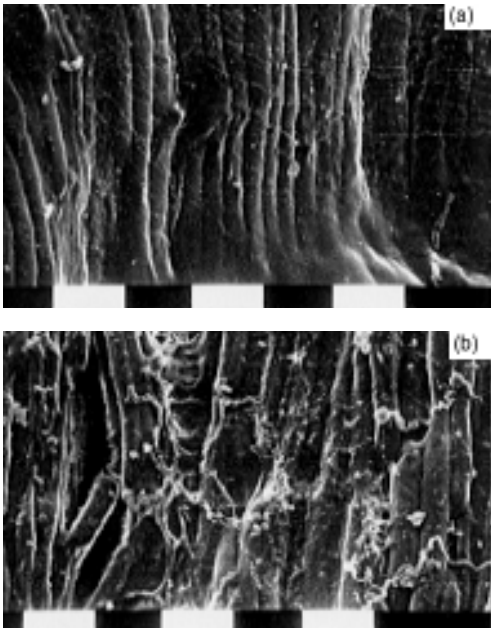

FIG.1 Scanning electron micrographs of pork tissue treated with a) 140g/l NaCl; b) 2.5g/l KNO_3. Scale = 100 µm between marks.

TABLE I Effective diffusion coefficients (Dm) in pork tissue

Solution	Dm (m^2/s)$NaNO_2$	
	4°C	20°C
$NaNO_2$ 3g/l	$3.8 \cdot 10^{-10}$	$4.1 \cdot 10^{-10}$
$NaNO_2$ 3g/l + NaCl 10g/l	$4.0 \cdot 10^{-10}$	$5.6 \cdot 10^{-10}$
$NaNO_2$ 3g/l + NaCl 140g/l	$5.1 \cdot 10^{-10}$	$8.5 \cdot 10^{-10}$
Solution	Dm (m2/s)KNO_3	
KNO_3 2.5g/l	$4.1 \cdot 10^{-10}$	$4.0 \cdot 10^{-10}$
KNO_3 2.5g/l +NaCl 140 g/l	$8.8 \cdot 10^{-10}$	$9.5 \cdot 10^{-10}$

by the simultaneous diffusion of electrolytes, the observed increase in the diffusion coefficients when NaCl was present. Another aspect that should be considered is that the penetration of a chemical preservative in a tissue may affect its microstructure, leading to diffusion coefficients that depend on the concentration of the diffusing solute. The molecular diffusion coefficient (D_{AB}) is related to the effective diffusion coefficient (Dm) in a complex matrix by different factors that consider the volumetric fraction of the solvent, the degree of obstruction in the matrix, and the interactions between matrix-solvent-and solute. High levels of NaCl might affect tissue microestructure allowing the penetration of nitrite and/or nitrate; this modification of the fiber structure leads to higher diffusion coefficients. It has been reported that at high concentrations of NaCl (> 1M) in meat tissue the thick filament is dissociated into its constituent myosin molecules and other proteins[4]. These microestructural changes, as shown by the SEM micrographs (Fig.1a,b), could explain the rise in the diffusion coefficients of nitrite and nitrate in the presence of NaCl.

References

1. Wood F W: The Diffusion of Salt in Pork Muscle and Fat Tissue. *J Sci Food Agric* 17, 138-140 (1966)
2. Fox J B: Diffusion of Chloride, Nitrite and Nitrate in Beef and Pork. *J. Food Sci.* 45, 1740-1744 (1980)
3. Crank J: *The Mathematics of Diffusion*, Oxford University Press, London (1957)
4. Offer G and Trinick J: On the Mechanism of Water Holding in Meat: the Swelling and Shrinking of Myofibrils. *Meat Sci* 8: 245-281 (1983)

The Disulfide Reducing Agent Dithiothreitol (DTT) Affects Cilia Formation During Development

HEIDE SCHATTEN AND AMITABHA CHAKRABARTI

Department of Veterinary Pathobiology, University of Missouri-Columbia, 1600 East Rollins Street, Columbia, MO, USA

Elucidating the roles of disulfide and sulfhydryl bonds during specific processes of the cell cycle has brought

insights into membrane biology, cell cycle events, and protein chemistry. Dithiothreitol (DTT) has been used to study pronuclear decondensation and pronuclear fusion during fertilization and cell division (Schatten, 1994) and has also provided insights into molecular mechanisms of metabolic defects causing disease (Bardwell *et al.*, 1991; Taniyama *et al.*, 1991). Here we explore the effects of DTT on cilia formation during development of sea urchin embryos.

Gametes of the Californian sea urchins *Lytechinus variegatus* and *Strongylocentrotus purpuratus* were obtained by intracoelomic stimulation with 0.5M KCl. Eggs were fertilized and cultured to the morula stage when DTT was applied at concentrations from 1–5 mM for 24 h. The embryos were fixed in 1% glutaraldehyde in 0.4M sodium acetate buffer (pH 6.1) for 1 h at room temperature and washed in the same buffer. The samples were post-fixed with 1 % osmium tetroxide in 0.4 M sodium acetate buffer (pH 6.1) for 1 h, and dehydrated in a graded series of ethanol washes. Preparation for scanning electron microscopy was continued by critical-point drying and sputter coating with gold. Samples were viewed in a JEOL JSM 35 scanning electron microscope. For transmission electron microscopy samples were embedded in Spurr's embedding medium, ultrathin sectioned and poststained with 1% ethanolic uranyl acetate followed by lead citrate. Preparations were analyzed in a JEOL 1200EX scanning transmission electron microscope.

Our analysis of DTT treated embryos revealed that proper cilia formation was inhibited. At 5mM DTT basal bodies were found underneath the plasma membrane oftentimes in perpendicular orientation while cilia were not formed. Treatment with 1mM DTT resulted in aberrant formation of cilia that could be discerned above the plasma membrane as short fragments compared to normally elongated cilia in control cells. These short cilia contained microtubules and a basal apparatus consisting of basal body, basal foot, basal foot cap, centrioles, striated rootlets, and striated site arms. At 2mM DTT the striated rootlets appeared fractured. In addition to these effects on cilia DTT (1-5mM) treated cells also exhibited alterations of mitochondrial cristae and showed an increase of annulate lamellae indicating that membrane structure was affected. In summary, these results show that DTT affects cilia formation through membrane-related mechanisms and not through microtubule dysfunctions.

References

Bardwell J. C. A., McGovern, K., and Beckwith, J. (1991). Identification of a protein required for disulfide bond formation in vivo. Cell 67:581-589.

Schatten, H. (1994). Dithiothreitol prevents membrane fusion but not centrosome or microtubule organization during the first cell cycles in sea urchins.

Taniyama, Y., Kuroki, R., Omura, F., Seko, C., and Kikuchi, M. (1991). Evidence for intramolecular disulfide bond shuffling in the folding of mutant human lysozyme. J. Biol. Chem. 266:6456-6461.

Scanning Electron Microscope Study of the Flowers of *Nelumbo nucifera*

CINDI L. SCHWARTZ AND H.J. ARNOTT

The Department of Biology and the Center for Electron Microscopy at the University of Texas at Arlington, Arlington, TX, USA

Nelumbo lutea, the yellow lotus, is found in lakes in the southern United States. Lotus flowers are large, about 20cm in diameter when fully opened, and extend above water level on a long, thin petiole. The flowers do not have sepals, but have 10–20 petals that are arranged around a large, central receptacle. Lotus flowers contain 50–100 stamens surrounding the receptacle as well. The conical receptacle or carpophore contains about 20 carpels.

As previously seen in lotus leaves[1], the outer surface of the receptacle contains papillose epidermal cells and large,

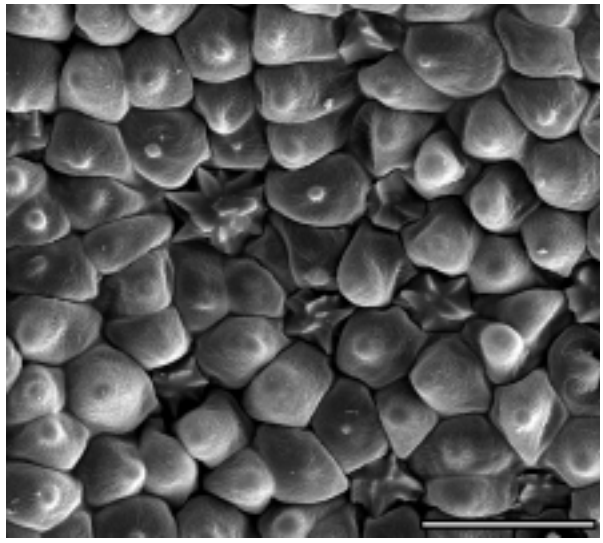

FIG. 1 Surface of petal showing papillose epidermal cells and unicellular crystal idioblasts. (bar=50 μm)

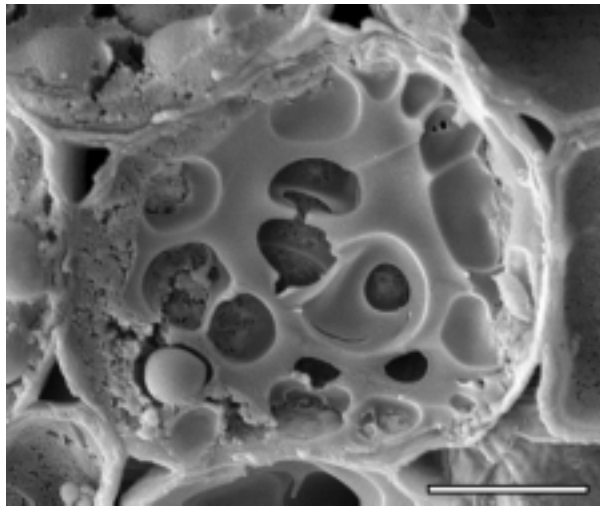

FIG. 2 Cell with densely packed cytoplasm found near the epidermis of the receptacle. (bar=10 μm)

multicellular crystal trichomes. Large airspaces give the receptacle a spongy consistency. Calcium oxalate crystals are found lining these airspaces.

The petals of lotus also have papillose epidermal cells. However, the crystals are not found on multicellular trichomes, but in single-celled idioblasts (Fig. 1). Calcium oxalate crystal druses line the airspaces found at the base of the petals.

The stamens of lotus have a short filament with the anther about twice as long as the filament. The anther contains four pollen sacs. The pollen grains of lotus are tripunctate with a convoluted surface.

Interestingly, the lotus flower is able to regulate its own temperature. It can maintain a temperature of 30–36°C during a 2–4 day period when ambient temperature fluctuates from 10–45°C.[2] Only two other species, *Philodendron selloum* and *Symplocarpus foetidus*, are also known to be thermoregulatory.[3]

All parts of the flower have been shown to contribute to the generation of heat. The receptacle generates 54%, while the petals and stamens generate about 23% each.[2] The exact mechanism by which lotus generates heat is unknown. It is believed through calorimetric experiments that the energy comes from the breakdown of carbohydrates.[2] However, no studies have been done to look at this at a microscopic level. The receptacle and stamen filaments contain starch, the presumed energy resource.

There are two distinct cell types found in the flower. One type of cell contains densely packed cytoplasm with numerous vacuoles (Fig. 2) and the other is packed with starch. In the petal base and receptacle, both cell types tend to be adjacent to the large airspaces. In the receptacle, these cells are also found near the epidermis.

References:

1 C.L. Schwartz, H.J. Arnott. 1996. Investigation of Water Beading on the Adaxial Leaf Surface of *Nelumbo Nucifera*. Texas Society for Electron Microscopy platform presentation. Available as text from the authors upon request.

2 Seymour, R. & Schultze-Motel, P. 1998. Physiological Temperature Regulation by Flowers of the Sacred Lotus. *Phil. Trans. R. Soc. Lond.* B 353:935-943.

3 Seymour, R. 1997. Plants That Warm Themselves. *Scientific American.* 276:104-109.

Role of SH Residue on Heat-induced Aggregation of B-Lactoglobulin A

RITSUKO WADA AND NAOFUMI KITABATAKE

Research Institute for Food Sciene, Kyoto University, Japan

B-Lactoglobulin A (B-LGA) is a major protein in whey fraction of bovine milk. Its molecular weight is about 18,400 and has two disulfide bonds and one free SH residue at Cys121. B-LGA gave soluble aggregates through S-S bond by heating under salt free condition at neutral pH. The aggregates formed huge size of polymer by addition of NaCl. When a free SH residue of B-LGA molecule was blocked by N-ethylmalemide (NEM), no aggregates were formed by heating and kept the monomer structure even by addition of NaCl. On the other hand, when SH-blocked B-LGA (NEM-B-LGA,10, 40 mg/ml, pH 7.5) was heated at 80°C for 1 hr in the presence of reducing agent dithiothreitol (DTT), NEM-B-LGA formed aggregates through intermolecular S-S bond. The amount of aggregates increased with the increase of DTT concentration, and decreased at high DTT concentration. This means that a free SH residue of DTT is available for the induction of intermolecular SH/S-S exchange reaction between B-LGA molecules and and the formation of aggregates. In this study we investigated the role of free SH residue of B-LGA. DTT was added after NEM treatment of heated b-LGA. Further polymerization did not occur with 2 hr of incubation or heating with DTT.

Oscillating Trichobothria in the Low Temperature SEM: Biological Capacitors or Charging Artifacts

WILLIAM P. WERGIN,* RONALD OCHOA,† ERIC F. ERBE* AND DAVID C. JOY‡

*Nematology Laboratory, USDA ARS, Beltsville Agricultural Research Center, Beltsville, MD;
†Systematic Entomology Laboratory, USDA ARS, Beltsville Agricultural Research Center, Beltsville, MD;
‡EM Facility, University of Tennessee Knoxville, and Oak Ridge National Laboratory, Oak Ridge, Tennessee, USA

Mites, which are the second largest arthropod group after insects, contain numerous types of specialized, external setae that function as mechano-, chemo-, thermo-and hygro-receptors (Evans 1992). Recently, Wergin *et al*. (2000) demonstrated the advantages of using low temperature scanning electron microscopy (LTSEM) to distinguish and characterize the different types of setae found on mites. During this study, one highly specialized type of seta, known as a trichobothrium, exhibited regular and repeatable oscillations in the LTSEM as the frozen specimens were imaged. Subsequently, trichobothria were imaged in two other species and exhibited the same phenomenon. No other type of seta behaved in this manner. This study provides details on these observations and attempts to offer an explanation for the movement.

Three species of mites, the itch mite, *Pyemotes tritici* and two beetle mites, *Archegozetes longisetosus* and a *Galumna jacoti*, were prepared for LTSEM as previously described (Wergin *et al*. 2000). Briefly, samples harboring the mites were excised and placed on flat specimen holders and frozen conductively by placing the holders on the surface of a pre-cooled brass bar whose lower half was submerged in LN_2. After 20-30 seconds, the holders containing the frozen samples were cryo-transferred under vacuum to a

cold stage in the pre-chamber of a cryo-system, sputter coated with platinum and then transferred to a pre-cooled (–170° C) cryo-stage in an SEM for observation.

Each of the three species has two trichobothria that occur anterior and lateral, left and right, on the mite. The shape of these trichobothria is distinctly different in each of the three mites: in *P. tritici*, they are bulbous, about 10 µm in length, 6 µm at their widest diameter and have a 0.5 µm diameter stalk (Fig. 1); in *A. longisetosus*, they are elongate, 150 µm in length and 5 µm in diameter along their length; in *G. jacoti* they are also elongate, about 100 µm long. However their diameter gradually increases towards the tip. They are 5 to 6 µm in diameter near the tip but gradually taper to only 2 to 3 µm at their base. Depending on the kV, magnification and scan rate, these (frozen) trichobothria oscillate when they are imaged or photographed with their longitudinal axis perpendicular to the raster scan. The oscillation consists of a relatively slow movement in one direction followed by a quick return to the original position. For example, in *P. tritici* the trichobothria exhibit a 0.5 µm deflection at the rate of 6/sec when the sample is photographed (10 sec exposure) at 5,000X, with 10 kV and a 10 µA emission current (Fig. 2). In all three species, 1) the oscillations are optimum at a particular kV (10 kV in *P. tritici* and *G. jacoti*, 12 kV in *A. longisetosus;* oscillations cease when the kV is lowered or raised by as little as 1 kV from the this value); 3) the oscillations only occur when the beam interacts with a unique 4–5 µm zone along the length of the trichobothrium; 4) no other structures (setae) on the mites show signs of charging or similar movement and 5) the oscillations are consistent and repeatable in the frozen hydrated samples.

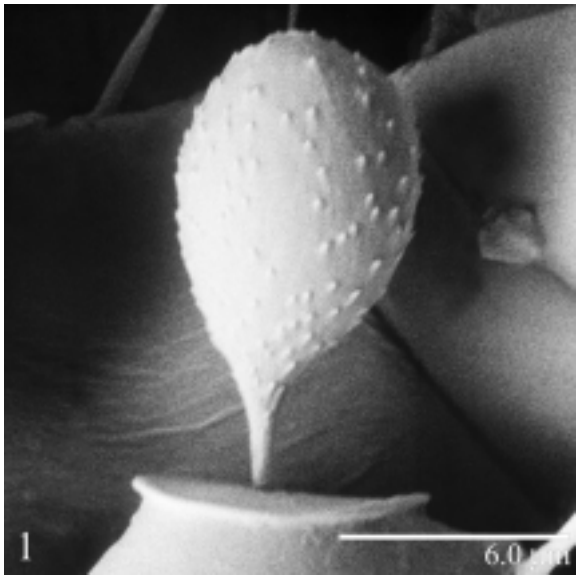

FIG. 1 Bulbous type of trichobothrium characteristic of the *Pyemotes tritici.* The structure is about 10 µm in length, 6 µm at its widest diameter and has a 0.5 µm stalk. Image was recorded at 5 kV (80 sec exposure), which failed to induce oscillations.

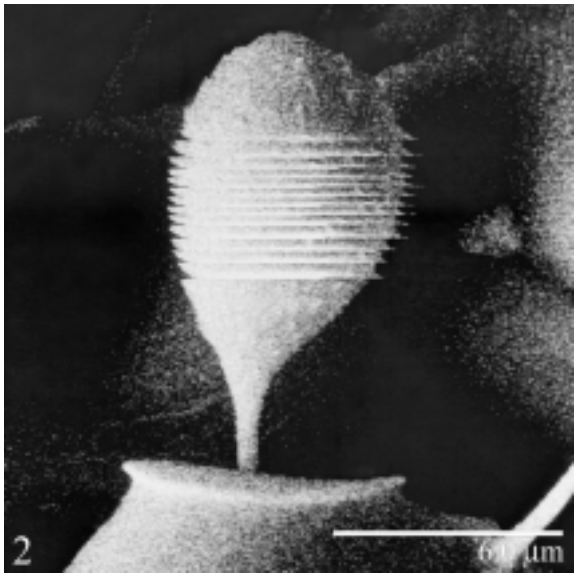

FIG. 2 Same trichobothrium illustrated in Fig. 1. However, this image was recorded at 10 kV (10 sec exposure). The figures shows that 13 oscillations occurred at the rate of 5/sec as the raster scanned a 4 µm segment of the hair. Each oscillation is characterized by a relatively slow movement in one direction followed by a rapid return to the original position.

The function of trichobothria in mites has not been extensively studied. The sole investigation of these setae indicates that they may be mechanical receptors that detect fine vibrations and slight air currents (Pauly 1956). Alternatively, if this observation is not due to some unexplained charging phenomenon in the LTSEM, we suggest that the trichobothria may "function" as a capacitor that would be slightly deflected by an electromagnetic field, possibly generated by its host or prey. If this were the case, differential deflection of the two lateral trichobothria could stimulate basal nerves to alert the mite to the presence and direction of the field. Although magneto-static bacteria have been described, pigeons have a magnetic sensor in their brain and crayfish and sharks have electro-receptors, neither electro- nor magneto-reception has been proposed for mites.

References

1. Evans GW: Principles of acarology. University Press, Cambridge. pp60-94 (1992)
2. Wergin, WP, R Ochoa, EF Erbe, C Craemer AK Raina: Use of low temperature field emission scanning electron microscopy to examine mites. *Scanning* (submitted) (2000).
3. Pauly, F: Zur Biologie einiger Belbiden (Oribatei, Moosmilben) und zur Funktion ihrer pseudostigmatischen Organe. *Zool. Jahrb.* 84,275-328 (1956)